Experiment E865 at BNL
A search for the decay $K^+ \to \pi^+\mu^+e^-$

Inaugural–Dissertation

zur

Erlangung der philosophischen Doktorwürde

vorgelegt der

Philosophischen Fakultät II

der

Universität Zürich

von

Stefan Pislak

aus Neuhausen am Rheinfall SH

begutachtet von Prof. Dr. Peter Truöl

Zürich 1997

Die vorliegende Arbeit wurde von der Philosophischen Fakultät II der Universität Zürich im Sommersemester 1997 auf Antrag von Prof. Dr. Peter Truöl und Prof. Dr. Roland Engfer als Inaugural–Dissertation angenommen.

Zusammenfassung

Diese Arbeit beschreibt ein Experiment zur Suche nach dem Zerfall $K^+ \to \pi^+\mu^+e^-$, $K_{\pi\mu e}$. Die Messungen wurden am Alternating Gradient Synchrotron (AGS) des Brookhaven National Laboratory (BNL) im Frühling 1995 mit der Apparatur der E865-Kollaboration durchgeführt. Der gesuchte Zerfall verletzt die Leptonzahl und ist demnach im Standard Modell nicht erlaubt. Es wurden keine Ereignisse gefunden und eine obere Grenze von 2.1×10^{-10} für das Verzweigungsverhältnis bei einer Vertrauensgrenze von 90% wurde gesetzt.

Abstract

Results of an experimental search for the decay $K^+ \to \pi^+\mu^+e^-$, $K_{\pi\mu e}$, are described. The data were collected at the Alternating Gradient Synchrotron (AGS) of Brookhaven National Laboratory (BNL) in the setup of the E865-collaboration in spring 1995. According to current theory, this decay is forbidden by the conservation law of lepton-flavour. We find no evidence for this decay mode and we establish an upper limit on its branching ratio of 2.1×10^{-10} at the 90% confidence level.

Contents

List of Figures

List of Tables

Chapter 1

Introduction

1.1 Overview

This thesis describes the results of a search for the decay $K^+ \to \pi^+\mu^+e^-$, $K_{\pi\mu e}$. The data presented were collected in experiment E865 at the Alternating Gradient Synchrotron (AGS) of Brookhaven National Laboratory (BNL) during a first running period in spring 1995. According to current theory, this decay is forbidden by the lepton-flavour conservation law. Previous searches [1, 2] found no evidence for this decay mode and set an upper limit on the branching fraction of less than 2.1×10^{-10} at the 90% confidence level.

1.2 Theoretical considerations

In this section, we will make an attempt to motivate the experimental search. We will introduce the concept of lepton number conservation in the standard model, list a few of its shortcomings and conclude with a discussion of possible extensions to the standard model like technicolor, supersymmetry, leptoquarks, etc, which allow lepton number non-conservation.

1.2.1 Lepton number

A first version of the conservation law of the lepton number was introduced on phenomenological grounds, around 1953 [3, 4]. At that time it was believed that there is only one kind of neutrino (ν), and it was assumed that the net number of 'leptons' was conserved, with the convention that e^-, ν, μ^+ were the leptons and e^+, $\overline{\nu}$, μ^- their antiparticles. This conservation law succeeded in forbidding such processes as

$$
\begin{aligned}
\mu^{\pm} + n &\rightarrow e^{\pm} + n \\
\mu^{\pm} &\rightarrow e^{\pm} + e^{+} + e^{-} \\
\mu^{\pm} &\rightarrow e^{\pm} + \gamma
\end{aligned}
$$

But it failed to forbid

$$K^{+} \rightarrow \mu^{+} + e^{+} + \pi^{-}$$

Alternative conservation laws have been proposed since (see [5]), until 1962 Danby *et al.* [6] provided definitive evidence that, as there are two distinct charged leptons (e, μ)*, so there are also two distinct neutral ones (ν_e and ν_μ) and that the electron and its partner neutrino on the one hand, and the muon and its neutrino on the other do not mix with each other.

In the present formulation, there are six known leptons, and they occur in pairs called generations which we write as doublets:

$$\begin{pmatrix} \nu_e \\ e^- \end{pmatrix}, \quad \begin{pmatrix} \nu_\mu \\ \mu^- \end{pmatrix}, \quad \begin{pmatrix} \nu_\tau \\ \tau^- \end{pmatrix}$$

In addition to the leptons there are six corresponding antiparticles:

$$\begin{pmatrix} e^+ \\ \overline{\nu}_e \end{pmatrix}, \quad \begin{pmatrix} \mu^+ \\ \overline{\nu}_\mu \end{pmatrix}, \quad \begin{pmatrix} \tau^+ \\ \overline{\nu}_\tau \end{pmatrix}$$

Each generation of leptons has associated with it a conserved quantum number. The first of these lepton numbers is the electron lepton number defined by

$$L_e = N(e^-) - N(e^+) + N(\nu_e) - N(\overline{\nu}_e) \tag{1.1}$$

where $N(e^-)$ is the number of electrons present, and so on. For single particle states, $L_e = 1$ for e^- and ν_e; $L_e = -1$ for e^+ and $\overline{\nu}_e$; and $L_e = 0$ for all other particles. Similar muon lepton number L_μ and tau lepton number L_τ are defined for the second and third generation, which like the electron lepton number are conserved in all known interactions. Often one introduces an additional 'total' lepton number defined by the sum $L = L_e + L_\mu + L_\tau$. It is obvious that, while the conservation of each L_a $(a = e, \mu, \tau)$ implies L conservation, the converse is not necessarily true.

If the conservation law of lepton number is violated, the conservation of angular momentum requires that the numbers of leptons created or destroyed in a given process be even, provided the number of baryons in the process is conserved, i.e. we can distinguish two main categories:

*The τ lepton was not discovered before 1975

1. The specific lepton numbers L_e, L_μ and L_τ are not separately conserved, while the total lepton number L is conserved.

2. The total lepton number is not conserved, the minimal violations correspond to $|\Delta L| = 2$.

Processes allowed, if the first assumption holds, are:

$$\begin{aligned} \mu^\pm &\rightarrow e^\pm\gamma \\ K_L^0 &\rightarrow \mu^+e^- \\ K^+ &\rightarrow \pi^+\mu^+e^- \end{aligned}$$

They all involve $\Delta L_e = -\Delta L_\mu = \pm 1$ transitions, but provide nevertheless complementary measurements. The first decay differs from the second and third one in its generation number property. Generation number (G) is customary defined as 1 for the fermions of the first generation (e, ν_e, u- and d-quark), 2 for the second generation (μ, ν_μ, c and s) and three for the third generation (τ, ν_τ, t and b). Antiparticles have generation number with opposite sign, gauge bosons have $G = 0$. In the standard model, conservation of G is violated through mixing in the quark sector. If new physics at the scale Λ conserves this quantum number, the second and third decay could be allowed while the first one would be forbidden. Comparing the second and third decay, then, for a given branching ratio, $K_L^0 \rightarrow \mu^+e^-$ is usually favoured because of the greater phase space available and because the K^+ is shorter lived. However, the former proceeds through a pseudovector or pseudoscalar current whereas the latter proceeds through a vector or scalar current. Depending on the nature of the mechanism for lepton number violation, it is quite possible that one of these would be allowed and the other one forbidden.

Passing now to charged processes of the second category, we recognize that such processes must involve also hadrons. Since L is the same for leptons of the same charge, the violation $\Delta L = \pm 2$ corresponds to a change of the charge $\Delta Q_l = \mp 2$ for the leptons, which must be compensated by an opposite change $\Delta Q_h = \pm 2$ for the hadrons. Such processes can be considered as occurring at second order in weak interactions (e.g. neutrinoless double β decay: $n_1 + n_2 \rightarrow n_1 + p_2 + e_2^- + \nu \rightarrow p_1 + e_1^- + p_2 + e_2^-$), i. e. they can only be detected in processes for which the first order transition is forbidden or highly suppressed.

It is clear that the subject of lepton number violation involves many different features. The absence of lepton number violation in one specific decay up to a certain limit does not necessarily infer the absence of lepton number violation in all reactions until this limit. Hence it is important to search for violation in all possible decays channels - $K_{\pi\mu e}$ is one possible avenue. Table 1.1 summarizes the present status of the search for lepton number violation.

Decay	Violates	Upper limit	Reference
$\mu^- \to e^- e^+ e^-$	L_μ L_e	1.0×10^{-12}	[7]
$\mu^- \to e^- \gamma$	L_μ L_e	4.9×10^{-11}	[8]
$\tau^- \to e^- \gamma$	L_τ L_e	1.1×10^{-4}	[9]
$\tau^- \to \mu^- \gamma$	L_τ L_μ	4.2×10^{-6}	[10]
$\tau^- \to e^- e^+ e^-$	L_τ L_e	3.3×10^{-6}	[11]
$\tau^- \to \mu^- \mu^+ \mu^-$	L_τ L_μ	1.9×10^{-6}	[12]
$\tau^- \to e^- \mu^+ \mu^-$	L_τ L_e	3.6×10^{-6}	[11]
$\tau^- \to e^+ \mu^- \mu^-$	L_τ L_e L_μ	1.1×10^{-4}	[11]
$\tau^- \to \mu^- e^+ e^-$	L_τ L_μ	3.4×10^{-6}	[11]
$\tau^- \to \mu^+ e^- e^-$	L_τ L_e L_μ	3.4×10^{-6}	[11]
$\tau^- \to \mu^- \pi^+ \pi^-$	L_τ L_μ	7.4×10^{-4}	[11]
$\tau^- \to \mu^+ \pi^- \pi^-$	L L_τ L_μ	3.7×10^{-4}	[11]
$K^+ \to \pi^+ \mu^+ e^-$	L_e L_μ	2.1×10^{-10}	[2]
$K^+ \to \pi^+ \mu^- e^+$	L_e L_μ	7×10^{-9}	[1]
$K^+ \to \pi^- \mu^+ e^+$	L L_e L_μ	7×10^{-9}	[1]
$K^+ \to \pi^- e^+ e^+$	L L_e	1.0×10^{-8}	[1]
$K^0 \to \mu e$	L_e L_μ	3.3×10^{-11}	[13]
$D^+ \to \pi^+ \mu^+ e^-$	L_e L_μ	3.3×10^{-3}	[14]
$D^0 \to \mu e$	L_e L_μ	1.9×10^{-5}	[15]
$B^+ \to \pi^+ \mu^+ e^-$	L_e L_μ	6.4×10^{-3}	[14]
$B^0 \to \mu e$	L_e L_μ	5.9×10^{-6}	[16]
$\mu^- Ti \to e^- Ti$	L_e L_μ	4.3×10^{-12}	[17]

Table 1.1: Summary of decays violating lepton number. The specific charge mode in which the limit has been established is not quoted.

1.2.2 Standard model

The standard model of elementary particle physics almost perfectly explains the results of many different experiments. Especially, the agreement with the recent precision experiments at the LEP collider is remarkable. The unified description of electromagnetic and weak interactions is now established. They are described as the gauge interaction of the symmetry $SU(2)_L \otimes U(1)_Y$ (electroweak symmetry) which contains four massless gauge bosons. This gauge symmetry is spontaneously broken to the electromagnetic gauge symmetry $U(1)_{em}$, and three gauge bosons (weak gauge bosons) get their mass by the Higgs mechanism. The high mass of these gauge bosons explains why the weak interaction is of short range. The electroweak symmetry requires massless quarks and leptons. Quarks and leptons cannot be massive till the electroweak symmetry breaking is achieved. Therefore the mechanism of the mass generation must tightly be related to the mechanism of electroweak symmetry breaking.

In the standard model, electroweak symmetry is spontaneously broken by the vacuum expectation value of the elementary Higgs field. The magnitude of the vacuum expectation value decides the masses of the weak gauge bosons. The masses of fermions (quarks and leptons) are generated through the Yukawa interactions between the fermion fields and Higgs field. The mixing among the quarks with the same electric charge is also generated. This mixing is the origin of the Cabibbo-Kobayashi-Maskawa (CKM) mixing angles and CP violation in the weak interaction.

Neglecting the mixing in the quark sector, the standard model could be constructed and would be mathematically self-consistent with only four fermion fields: the up and down quarks, the electron and its neutrino. But more particles have to be introduced, as prescribed by experiment. These new particles are clones of the four basic ones except for their masses. They are included in the Lagrangian of the standard model by just arbitrarily adding terms involving the new fermions, these are exactly identical to the Lagrangian of the first generation except for different Yukawa couplings to the Higgs boson in order to generate different mass after symmetry breaking. This is how the conservation of lepton number is ensured in the standard model.

1.2.3 Motivation for physics beyond the standard model

Why does one expect new physics beyond the standard model? Although very successful, the model is clearly incomplete. It rests on many assumptions and leaves many fundamental questions unanswered. For illustration, we will list a few of the major puzzles of the standard model.

The standard model has three different gauge groups postulated from phenomenological considerations. They are associated with three different gauge coupling constants, which are arbitrary. In a more satisfactory theory, one should have a way of not only understanding the three gauge groups but also the origin of the three gauge couplings. The most popular approach to address these problems is grand unification, proposing the existence of a simple symmetry group which breaks spontaneously into the standard model group at a large energy scale. However, the simplest and most predictive grand unification theory, minimal $SU(5)$, predicts proton decay at a too rapid rate to agree with experimental limits.

Furthermore, the standard model assumes the Higgs mechanism and an associated physical Higgs particle. Well, what's wrong with the Higgs? Like all massive particles, the Higgs bosons 'bare' mass is not its effective mass due to a cloud of virtual particles which is always present. This cloud causes higher order corrections to the Higgs mass.

This correction gives rise to the hierarchy problem. The parameters of the Higgs potential must be fine tuned if the standard model is looked upon as an effective theory. Suppose that the standard model is valid up to a certain high energy scale Λ (GUT scale or Planck scale, for example). Then the Higgs potential

$$V(\Phi) = -m^2\Phi^\dagger\Phi + \frac{\lambda}{4}(\Phi^\dagger\Phi)^2 \tag{1.2}$$

receives a first order correction as

$$V(\Phi)_{\text{one loop}} = -(m^2 - \lambda\frac{\Lambda^2}{16\pi^2})\Phi^\dagger\Phi + \frac{\lambda}{4}(\Phi^\dagger\Phi)^2 \tag{1.3}$$

leading to a vacuum expectation value for the Higgs field Φ of

$$\langle\Phi\rangle = \frac{\upsilon}{\sqrt{2}}\begin{pmatrix} 0 \\ 1 \end{pmatrix} = \sqrt{\frac{2(m^2 - \lambda\Lambda^2/16\pi)}{\lambda}}\begin{pmatrix} 0 \\ 1 \end{pmatrix} \tag{1.4}$$

This value must be of the order of the electroweak scale $\upsilon \simeq 250$ GeV to give a realistic weak boson mass. Since $\Lambda_{GUT} \simeq 10^{15}$ GeV or $\Lambda_{Planck} \simeq 10^{19}$ GeV, we must take for the mass m^2 a large value, and fine-tune to cancel the large value $\lambda\Lambda^2/16\pi$ with a tremendous precision, a very unnatural situation. This work must be iterated order by order in loop calculation. This problem is addressed by e.g. technicolor and supersymmetry.

Another puzzle is the gravity problem, Einstein's gravity is totally outside of the framework of gauge theories. In fact, adding gravity to gauge theories destroys the attractive property of renormalization.

And finally, the conservation of separate lepton number, L_e, L_μ and L_τ, is not understood at a fundamental level. An additive conservation law, such as charge conservation, baryon number conservation and each type of separate lepton number conservation, implies the existence of global $U(1)$ gauge invariance. In the case of the charge conservation, the global invariance is understood as the result of the stronger local $U(1)$ gauge invariance, from which the form of the electromagnetic interaction is derived. Such an unbroken gauge symmetry requires the existence of a massless boson, namely the photon. No known massless boson is associated with baryon number or lepton number conservation, indicating that the global invariance associated with these additive conservation rules is not a consequence of a gauge principle. Therefore baryon number and separate lepton number conservation appear not to be fundamental and may be expected to be violated. In view of these considerations, it seems likely that lepton flavour transitions are not strictly forbidden, but are highly suppressed in some dynamical process which lies outside the standard model.

1.2.4 Attempts to go beyond the Standard Model

As discussed in the sections 1.2.1 and 1.2.2 , L and also L_e, L_μ and L_τ are conserved in the standard model. It is therefore clear that any detectable breaking of the conservation law must be connected with a suitable extension of the standard model. In order to have lepton number violation, one must either enlarge the particle content on the matter side, or the gauge group with the introduction of new gauge vector bosons, or both. In this section we shall briefly examine possible extensions to the standard model which allow lepton number nonconservation.

Massive Neutrinos

A minimal extension of the standard model is the inclusion of massive neutrinos. By adding right-handed singlet ν_R fields, one can get Dirac masses. A natural concomitant of massive non-degenerate neutrinos is lepton number violation, similar to the mixing in the quark sector. Thus the weak eigenstates ν_e, ν_μ and ν_τ would be linear combinations of the neutrino mass eigenstates ν_1, ν_2 and ν_3 with definite mass eigenvalues m_1, m_2 and m_3. This mixing would give rise to the various lepton number violating decays, such as $\mu \to e\gamma$, $K_L \to \mu^\pm e^\mp$ and also $K^+ \to \pi^+\mu^+e^-$. Both kaon decays proceed then via box diagrams as shown in Fig. 1.1. However, the contributions from these diagrams are too

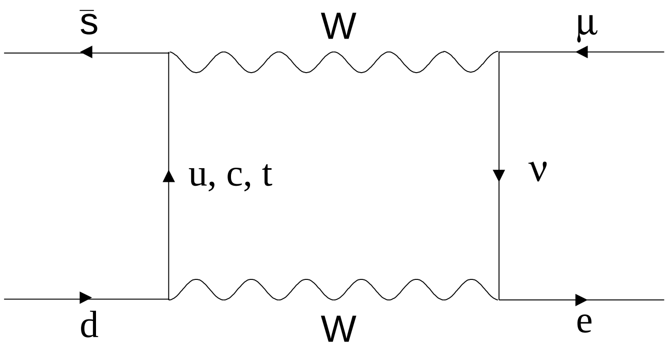

Figure 1.1: Box diagram giving rise to $K_{\pi\mu e}$ in models with massive neutrinos.

small to be relevant. If the exchanged neutrino is an ordinary light neutrino (ν_e, ν_μ, ν_τ) then the amplitude is suppressed by m_ν^2 leading to branching ratios well below 10^{-25} [18].

An appealing idea is to extend the electroweak theory by introducing right-handed weak interactions based on $SU(2)_L \otimes SU(2)_R \otimes U(1)$, leading to a right-left symmetric electroweak model. Lepton number violation need not occur in such models, but if massive right-handed neutrinos also appear, then the branching ratio for $K_{\pi\mu e}$ could be as large as 10^{-13} [19] to 10^{-15} [18].

Supersymmetry

The main motivation for the introduction of supersymmetric models (see [20] for a review) is, as in technicolor, the absence of the gauge hierarchy problem. This occurs via cancelations in certain Feynman diagrams which are insured by requiring that each known particle has a supersymmetric partner [21]. Furthermore, supersymmetry appears very naturally in superstring theory. String theory, in turn, is clearly our currently best hope for a 'theory of everything', which would in particular include a quantum theory of gravity.

Supersymmetry essentially doubles the number of elementary particles. To each ordinary particle there corresponds a supersymmetric partner (sparticle) and they are combined in superfields. An ordinary particle and its superpartner differ in spin by half a unit but, besides that carry identical quantum numbers. Consequently, the partner of a fermion has to be a boson and vice versa and - the ordinary particles and their partners need to be of equal mass. It is clear, then, that supersymmetry must be a broken symmetry, for example, there is no sparticle with the mass and quantum number of the electron. In fact, there are no candidate supersymmetric partners for any of the ordinary particles in the observed spectrum.

The mechanism of supersymmetry breaking is not well understood. It is typically assumed that the breaking spontaneously occurs at a high scale, e.g. the Planck scale, and perhaps results from some complete theory encompassing gravity. Technically, the breaking is implemented by including explicit 'soft' mass terms in the Lagrangian [22]. These interactions are termed soft because they do not re-introduce the quadratic divergences which motivated the introduction of supersymmetry in the first place.

Since supersymmetric theories contain a plethora of new particles, it is not surprising that they feature new mechanisms for lepton number violation. Generally, one can imagine that lepton number violation can arise (i) in processes where the neutrinos get masses [23] or (ii) through various trilinear couplings [24]. But constraints originating from the stability of the proton, from neutrino mass limits and from the suppression of lepton flavour changing decays like $\mu \to 3e$ and $\mu \to e\gamma$ rule out most of these mechanisms. Hence different conservation laws have been examined which do not conflict with the experiment but allow lepton number violation. We will not go here into further detail, for additional information the review by Costa and Zwirner [25] may be consulted. Several authors [26, 27, 28, 29] have calculated the box diagram shown in Fig. 1.2, the only Feynman graph giving contributions to $K_{\pi\mu e}$. In general, information about the mass difference between the supersymmetric partners of the quarks and the leptons could be deduced, but it was found [29] that the experimental sensitivity has to be as low as 10^{-14} to allow any consistent statements.

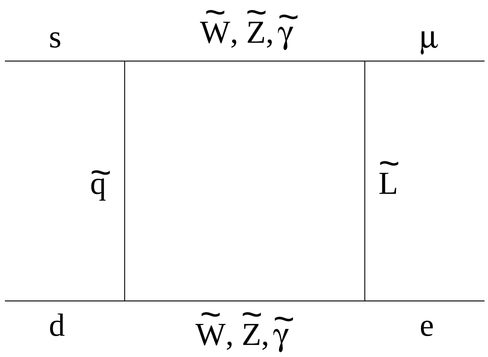

Figure 1.2: SUSY contribution to $K_{\pi\mu e}$. $\tilde{W}$, $\tilde{Z}$ and $\tilde{\gamma}$ are the supersymmetric partners of the electroweak W, Z and γ bosons. $\tilde{q}$ is a supersymmetric quark and $\tilde{L}$ a supersymmetric lepton.

Technicolor

Technicolor models (see [30, 31] for reviews) are introduced to provide a symmetry breaking mechanism to replace the standard one based on Higgs bosons. In technicolor (TC) models there is no Higgs, it is substituted by a set of technifermions, transforming according to a new gauge group. Imagine that there is a new asymptotically free gauge interaction which becomes strong in the vicinity of a few hundred GeV and gives rise to a technifermion condensate. This an exact copy of QCD: when the color interaction becomes strong enough, condensates of a pair of quarks appear. This technifermion condensate breaks the chiral technisymmetry resulting in the generation of massless Goldstone bosons. For pure TC this would be the end of the story, but in the presence of the gauge sector of the electroweak Lagrangian, the Higgs mechanism occurs. Three Goldstone bosons are eaten up while the W and Z bosons acquire masses. The photon remains massless. However, in the minimal technicolor model just described, there is no obvious way to give the leptons and quarks masses, since the Yukawa couplings are absent. To solve this problem in the spirit of technicolor, i.e. without the introduction of elementary scalars, it is necessary to go to extended technicolor (ETC) models. Within this theory, the ordinary fermions and the technifermions are embedded in a larger gauge group. Figure 1.3 shows a simple example. ETC bosons will mediate transitions between ordinary fermions and technifermions. By hypothesis, the ETC symmetry will break spontaneously and the ordinary fermions will acquire mass. Since the mass m_f of the ordinary fermions is estimated to be [32]

$$m_f \simeq \frac{(300\ \text{GeV})^3}{M_{ETC}^2} \tag{1.5}$$

we calculate the mass M_{ETC} of the ETC bosons to be in the range of tens of TeV.

$$\begin{pmatrix} u \\ d \\ e \\ \nu_e \\ A_1 \\ A_2 \\ \vdots \end{pmatrix} \quad \begin{pmatrix} c \\ s \\ \mu \\ \nu_\mu \\ B_1 \\ B_2 \\ \vdots \end{pmatrix} \quad \begin{pmatrix} t \\ b \\ \tau \\ \nu_\tau \\ C_1 \\ C_2 \\ \vdots \end{pmatrix} \begin{array}{l} \left.\begin{array}{l} \\ \\ \end{array}\right\} \text{Quarks} \\ \left.\begin{array}{l} \\ \\ \end{array}\right\} \text{Leptons} \\ \left.\begin{array}{l} \\ \\ \\ \end{array}\right\} \text{Technifermions} \end{array}$$

Figure 1.3: Representation of ETC group.

The phenomenology of technicolor models is rich. In most versions some of the ETC bosons will connect ordinary fermions as well, leading to flavour changing neutral interactions, allowing processes like $K_{\pi\mu e}$ or $K_L^0 \to \mu e$ and also giving contributions to the $K^0 - \overline{K^0}$ mass difference.

The predictions for the $K_{\pi\mu e}$ decay rate from ETC theories are fairly independent of the details of the model chosen. The decay is assumed to occur via ETC boson exchange. The s-quark in the kaon turns into a d-quark and emits a ETC boson which creates a μe pair at the other vertex. The rate can be estimated because of the similarity with the decay $K^+ \to \pi^0 \mu^+ \nu$, $K_{\mu 3}$. This weak decay proceeds through W exchange and the Feynman diagrams of the two processes are virtually identical (Fig. 1.4). Since the phase space factors are comparable, the ratio of rates is then given by [32, 33]:

$$\frac{\Gamma(K_{\pi\mu e})}{\Gamma(K_{\mu 3})} = 16 \frac{1}{\sin^2\theta_c} \left(\frac{M_W}{M_{ETC}}\right)^4 \left(\frac{g_{ETC}}{g_W}\right)^4 \tag{1.6}$$

where M_W the mass of the weak boson, g_W and g_{ETC} the gauge coupling constants and θ_c the Cabibbo angle. The factor of 16 comes from the assumption that the interaction leading to $K_{\pi\mu e}$ is purely vectorial. With a branching ratio of 2.1×10^{-10} for $K_{\pi\mu e}$ equation 1.6 yields a lower limit for the mass of the ETC bosons of:

$$M_{ETC} > 40 \text{ TeV} \tag{1.7}$$

where we made the simplifying assumption that $g_{ETC} \simeq g_W$. We immediately recognize, that this mass limit is comparable with the predicted mass of the ETC boson. To keep technicolor alive, 'walking' technicolor models [34] have been constructed. This mechanism may provide a means of escape from the problems with $K_{\pi\mu e}$ and comparable decays. However, current limits presents a serious challenge to ETC models.

Leptoquarks

Recently the H1 and ZEUS groups at HERA reported that they see more events at very high momentum transfer than expected from the standard model [35, 36]. A scenario that

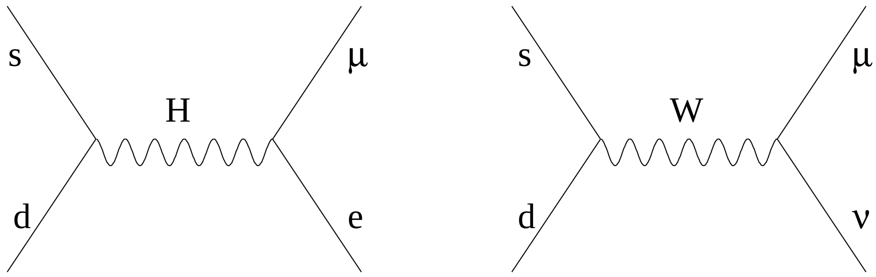

Figure 1.4: A comparison between the Feynman diagrams for the processes $K_{\pi\mu e}$ (left) and $K_{\mu 3}$ (right). H is a horizontal extended technicolor boson, while W is the weak boson.

could explain the extra events is a resonant production of bound positron-quark states, such as leptoquarks.

A leptoquark is a scalar or vector particle that couples to a quark and a lepton. They first appeared in the $SU(4)$ model from Pati and Salam [37] in which leptons are treated on the same basis as quarks. Leptons then carry a fourth color, which is lepton number. $SU(4)$ is spontaneously broken, so that the gluons remain massless and the leptoquarks gauge bosons become heavy. An alternative kind of leptoquarks appear in $SU(5)$ unified theories [38]. This is a general feature of grand unified theories (GUT), the quarks and leptons share multiplets, so there are necessarily leptoquark gauge bosons. Leptoquarks can also appear in extended technicolor models, mediating interactions between the members of the generations shown in Fig. 1.3. Leptoquarks arise also in composite models (see [39] for a review). In these scenarios, the leptons and quarks, and sometimes the gauge bosons are assumed to be bound states of more fundamental particles. Leptoquarks can then exchange appropriate constituents and turn quarks into leptons and vice versa.

In the $SU(5)$ model, leptoquarks violate baryon and lepton number conservation. From the experimental limit on the lifetime of the proton, it can be concluded that these leptoquarks must be very heavy, with masses larger than 10^{15} GeV [38]. Also Pati-Salam leptoquarks are probably heavier than 10^5 GeV [40]. The masses of technicolor leptoquarks, however, are predicted to be in the order of a few 100 GeV [41] and also composite models predict leptoquarks with masses of the order of 100 GeV [42, 43].

Figure 1.5 shows the simple graph mediating $K_{\pi\mu e}$ via a leptoquark. Since the branching ratio

$$BR(K_{\pi\mu e}) \sim \frac{\lambda_1^2 \lambda_2^2}{M_{LQ}^4} \tag{1.8}$$

where λ_1 and λ_2 the coupling constants at the two vertices and M_{LQ} the mass of the leptoquark, authors usually state a limit on this ratio. Following Davidson [44] the mass of the leptoquark needs to be in the order of 100 TeV assuming $\lambda \simeq 1$ and $BR(K_{\pi\mu e}) < 2.1 \times 10^{-10}$, while, on the other side, assuming $M_{LQ} \simeq 100$ GeV, λ can not be larger than 10^{-6}.

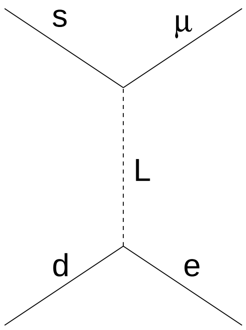

Figure 1.5: Feynman diagram for the decay $K_{\pi\mu e}$ mediated by a leptoquark L.

If the anomaly at high momentum transfer and high positron-quark masses observed by the HERA experiments is indeed a signal for a leptoquark, our experiment as a few other low energy experiments rule out many of the allowed choices for the quantum numbers [45]. In this respect the small scale precision experiments at low energy machines, which require a lot of patience, are complimentary to high energy measurements.

Summarizing, we recognize that lepton number violation can be mediated either through box diagrams (Fig. 1.1, 1.2), or through horizontal bosons (Fig. 1.4), or through leptoquarks (Fig. 1.5). While our sensitivity is not large enough to challenge models requiring box diagrams, we can impose serious constraints on models involving horizontal bosons and leptoquarks.

Chapter 2

AGS

The accelerator complex at the Brookhaven National Laboratory consists of a variety of machines including the Alternating Gradient Synchrotron (AGS), the Relativistic Heavy Ion Collider (RHIC), the Tandem Van de Graaff, the Linac and the Booster.

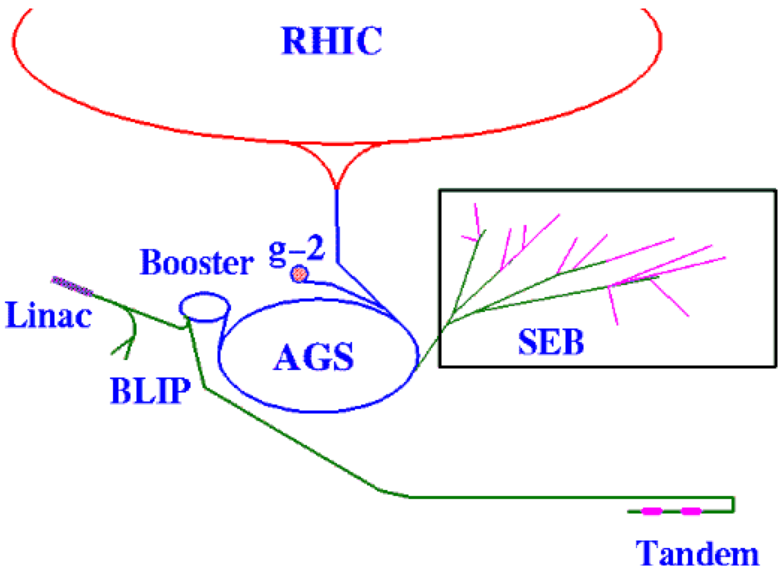

Figure 2.1: Layout of the accelerator complex and of the secondary beam lines (SEB), where the individual kaon decay experiments are located.

The AGS is a strong focusing synchrotron which ran first in 1960. The protons, used for producing kaons, are accelerated to 200 MeV by the Linac and injected into the Booster, which accelerates them to 1.5 GeV and injects three times four bunches into the AGS at 7.5 Hz, where they reach their final energy of 25.2 GeV. Before the slow extraction, the beam is debunched, i.e. particles are smeared over the circumference of the ring to insure an uniform beam intensity during the 1.6 second long spill. The total cycle time is 3.2 seconds. The main parameters for the run in 1995 are collected in Table 2.1.

Momentum	25.2 GeV
Max. intensity	60×10^{12} protons per pulse
Flattop length	1600 ms
Flattop field	1.052 T
Rep. rate	3200 ms
Mean radius	128.5 m
Tune	(Qh,Qv) = (8.67,8.76)
Phase transition	8.5 GeV

Table 2.1: Setup parameters of the AGS for proton operation [46].

Beside protons, the AGS accelerates also polarized protons and ions as heavy as gold. After RHIC is commissioned in 1999, the AGS will serve in addition as pre-accelerator for this new machine which will collide heavy ions at energies of 100 GeV in each beam.

Chapter 3

Experiment E865

3.1 Design philosophy

When searching for a rare decay mode, there are two conditions that need to be satisfied: First, a large number of parent particles must be available and second, the detector must be able to suppress all the background to a level such that a rare decay signal would be clearly recognizable. With the proton beam provided by the AGS, one can obtain a beam in the order of 6×10^7 kaons per spill or 7×10^{10} kaons per hour. This flux is more than adequate to conduct a serious search for a rare decay mode.

Crucial to the design of the detector is an understanding of the background to be expected in the search for $K^+ \to \pi^+\mu^+e^-$ ($K_{\pi\mu e}$), i.e. the background dictates the design of the detector. Hence, we will first look at the most dangerous K^+ decays or decay chains resulting in possible background before we describe the experiment. Possible sources of background contain either the wrong final state particles or have additional (neutral) particles in the reconstruction. Identifying these backgrounds is then accomplished by particle identification and kinematical rejection:

- The dominant decay allowed by the standard model which gives the correct final state particles is $K^+ \to \pi^+\pi^+\pi^-$, K_τ, the so called tau decay of the kaon, followed by $\pi^+ \to \mu^+\nu$ and $\pi^- \to e^-\overline{\nu}$. It has a combined branching ratio of 6.8×10^{-6}. Because the apparatus is necessarily short in order to maximize the geometrical acceptance, the decay length of the pion at AGS energies is large compared to the length of the apparatus. With a pion energy of typically 2 GeV and a detector length of 10 m, the background level is reduced by a factor of 100 to a few parts in 10^{-8} before kinematical reconstruction. Monte Carlo studies show that this background can be pushed below 0.25×10^{-12} with kinematical reconstruction.

- Another potential background from tau decay K_τ arises if (1) either one of the positively charged pions is misidentified as a muon and the negatively charged pion decays into an electron and a neutrino or if (2) the negatively charged pion is misidentified as electron and a positively charged pion decays into a muon and a neutrino, or (3) the positively and the negatively charged pion are misidentified as a muon and as an electron, respectively. The branching ratios for the tau decay is 5.6%, the pion decay into a muon and a neutrino 100%, and the branching ratio of a pion into an electron and a neutrino is 1.2×10^{-4}. The remaining orders of magnitude have to come from kinematical reconstruction and, most importantly, from a good particle identification. This background requires a separation between negatively charged pions and electrons in the order of 10^{-5} and a separation between pions and muons of 10%. For the latter a stack of muon chambers and for the former two Čerenkov counters and a calorimeter are used in E865. To achieve such a low π^-/e^- misidentification probability it is necessary to select a gas for the Čerenkov counters with a high threshold, minimal scintillation light and minimal effects from delta rays to exclude all possible sources where other particles than electrons originating from K^+ decays can give light in the Čerenkov counters.

- The decay $K^+ \to \pi^+\pi^0$ with $\pi^0 \to e^+e^-\gamma$, the so called Dalitz decay, K_{DAL}, with a misidentification of the e^+ as a π^+ and either misidentification of the π^+ as a μ^+ or the decay $\pi^+ \to \mu^+\nu$ also leads to a fake $K_{\pi\mu e}$ decay. For this decay chain, the combined branching ratio is 2.5×10^{-3}. To suppress such decays with an e^+ in the final state, it is necessary to have substantial light to limit the effect of inefficiencies in the Čerenkov counters, e.g. cracks between the mirrors or electronic failures. This requires a gas with a lower threshold and consistently with a greater yield of Čerenkov photons than it is found optimal for π^-/e^- separation, resulting in a large rejection of e^+ against π^+. Therefore positively and negatively charged particles have to be separated and the detector is split into two halves. Kinematically this decay chain is especially dangerous, since an event can be measured with the correct invariant mass despite the missing neutral(s) due to the fact that incorrectly labeling the particles in the reconstruction adds mass to the system. This can be reduced by making requirements on the phase space parameters of the reconstructed kaon (momentum, position, angles).

Table 3.1 summarizes the background channels mentioned above and the required misidentifications are given.

Decay	Misidentification
K_τ with $\pi^+ \to \mu^+\nu$, $\pi^- \to e^-\overline{\nu}$	None
K_τ with $\pi^+ \to \mu^+\nu$	π^- as e^-
K_τ with $\pi^- \to e^-\overline{\nu}$	π^+ as μ^+
K_τ	π^- as e^- and π^+ as μ^+
K_{DAL}	e^+ as π^+ and π^+ as μ^+
K_{DAL}	e^+ as μ^+
K_{DAL} with $\pi^+ \to \mu^+\nu$	e^+ as π^+
$K^+ \to \pi^0\mu^+\nu$, $\pi^0 \to e^+e^-\gamma$	e^+ as π^+

Table 3.1: Possible background to $K_{\pi\mu e}$.

3.2 Overview of the detector

The considerations of the previous section lead to the design of a detector as shown in Figure 3.1. Kaon decays in a 5 m long evacuated decay volume may be accepted by the detection system. The decay products are deflected out of the beam region and separated by charge, with positively charged particles being deflected to the right side and negatively charged particles being swept to the left by a first dipole magnet called D5. A set of four multiwire proportional chambers (MWPC) together with a second dipole magnet (D6), serve as spectrometer to measure the momentum of the decay products. The magnetic field in D6 is opposite the field in D5 in order to keep the trajectories in a volume as small as possible. The first two MWPC's, P1 and P2, are located upstream of D6, the other two MWPC's, P3 and P4, are placed downstream of D6. Downstream of P2, halfway inside D6 and between P3 and P4 two threshold Čerenkov counters (C1, C2) provide particle identification for electrons and positrons. An electromagnetic shower calorimeter, which further aids to separate electrons and positrons from pions and muons, is placed downstream of P4 followed by a stack of 12 muon chambers which are designed to distinguish between muons and other particles. The apparatus is completed by three scintillator trigger hodoscopes: the A-counter upstream of the calorimeter, the B-counter after two thirds of the muon stack, and the C-counter at the end.

E865 uses a right-handed coordinate system with the origin in the center of the upstream entrance of D5. The Z-axis points into the beam direction, the Y-axis points upwards, the X-axis points towards the 'left' side.

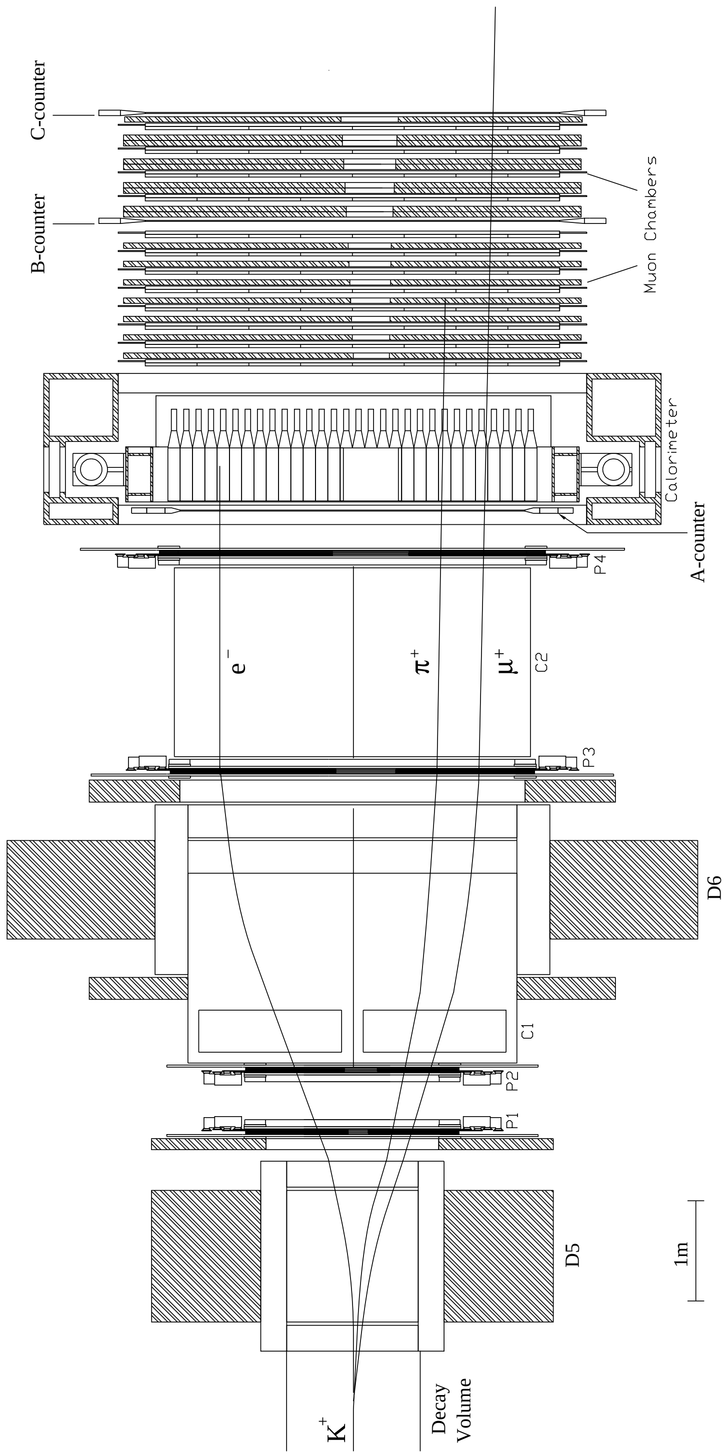

Figure 3.1: Plan view of the E865 detector with a simulated $K_{\pi\mu e}$ decay.
P$_i$: Multiwire proportional chambers, C$_i$: Čerenkov counters, D$_i$: Dipole magnets.

3.3 Secondary beam line and target

The 25.2 GeV proton beam extracted from the AGS strikes a 15 cm long, water cooled copper target producing a spray of secondary particles consisting of mainly pions, protons and kaons. The purpose of the secondary beam line is to select positively charged particles of a specified momentum and emittance. The choice of the momentum is dictated by the requirement of keeping the momentum of the beam particles below the threshold for producing Čerenkov light (6.3 GeV in Hydrogen gas at atmospheric pressure) and, on the other side, to get a high relativistic boost to raise the acceptance of the apparatus and to increase the lifetime of the kaon in the laboratory to give more time to collimate. Considering these constraints a beam momentum of 6 GeV/c is selected.

Figure 3.2 sketches the secondary beam line. The dipole magnets D1 and D2 deflect the secondary particles away from the proton beam. Horizontal and vertical collimators in D1 define the production angle as 3.5° and the angular acceptance to -30 mr/+20 mr horizontally and $\pm$10.75 mr vertically. The quadrupole magnets Q1 and Q2 together form a strong focussing doublet to produce a horizontal and vertical focus with a momentum dispersed image in the center of Q3. Q1 has vertical and horizontal collimators with an angular acceptance slightly larger than D1. Movable collimators upstream of Q3 (for low momentum) and downstream of Q3 (for high momentum) determine the momentum acceptance of the beam as $\Delta p/p \sim 5\%$ FWHM. Q4, Q5 and Q6 produce a second intermediate focus in Q7. D3 and D4 serve to make the beam in this focus achromatic. Horizontal and vertical collimators in Q7 do not limit the beam, but they shield the apparatus from beam halo. Additional collimators are installed in Q5 and D4 in order to help to reduce the number of muons originating from pion decays. Finally, Q8 and Q9 focus the beam at the first MWPC P1. The 5 m long decay volume is located after Q9. About 5% of the kaons produced in the target and accepted by the beam line decay within this volume. The distance between the target and the beginning of this decay volume is 27.6 m, corresponding to about 60% of the decay length of 6 GeV/c kaons.

A secondary emission chamber (SEC) and a stack of three scintillation counter telescopes that view the target at an angle of 90° are used to monitor the intensity of the primary proton beam. The SEC consists of five 25 μm aluminum foils plated with 6 μm silver foils separated by several millimeter in argon gas at atmospheric pressure. A bias voltage of 40-50 V is applied between the foils to collect the electrons liberated by the beam. The collected charge is proportional to the number of protons passing through the foils. For the calibration aluminum irradiation techniques are used. The beam profile is monitored by two segmented wire ionization chambers (SWIC) with one millimeter wire spacing. One is located upstream of the target to monitor the primary proton beam, the other one is installed just downstream of Q7 to control the secondary beam. A phospho-

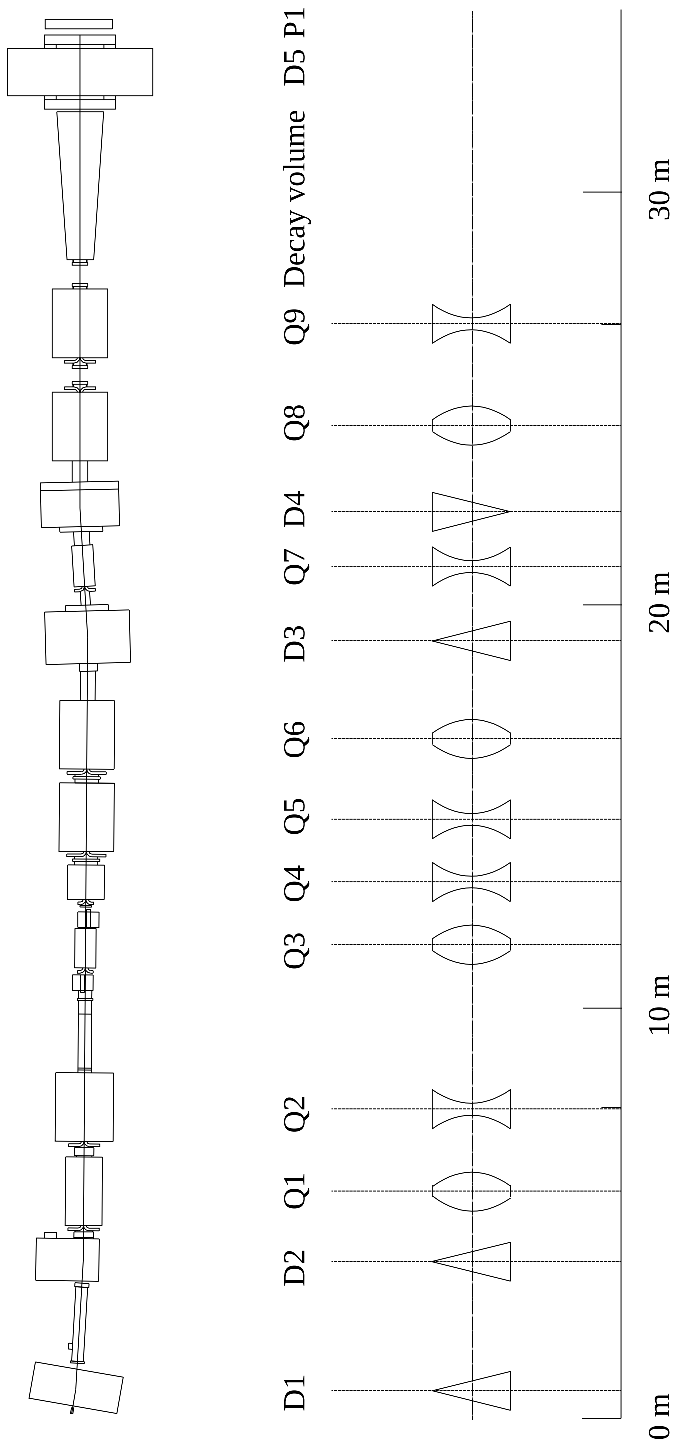

Figure 3.2: Plan view of the E865 secondary beam line and beam optics. Q_i: Quadrupole lenses, D_i: Dipole magnets (prisms).

rescent screen is mounted about 10 cm upstream of the target and is viewed by a video camera to allow more coarse adjustments of the beam position. With 10^{13} protons on target the beam line yields 7×10^7 K^+ per 1.6 second AGS spill accompanied by 1.7×10^9 protons and pions [47]. It is not possible to separate the kaons from the protons and the pions without losing a significant part of the phase space of the beam.

3.4 Spectrometer magnets

Two spectrometer magnets are found in the experiment E865. The first one, D5, separates positively from the negatively charged particles. It is 48 inches[†] wide and 48 inches deep along the beam axis (48D48). The vertical gap is 24 inches. The line integral of its vertical field, measured in units of transverse momentum deflection (p_t-kick) is 240 MeV/c. D6, the second spectrometer magnet is 120 inches wide, 36 inches long (120D36), and has a gap of 50 inches, and yields a p_t-kick of 255 MeV. The three components of the magnetic field including the fringe field were mapped on a grid in 5 cm steps using a Hall probe. The map starts about 1 m upstream of the entrance of D5 and ends 10 cm downstream of P4. Figure 3.3 shows the B_Y and B_Z components of the magnetic field.

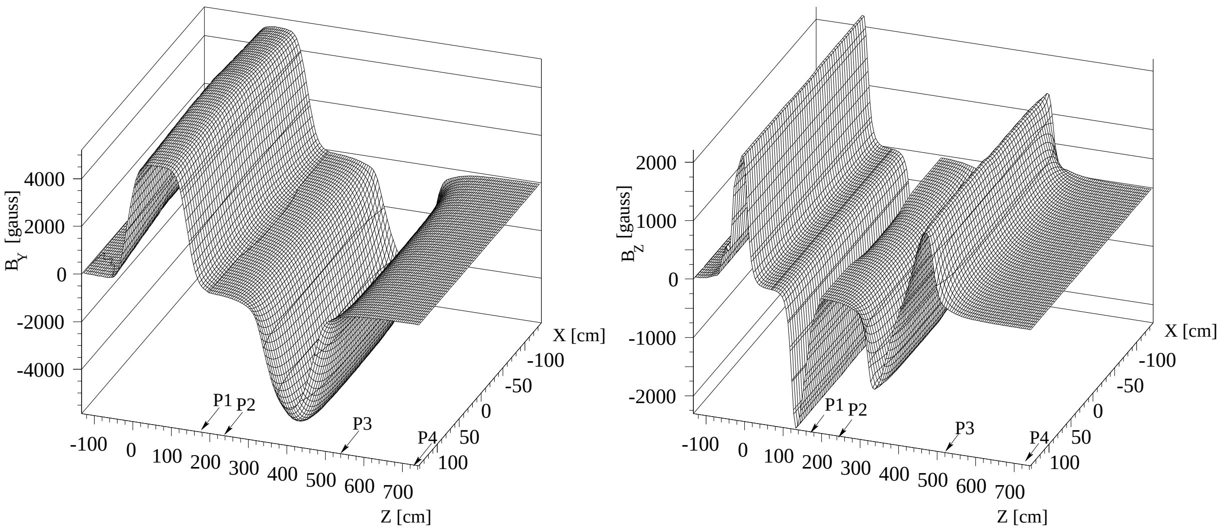

Figure 3.3: Y-component of the magnetic field at fixed Y = 0 cm and Z-component of the magnetic field at fixed Y = 20 cm as a function of the X- and Z-coordinate. The positions of the four MWPC's are also indicated.

[†]One inch is equal 2.54 cm

3.5 Multiwire proportional chambers

3.5.1 Design considerations

The goal of the chamber design is to build a system capable of measuring the positions of tracks with great accuracy as they are bent through the magnetic fields of the spectrometer magnets in order to determine the momenta of the decay particles. This has to be done in a high rate environment. Roughly 50 MHz of secondary particles, i.e. particles originating from decaying beam particles and from beam particles scattered at the apertures of the beam line magnets pass through the chambers. Additionally, the particle flux in the beam line itself (>1 GHz) has to cross the chambers in their central area. This explains the choice of multiwire proportional chambers (MWPC) rather than drift chambers. MWPC can stand a higher beam intensity and have a better pattern recognition efficiency than drift chambers.

Theoretically, MWPC's with two sense wire planes, would suffice to determine the position of a track. To reduce inefficiencies, to control the combinatorics due to random hits, to improve the position resolution, and, especially, to determine the positions unambiguously, more wire planes are desirable. On the other hand, additional wire planes add material and the resolution gets smeared due to multiple scattering. Experience with a previous experiment [48] showed that four planes are necessary to have enough redundancy. The accuracy of the position measurement obviously depends also on the spacing between the anode wires. But since the potential difference between the anode and the cathode has to be increased if the wire spacing is decreased to get a comparable gas gain, spacings of less than 2 mm make large chambers difficult to operate. Decreasing the wire diameter would help, but mechanical and electrostatical limitations exists [49].

To handle the high rates outside the beam region, the gate of the chamber has to be kept below a few tens of nanoseconds. To operate a chamber with such a narrow gate, the distance between the anode wires has to be small and a chamber gas with a high electron drift velocity has to be used. A source of possible inefficiencies are space charge effects due to positive ions shielding the anode wires at such high rates. To minimize such effects a gas with a high ion mobility should be selected and the distance between the cathode and the anode (gap) should be kept small to reduce the drift time for positive ions from the avalanche to the cathode. A fundamental limit to the possible reduction of the gap is given by the required efficiency of the chamber. If the gas thickness is too small, a minimum ionizing particle may occasionally traverse the chamber without producing any ionization, resulting in a loss of efficiency. The inefficiency $1-\epsilon$ and the average number of primary ions N are related by $1-\epsilon = e^{-N}$. But in practice, the possible reduction of the gap is limited by the fact that for large MWPC's it becomes difficult to maintain a uniform anode to cathode distance. This is critical, since a gap variation of only a few percent changes the gain significantly [49].

Besides a large drift velocity for electrons and a high mobility for ions, the chamber gas should also show minimal degradation over time (ageing) and a large number of primary ions per unit length should be created to reduce possible inefficiencies. The constraints of thin windows to minimize multiple scattering and of a large area to maximize the acceptance dictates the operation of the chamber at atmospheric pressure. CF_4 has been identified as a fast wire chamber gas [50], producing a large number of primary electrons [51]. It is also reported that CF_4/isobutane gas mixtures do not produce any deposits on anode wires [52] at specific mixing ratios. It was found that in a region between approximately 30% and 85% CF_4 in CF_4/isobutane no ageing can be observed [53]. Yamashita *et al.* [54] measured the electron drift velocity and the positive ion mobility for different fractions of CF_4 in CF_4/isobutane. Their results are shown in Figure 3.4, indicating an increase of the drift velocity with the fraction of CF_4 but, unfortunately, also a decrease of the ion mobility. Considering all these constraints we selected a CF_4/isobutane gas mixture in the ratio 50%:50% to operate the MWPC's.

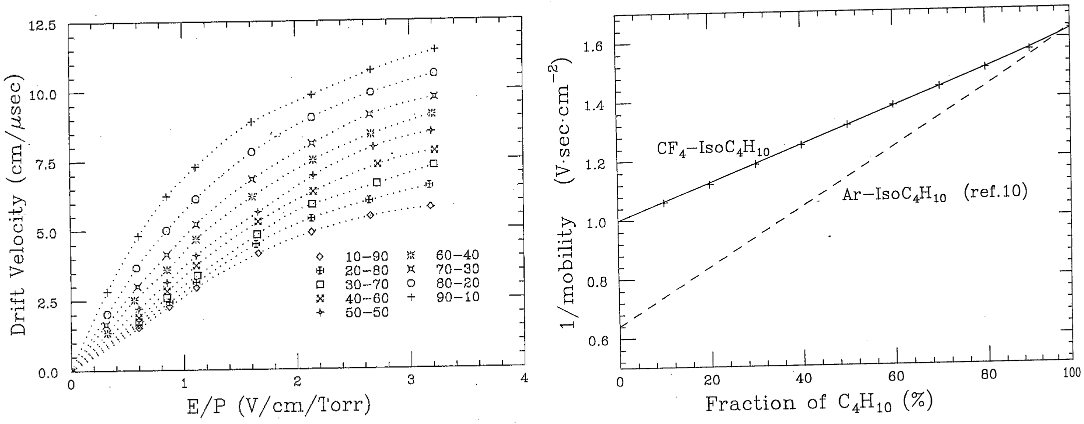

Figure 3.4: Drift velocity and ion mobility for CF_4/isobutane gas mixtures.

Due to the high beam flux, it is necessary to reduce the sensitivity of the chamber in the beam region ('dead area'). The technique used will be described in section 3.5.2.

3.5.2 Construction of the chambers

There are some differences in the construction between P1/P2 and P3/P4, respectively. In the following sections the chambers P1/P2 will be described. These two chambers were built in the workshop of the Physik Institut of the University of Zürich. Significant differences for P3/P4 will be mentioned.

The dimensions of the chambers are summarized in Table 3.2. Each chamber consists of four types of anode wire planes corresponding to a different orientation of the wires: horizontal, vertical and inclined at $\pm 19.4°$ with respect to the vertical direction, five cathode planes, two ground planes and two gas window planes supported by an aluminum and a steel frame (Fig. 3.5).

Chamber	Active area	Dead area
P1	160×80 cm^2	19×9 cm^2
P2	160×80 cm^2	30×10 cm^2
P3	300×140 cm^2	55×16 cm^2
P4	320×160 cm^2	70×26 cm^2

Table 3.2: Size of MWPC's. The areas are given in horizontal dimension multiplied by vertical dimension.

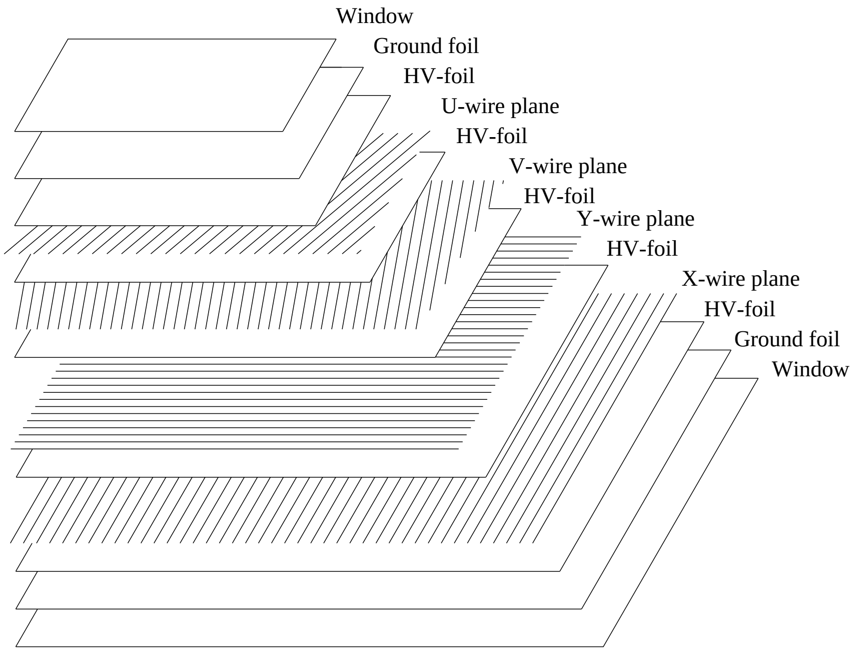

Figure 3.5: Cross section through P1.

The anodes are made of gold plated tungsten wires (diameter $2a = 20$ μm) [55] with a spacing of $s = 2$ mm. The gap width is $l = 5$ mm. The wires are soldered on both sides to gold plated solder points on printed circuit boards about 1 cm from the inside edge of the frame (Figure 3.7). On one side, the printed circuit is extended to the outside edge where the connectors for the readout electronics are mounted. The printed circuit boards are glued to a frame made of glass fibre reinforced epoxy resin (Stesalit [56]). The wires are positioned relative to reference points on the frame using for the first wire of a plane a measuring device attached to the reference points and for the following wires a comb with a spacing of 2.0 ± 0.0002 mm. The position of each 200 wires is checked against the reference point with the measuring device. For soldering the wires a solder without flux with a melting-point at 140°C is used. To reduce the electrical field at the outermost wires three edge wires of increasing diameter (30 μm, 50 μm and 100 μm) are added. Following Sauli [49], we calculate a capacity C per unit length:

$$C = \frac{2\pi\epsilon_0}{\pi l/s - \ln(2\pi a/s)} = 4.92 \text{ pF/m} \tag{3.1}$$

Since a wire of the type used breaks at 0.9 N, a safe tension T is 0.7 N [57]. Using this value, the maximal potential difference V_c between the electrodes before the anode wires are displaced can be calculated. For $L = 80$ cm long wires we get [49]:

$$V_c = \frac{s}{CL}\sqrt{4\pi T} = 4485 \text{ V} \tag{3.2}$$

Consequently, we get for $L = 160$ cm long wires a maximal potential difference of 2243 V. This is well below the operation point of a MWPC. Therefore we supported the horizontal wires by a 3 cm wide and 0.2 mm thick printed board glued with a double sided tape to a 3 cm wide and 50 μm thick Kapton foil [58]. This support structure is clamped to the Stesalit frame and the horizontal wires are soldered to solder points on the printed board and divided in the middle. This structure does not only support the wires but also allows to separate the horizontal wires into a left and a right side. For the larger chambers P3 and P4 nylon threads are woven in addition in pairs alternating through the sense wires and garlands [59] bent into a zig-zag shape are mounted on the frames to keep the anode wires stable against electrostatic forces between the planes. The tension of the wires was monitored electronically by measuring the resonance frequency of the wires and a mean value of 0.681 N with a spread of 0.017 N was found.

The cathodes are made of 50 μm thick Mylar foil [60]. The foils are stretched by pulling them around the edges into an evacuated groove. Then they are glued on Stesalit frames with Araldit [61] and sprayed twice with high resistance graphite. The surface is polished after each spraying process. At the end the graphite layer is approximately 40 μm thick and the resistance is 1.7 kΩ per square after one hour heat treatment at 100°C. The graphite layer is made from a mixture of DAG502 [62] and isopropanol in the ratio 1:1. Before the spraying process, a mask is applied to the foil in order to define the conductive surface. The graphite layer is divided into four electrically separated areas (Figure 3.6). The two central areas can serve as 'beam killers' (dead zone), the voltage of these areas can be lowered so that gas amplification will be strongly reduced. The sizes of the dead zones for the individual chambers are given in Table 3.2. All the edges of the graphite areas are rounded, removing the graphite with isopropanol, borders are cleaned with an ordinary pencil eraser and polished with Q-tips. The zones separating the graphite areas are cleaned with isopropanol, too. No high voltage breakdown from the front to the back side of the Mylar foil is observed up to 6 kV difference, across the 3.5 mm gap between the graphite areas up to 3.5 kV could be upheld. A printed circuit is used to supply the cathodes with negative high voltage (Figure 3.6). A flattened copper wire glued to the graphite with conductive epoxy [63] connects the graphite with the printed circuit. Each graphite area can be fed individually with high voltage. The cathodes are protected with 512 kΩ resistors to allow a high voltage degradation in case of a spark between the electrodes or a broken wire. In P3 and P4 a line of painted silver epoxy connects the graphite with the high voltage feed in and the front and the back sides of corresponding graphite areas are shorted with pin holes in the mylar foil.

The frames of the electrodes are not self-supporting. They are therefore assembled between a 2 cm thick aluminum frame and a 2 cm thick steel frame stiffened by a U-profile (Figure 3.7). Twenty-eight precisely drilled holes in the support frames and in the Stesalit frames fix the position of electrodes with respect to the chamber reference system. The chamber is assembled by means of 28 hollow steel bolts which are passed through the holes. This system allows the chamber to be easily opened and direct access to each electrode using expandable dowels.

The windows of the chambers are made of a Mylar-aluminum sandwich foil (12.7 μm aluminum evaporated on a 12.7 μm thick Mylar foil). The aluminum foil is necessary to prevent water vapor from penetrating the chamber and to screen the anode wires from electronic noise. This foil is glued with Araldit to the aluminum and steel frame, respectively. The aluminum foils and the frames are connected electrically by means of silver epoxy lining the corner between the frame and the foil (Figure 3.7). All Stesalit frames extending out of the chamber are wrapped with a copper foil, individual Stesalit frames are 'connected' together with metallic braids passed around PVC-tubing and pressed into the empty space between the frames (Figure 3.7), resulting in a Faraday cage around the chamber.

An open loop gas system flushes the MWPC's. The gas tightness is secured by conventional O-rings, glued into a groove in each Stesalit frame. This requires double sided circuit boards to read out the anode wires, i.e. boards with the copper lines, which connect the wires with the connector, not on the outer, visible side, such that the O-ring does not have to press against an uneven surface.

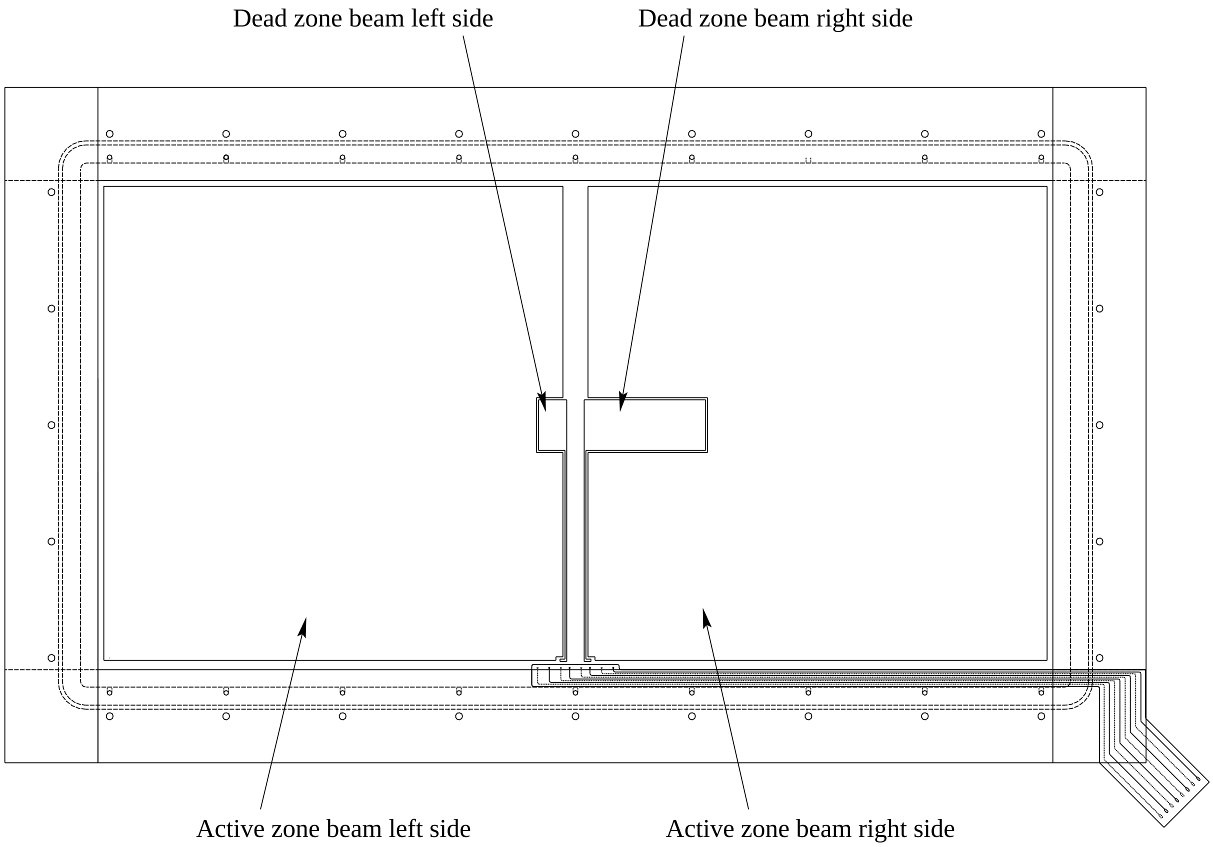

Figure 3.6: Cathode plane for P1.

Two additional 50 μm thick mylar foils (ground foils) sprayed on one side with a graphite spray and connected to ground are added to the package (Figure 3.7) to prevent the outermost cathode from sagging towards the anode caused by electrostatic forces. Since the capacity between the ground foil and the cathode is larger than between the anode wires and the cathode, the high voltage of the graphite areas facing the ground plane is lowered to 80% of the voltage of the other active areas of the cathode.

3.5.3 Electronics

Most of the signal from the anodes is induced by the motion of the positive ions from the anode towards the cathode. The accumulated charge q depends on the time as $q(t) = -q_0 \ln(1 + t/t_0)$. The characteristic chamber constant t_0 in our case is approximately 2 ns. Important for high counting rate applications is that a substantial fraction of the signal charge is collected in a relatively short time, a few t_0, although the signal current continues for a long time (typically hundreds of μs). The first condition provides the basis for high

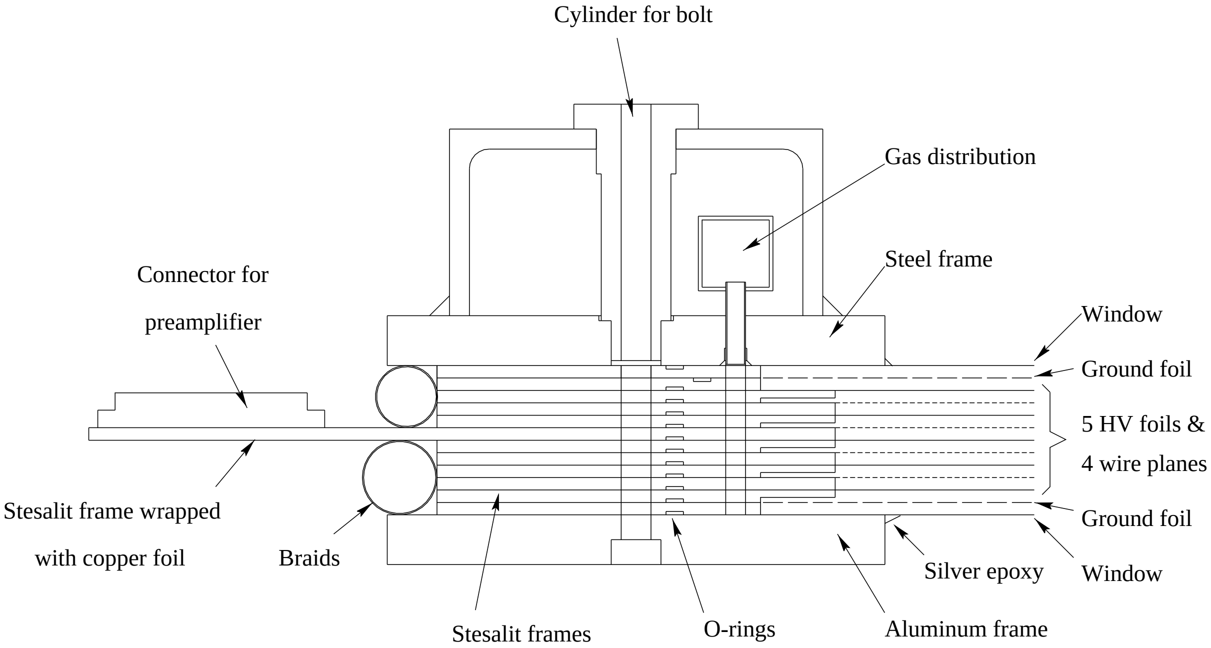

Figure 3.7: Cut through the MWPC frame.

rate counting, i.e. that sufficient signal charge relative to the electronic noise is collected in a short time. The long 'tail' of the signal however tends to obscure the measurement of any following signals.

E865 uses a new MWPC readout system (PCOS4) designed by our collaborators from Yale University together with LeCroy corporation. It consists of a preamplifier and shaper chip and a discriminator, delay, latch and readout chip. A block diagram of these chips is shown in Figure 3.8.

The LeCroy MQS104 integrated circuit contains a preamplifier and a shaper. It is implemented in a medium performance semi-custom bipolar process. The filtering consists of four poles and one zero. The output pulse width is 18 ns (FWHM) with 11 ns rise time and 23% undershoot. The undershoot is intended to cancel the 'tail' of the signal mentioned above. The double hit resolution is less than 80 ns. The effective noise level is less than 3000 electrons, with protection elements and wire capacitance added to the input circuit. The transimpedance gain is 500 kΩ with differential output. Each chip contains four independent channels.

The second integrated circuit (LeCroy MDL108) combines the discriminator, delay element, coincidence gate and readout logic in an 8-channel BiCMOS chip. The discriminator, adjustable down to below the noise level, is followed by a one-shot producing a fixed output pulse width. The delay element, which is used to adapt the timing of the individual channels to the timing of the coincidence gate sent by the trigger, is adjustable

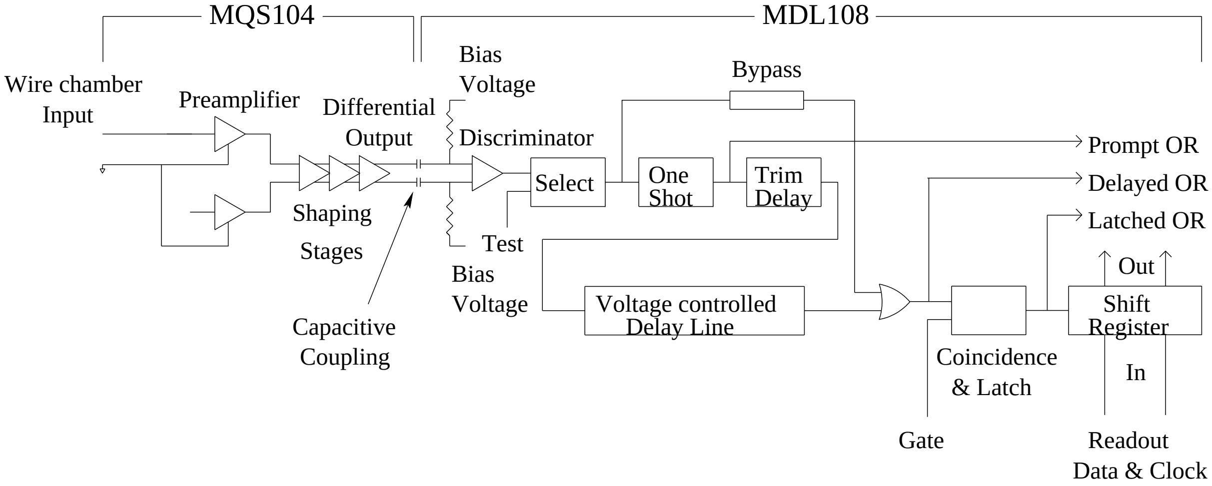

Figure 3.8: Multiwire proportional chamber electronics block diagram (PCOS4).

from 330 ns to 1 μs. The first section of the delay is a trim section with 16 fixed steps of approximately 1 ns. These trim sections allow all channels of the chamber to be adjusted to have the same delay with an error less than 2 ns. A delay line follows consisting of 150 current limited inverter stages, each with a minimum delay of 2 ns and a maximum of at least 6 ns. The delay lines are controlled by a phase lock loop and a ninth delay line, the reference delay, which is identical to the eight signal delay lines. In phase lock loop mode, a pair of gate pulses with a separation equal to the desired delay is input to the delay line. Detection circuitry determines whether the delay is greater or less than the desired delay and sets a direction bit accordingly. An initial calibration period with several thousand pulse pairs is required to set the proper delay value. Then a calibration every few seconds is necessary to track changes in temperature and power supply voltage. The coincidence is made in an edge triggered D flip-flop. The leading edge of the delayed one-shot output clocks the flip-flop, the coincidence gate is the D input. The output sets a simple set-reset flip-flop. During readout, the set-reset flip-flop output is transfered to a shift register. The shift register is 9 bits long, the eight data bits for the eight channels and one parity bit to identify transmission errors. The system is designed to be read out at a 20 MHz shift rate. There are three OR outputs, a prompt OR (the OR of the eight one-shot outputs), a delayed OR (the OR of the eight delay lines outputs) and a latched OR (the OR of the eight set-reset flip-flops).

Four MQS104 and two MDL108 chips are combined on a card. This card is designed to be mounted on the chamber (plugged into the connector shown in Figure 3.7). A second connector on the card plugs into a common motherboard. One to sixteen of these cards (max. 256 wires) are connected to one motherboard and are organized in a daisy chain, with the readout linked together in one long shift register. This motherboard also distributes power, gate and fast clear signals. The power consumption of one channel is 285 mW. Setting up the system requires down-loading 16 bytes for each MDL108 chip, running the system in phase lock loop mode for adjusting the delays and returning to normal running mode. The LeCroy 2748 Camac modules accomplish this tasks. Additionally, these Camac modules provide an OR which is used in the fourth level trigger (section 3.10.2).

3.5.4 Chamber performance

Conditioning the chamber required unusual care. It took a few months during which three wires in P1 and one in P2 were broken before a voltage well above the expected operation point was reached. It was tried to speed up this process by applying a voltage of opposite polarity to the electrodes for a short time, but no progress was observed using this method.

During bench tests using a ^{241}Am source producing a current density comparable to the beam the chamber produced at certain positions a dark current of up to 10 μA which was not immediately self-quenching when the source was removed. Usually the current continued to burn for a few hours. After if stopped, the chamber could be illuminated at the same position for many hours without the occurrence of any current. This was observed more often at the edges of the graphite area than in the center.

The uniformity of the chamber gain was tested twofold. We got a rough idea of the uniformity by scanning the chamber with the ^{241}Am source and comparing the currents drawn. No variations of more than 17% were found in any plane or between different planes. More accurate information was obtained by measuring gain curves at different positions on the chamber with a ^{55}Fe source. Figure 3.9 shows one of the curves. We also found with this method no variation larger than 15%. After this test, the chamber was installed in the experiment.

A plateau curve for P2 at nominal amplifier threshold is shown in Figure 3.10. It is measured using so called 'beam muons'. These are high energy muons originating from the target with the AGS running but all magnets of the secondary beam line switched off. P1 and the calorimeter are used as trigger.

Under regular beam intensity no increase of the efficiency could be observed by raising the high voltage above 3280 V, the voltage drop over the 512 kΩ protection resistors is less than 10 V. The chamber is operated during most of the time at 3280 V. The dead zone is set to 2600 V, no gas gain is observed at this voltage. Due to the high rate a few hits still occurred in this region, since the chamber operates as an ionization chamber.

We also tried to mix 0.1% of water to the gas by bubbling 8% of the isobutane through water held at 22^{0}C to avoid sparks. Due to the lack of a continuous gas flow monitoring,

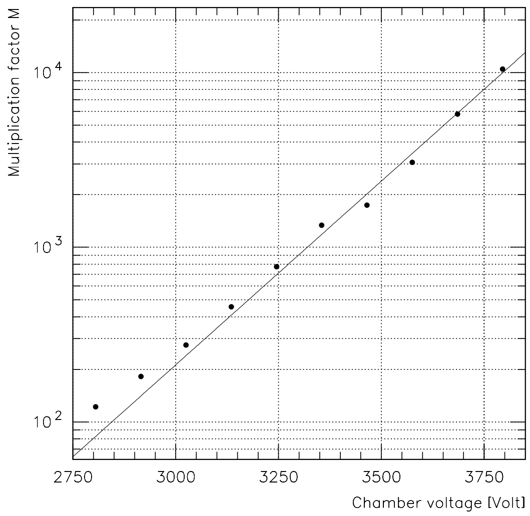

Figure 3.9: Gas gain in P2 for CF_4-iC_4H_{10} gas mixture.

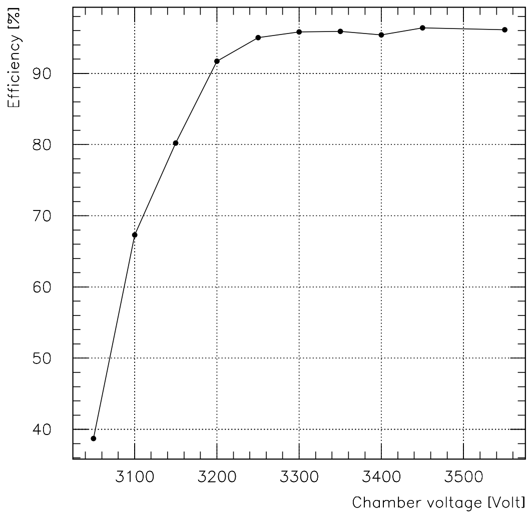

Figure 3.10: Efficiency curve for P2 using beam muons.

it is almost impossible to control the admixture and a loss of efficiency was observed. Hence, we continued to operate the chambers without an admixture of water.

Up to now (summer 1997), P1 ran for fifty weeks without any problems. The Y-plane of P2 started to trip off towards the end of the run in 95. A replacement of the support strip and the Y-wires solved this problem. The chamber accumulated up to now about 0.01 C/cm on the wires just outside the dead zone and no loss in the net efficiency can be observed.

With P3/P4 we had problems caused by electrostatic forces to bring them up to the operation point. Finally, we decided to run the two chambers with a gas mixture of 79.5% argon, 20% isobutane and 0.5% CF_3Br. No change in the main chamber parameters (efficiency, background rate, leakage current) have been seen.

Figure 3.11 shows delay curves for various gate widths in CF_4 - C_4H_{10} at 3280 Volts at nominal amplifier threshold. No delay calibration for the individual channels was done for this measurement, in fact, we didn't succeed to calibrate the delays until the end of the run in 95. We operated P1/P2 with a gate width of 60 ns and P3/P4 with a gate width of 85 ns during the run in 95. After we understood the calibration process, we were able to narrow the gate for P1/P2 to 40 ns and for P3/P4 to 60 ns, considerably reducing the accidental rate.

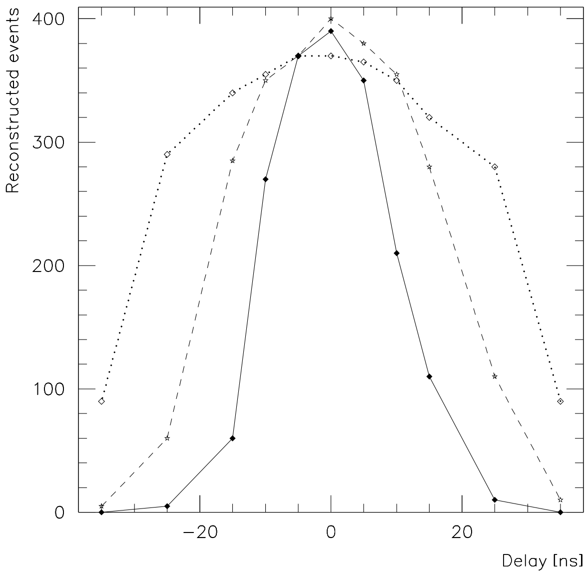

Figure 3.11: Delay curves for a 40 ns wide gate (solid), a 60 ns wide gate (dashed) and a 75 ns wide gate (dotted).

3.6 Čerenkov counters

3.6.1 Design and construction of the Čerenkov counters

The two Čerenkov threshold counters C1 and C2 are intended to separate electrons from pions and muons. In order to maximize the geometric acceptance of the decay particles, which is mainly limited by the size of the second spectrometer magnet, the detector has to be kept relatively short. This limited the amount of Čerenkov radiator which could be presented to the incident particles. Furthermore, Monte Carlo studies indicate that multiple scattering would be a limiting factor for the momentum resolution in the experiment. In order to keep the material in the detector to a minimum, the Čerenkov gas is held at atmospheric pressure. This is also required by the necessity of keeping delta ray production down, which dictates that the windows of the counters be kept thin. Background due to delta rays is of course also suppressed by the arrangement of the two counters sandwiching D6. Rays produced downstream of C1 and giving light in this counter are swept away by the magnet, preventing coincidences between C1 and C2. Finally, there is the requirement, that the counters should not identify a pion and a muon as electrons on the left side and, simultaneously, that it should not identify positron as a pion or as a muon on the right side as mentioned in section 3.1.

A choice of hydrogen ($n - 1 = 1.4 \times 10^{-3}$, where n is the refractive index of the gas) as the left side radiator and CO_2 ($n - 1 = 4.1 \times 10^{-3}$) as the right side radiator satisfies these demands. Hydrogen is selected since its high threshold (muons 6.3 GeV/c, pions 8.4 GeV/c) allows the highest possible beam momentum with the beam particles below the threshold. Hydrogen is also the best choice since the production of delta rays is proportional to the density of atomic electrons. The high threshold of hydrogen also prevents the detection of delta rays with a momentum less than 30 MeV/c. The disadvantage of this choice is that only 2.0 photoelectrons in each counter per electron track can be expected. Poisson statistics then dictates that each counter will be 14% inefficient, giving the left side about a 75% detection efficiency for electrons when requiring a coincidence between the two counters. Since the number of emitted photons is proportional to $(1 - 1/n^2\beta^2)$ [64] where n is the refractive index of the gas, the right side radiator CO_2 yields almost three times as many photons as hydrogen. This yield makes the counters on the right side nearly 100% efficient. The choice of CO_2 also insures that any inefficiency due to high energy muons and pions giving light in the counters would be minimal, as the 3.7 GeV Čerenkov threshold for muons and the 4.8 GeV threshold for pions is just at the end of the predicted spectrum for $K_{\pi\mu e}$.

A main disadvantage of hydrogen is its explosiveness. Proper sealing of the gas volume becomes a major concern. Figure 3.12 shows the design of the Čerenkov counters. It is based on a shell welded from four aluminum plates to form an integral part of the gas envelope. A 100 μm thick outer aluminized Mylar foil (in C2 a 25 μm thick Mylar foil) and a 50 μm thick inner Kevlar foil (in C2 150 μm), separated by 5 cm flushed with CO_2 for safety reasons, make up the upstream and downstream windows of the counters. The mylar foil is left slack so that the tensive forces are entirely supported by the Kevlar, hence the containment is not limited by the mechanical strength of the mylar. A septum made of a 50 μm thick Kevlar foils sewn to the windows, divides the gas volume into two halves. Since the beam passes through the Čerenkov counters on their right side, the septum is pushed to the left by a slightly higher pressure on the right side to move it out of the beam. The windows are sealed to the shell with a castable polyurethane gasket with bolt holes through the gasket. The septum has a similar gasket. No leaks have been detected under helium testing of 150% of the design pressure.

Čerenkov light in C1 is focussed by a system of primary and secondary mirrors onto one of the eight photomultiplier tubes mounted in aluminum caps on top and on bottom of the shell. C2 uses 24 photomultiplier tubes to cover the whole solid angle. A set of primary mirrors focuses the light directly onto these tubes. Since the distribution of the Čerenkov photons becomes asymmetric in X and in Y due to the horizontal dispersion of the particles in the magnetic field, fairly complicated astigmatic mirrors are needed. The mirror construction for both C1 and C2 uses the idea of a complex mirror made of smaller components (Fig. 3.12) . Each component is an element of a cylinder with a small 'secondary curvature' across the narrow side of the mirror element to make the bend more continuous. It consists of 760 μm Acrylic with a backing of 1000 nm of aluminum and is supported by a Rohacell frame. The mirror reflectivity is 90% for wavelengths above 400 nm, then it slowly starts to drop to 85% at 250 nm. Below 250 nm it falls off more rapidly to 70% at 200 nm.

The photomultiplier tubes (PMT's) are Burle 8854's with a diameter of 12.7 cm. Their window transmits UV-light down to 250 nm and their first dynode made of GaP provides a first electron multiplication of approximately 20, necessary for single photoelectron detection. The PMT's are mounted very close to the magnets and therefore need to be shielded from stray magnetic fields affecting the electron collection system and causing a drop in the collection efficiency. The shielding consists of a heavy plate to shunt field lines away from the PMT region, followed by heavy shielding plates, soft electrical conduit and inner mu-metal cylinders. To prevent the PMT's of becoming magnetized as well, the shielding is separated from the PMT by both a magnetic insulator and more iron. By means of these installations the magnetic field is reduced from $80-100$ Gauss to 0.5 Gauss at the tubes. The quantum efficiency of all PMT's is at least 90% of the efficiency with the magnetic fields off.

Since pions in the primary beam have energies above the Čerenkov threshold in CO_2,

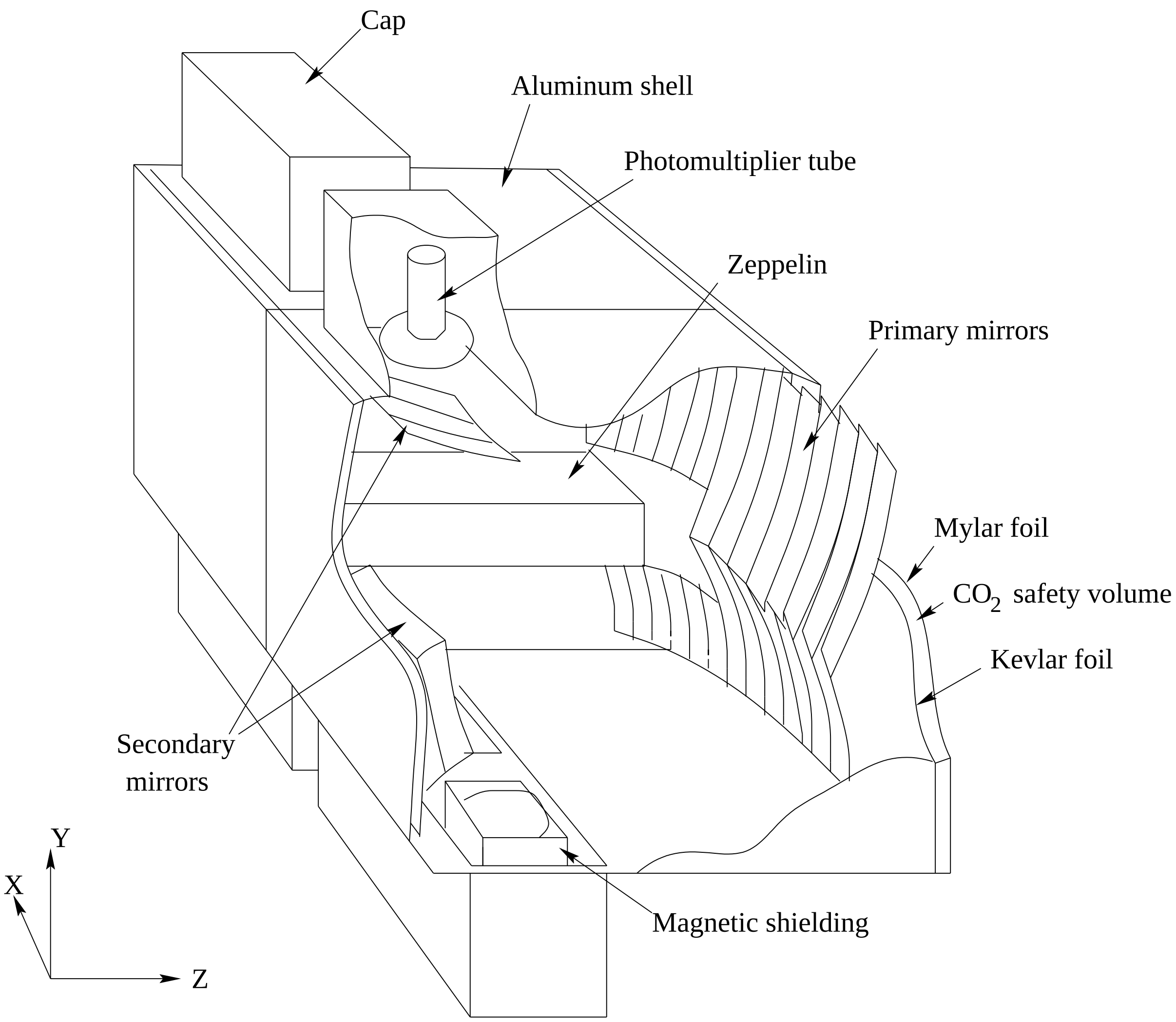

Figure 3.12: Sketch of the C1 Čerenkov counter. Differences between C1 and C2 are described in the text.

it is necessary to suppress this light. This is done by surrounding the beam in the counters with a 'zeppelin' made of 38 μm thick polyurethane filled with hydrogen.

3.6.2 Performance of the Čerenkov counters

Figure 3.13 shows the efficiency in the Čerenkov counters as a function of the position of the track at the mirror plane as measured by dedicated Čerenkov efficiency runs, requiring an OR of the two counters. As expected the left sides of the counters ($X > 0$) are less efficient, due to the lower yield of photoelectrons. The zones with zero efficiency correspond to blinded regions near the beam.

	-200 / -110	-110 / -90	-90 / -30	-30 / -10	-10 / 0	0 / 10	10 / 30	30 / 90	90 / 110	110 / 200
60 / 20	96.9	93.1	99.6	98.3	0.0	0.0	78.0	84.1	77.5	78.7
20 / 10	92.4	93.3	99.4	98.5	0.0	0.0	71.3	83.2	76.8	80.5
10 / 5	74.1	88.8	99.1	0.0	0.0	0.0	72.7	76.8	70.4	75.7
5 / 0	77.5	86.8	97.9	0.0	0.0	0.0	70.2	66.0	60.5	73.5
0 / -5	97.4	94.4	98.3	0.0	0.0	0.0	51.9	65.2	52.8	71.3
-5 / -10	99.2	94.7	98.2	0.0	0.0	0.0	78.5	67.7	58.5	72.8
-10 / -20	98.6	94.4	97.9	46.2	0.0	0.0	50.1	70.7	65.9	81.2
-20 / -60	99.3	94.1	99.2	84.1	0.0	0.0	51.5	72.6	72.2	86.8

	-200 / -140	-140 / -100	-100 / -80	-80 / -60	-60 / 0	0 / 30	30 / 80	80 / 100	100 / 140	140 / 200
80 / 40	94.7	99.1	98.4	96.6	98.9	63.9	79.9	83.4	87.3	77.6
40 / 30	97.5	99.9	99.0	80.4	97.3	72.4	58.5	72.2	83.5	70.5
30 / 10	94.1	99.9	99.5	90.0	99.1	76.2	69.4	78.7	85.0	84.2
10 / 0	93.3	99.6	99.7	95.7	99.2	0.0	76.3	81.9	81.3	86.9
0 / -10	97.0	99.4	99.5	89.2	93.5	0.0	89.0	82.0	84.1	88.5
-10 / -30	96.5	99.0	98.2	75.6	88.0	87.4	84.5	84.4	83.3	88.6
-30 / -40	98.1	98.2	95.9	65.2	84.8	83.3	78.3	78.9	81.2	82.6
-40 / -80	91.3	94.7	97.2	94.2	98.8	64.3	83.8	28.3	4.9	19.3

Figure 3.13: Average efficiency of C1 (top) and C2 (bottom) during the 1995 run as a function of the position of the track in the counter. The efficiencies are given in percent between ±200 cm in horizontal and ±60 cm in vertical direction for C1 and between ±200 cm in horizontal and ±80 cm in vertical direction for C2.

The most important point about the efficiencies is the positron rejection on the right hand side against positrons from K_{DAL}-decays. The rejection R is

$$R = 1/(1 - \epsilon_{C1}) \times 1/(1 - \epsilon_{C2}) \tag{3.3}$$

where ϵ_{C1} and ϵ_{C2} are the efficiencies at the track position in C1 and C2, respectively. Figure 3.13 shows, that on the right side in most of the significant regions, i.e. regions closest to the beam, the efficiency is above 97%, yielding to a rejection of more than 1000.

The important point for the performance on the left side is how many pions give unwanted light. Such light may originate from delta rays or accidental electrons from the beam, crossing the Čerenkov counter in the same region as the pion. From a sample of good K_τ events, we estimate that about 0.4% of pions in C1L and 1.1% in C2L have light associated with them. Thus the overall rejection factor for the left side Čerenkov counters for pions against electrons is $1/4.4 \times 10^{-5}$.

The pedestals, i.e. the DC-offset of the signal, are determined on a run by run basis using out-of-time data, i.e. data not assigned to a particle crossing the counters. The PMT gains are calibrated by looking for the one photoelectron peak from ELER triggers (see section 3.10.2 for a definition of the trigger types). Figure 3.14 shows the PMT response on electrons and positrons in C1 and in C2. The one- and two-photoelectron peaks are clearly recognizable. On average, we find 1.7 photo electrons on the left side and 4.2 photoelectrons on the right side.

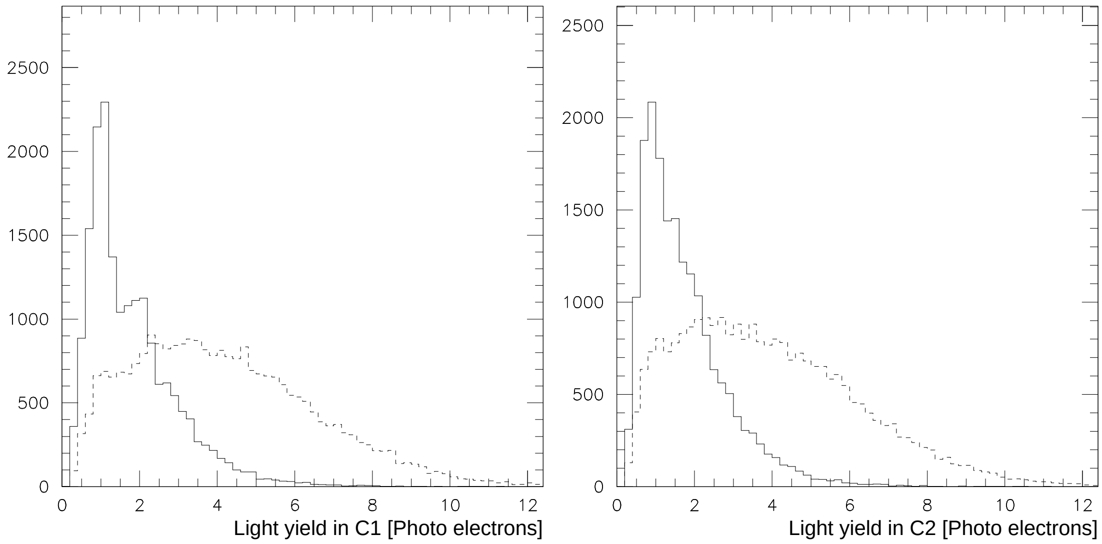

Figure 3.14: Number of photoelectrons in the left side (solid), filled with hydrogen, and the right side (dashed), filled with CO_2, Čerenkov counters.

3.7 Electromagnetic calorimeter

3.7.1 Mechanical construction

The electromagnetic calorimeter is a lead/scintillator sandwich sampling calorimeter read by wave-length-shifting fibres, called 'Shashlik'. It consists of 30 modules in the horizontal and 20 modules in the vertical direction, covering the whole solid angle. 6×3 modules are left out in the center of the calorimeter to give room for the beam. This is shown in Figure 3.15.

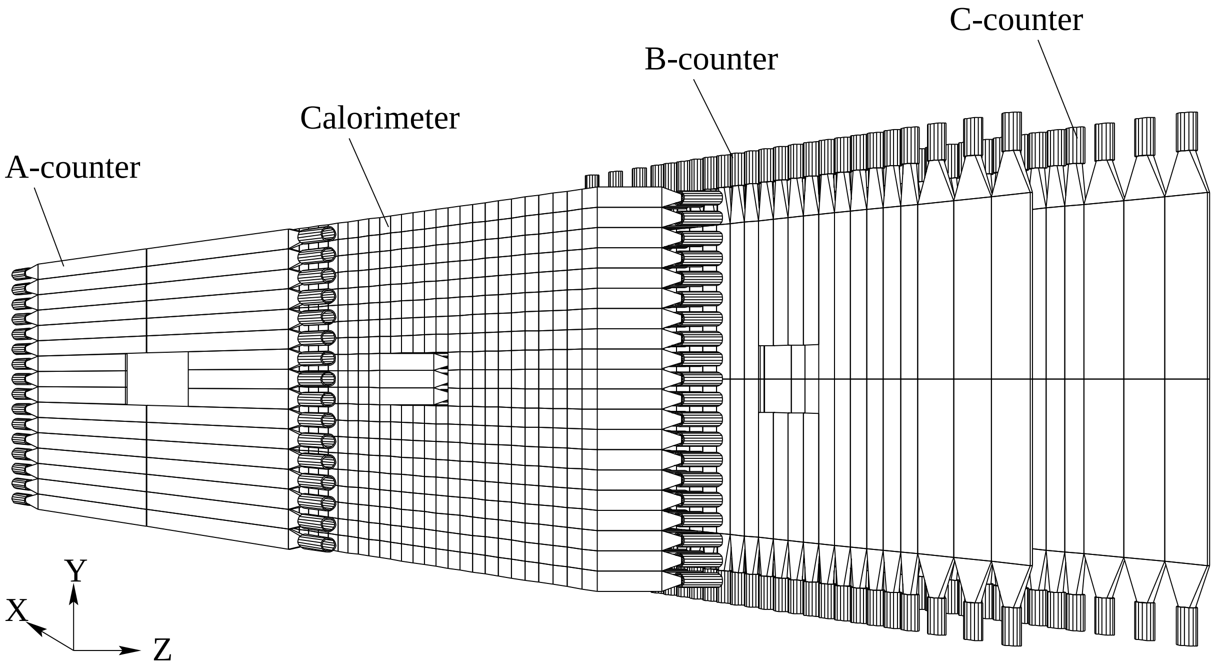

Figure 3.15: Arrangement of the calorimeter and the hodoscopes. The A-counter is moved 1.5 m upstream in this drawing.

As the design of a module is described elsewhere [65] in great detail, we will mention here only the most important points. Figure 3.16 shows a single module consisting of perforated lead plates alternating with plastic scintillator plates 1.4 ± 0.005 mm and 4.0 ± 0.05 mm thick, respectively. Altogether, there are 60 layers with a total thickness of 15 radiation lengths. The transverse dimensions are 11.4×11.4 cm^2, corresponding to 2.5 Molière radii. The light is collected by 144 wavelength shifting fibres with a diameter of 1.2 mm inserted into holes in the scintillator and lead plates. The selected number of fibres ensures an almost complete absorption of scintillation light at any emission angle. To reduce the contribution of the constant term to the energy resolution, each fibre is viewed by photomultiplier tubes at both ends. This is done by making a loop with a radius of 3 cm at the front of the module (Figure 3.16). White paper used as reflecting surface is placed between the lead and scintillator plates. The whole module is wrapped into aluminized mylar and tied up with four 100 μm thick steel strips from each side to provide rigidity.

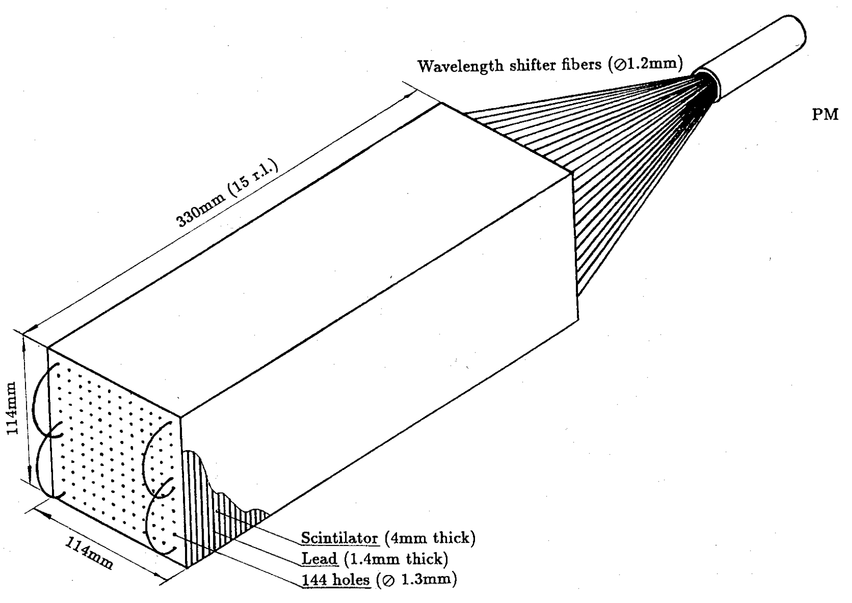

Figure 3.16: Calorimeter module.

Number of modules	582
Lateral size	11.4×11.4 cm^2
Number of planes	60
Scintillator/lead	4.0 ± 0.05 mm / 1.4 ± 0.005 mm
Total radiation length	15
Radiation length	21.6 mm
Molière radius	45 mm
Attenuation length in scintillator	30 cm
Scintillator	Polystyrene & P-terphenyl & POPOP
WLS-fibres	Polystyrene (core), PMMA (cladding) ∅1.2 mm
Number of fibres	144
Interfibre distance	9.6 mm
Attenuation length in fibres	1.2 m
PM-tube	FEU-84 & FEU-115
Contact between fibre and PMT	Direct contact, no optical grease used

Table 3.3: Parameters for calorimeter.

3.7.2 Performance of the calorimeter

Figure 3.17a shows the energy resolution of the calorimeter as a function of the energy. The resolution deduced from K_{DAL} data can be described by the formula

$$\delta/E = 0.022 + \frac{0.068}{\sqrt{E(GeV)}} \tag{3.4}$$

The most crucial point in the performance of the calorimeter is the π/e rejection. It is a well known fact that the level of pion rejection is limited by such processes as charge-exchange reactions, where all or almost all of the energy of the pion is transfered to a neutral pion. If this reaction occurs within the first few radiation lengths, such an event will be practically impossible to distinguish from an electromagnetic shower generated by an electron with the same energy. Figure 3.17b shows the deposited energy in the calorimeter divided by the momentum of the track (E/P) for pions and electrons of 1.5 GeV energy. The tail of the pion distribution is due to the effect mentioned above. Tables 3.4 and 3.5 summarize the E/P response of the calorimeter for pions and electrons. One finds a rejection factor $r = \epsilon_\pi/\epsilon_e$ for pions, using only E/P, of 13% for 1 GeV particles, 5% for 2 GeV particles and 3% for 3 GeV particles at $\epsilon_e = 0.9$ (as reference Fig. 5.4 shows the momentum spectrum of daughter particles). Additional separation can be obtained by considering the transverse shower development. This feature is not used in this analysis.

The suppression of signals from calorimeter modules (and also from A-counter slabs but not from Čerenkov counter PMT's) with no hits is turned off by the data acquisition system for one in 200 spills in order to determine the pedestals. Cosmic events, taken in between the AGS spills, provide an ideal source to determine the pedestals of the calorimeter and also of the A-counter. This is done again on a run by run basis.

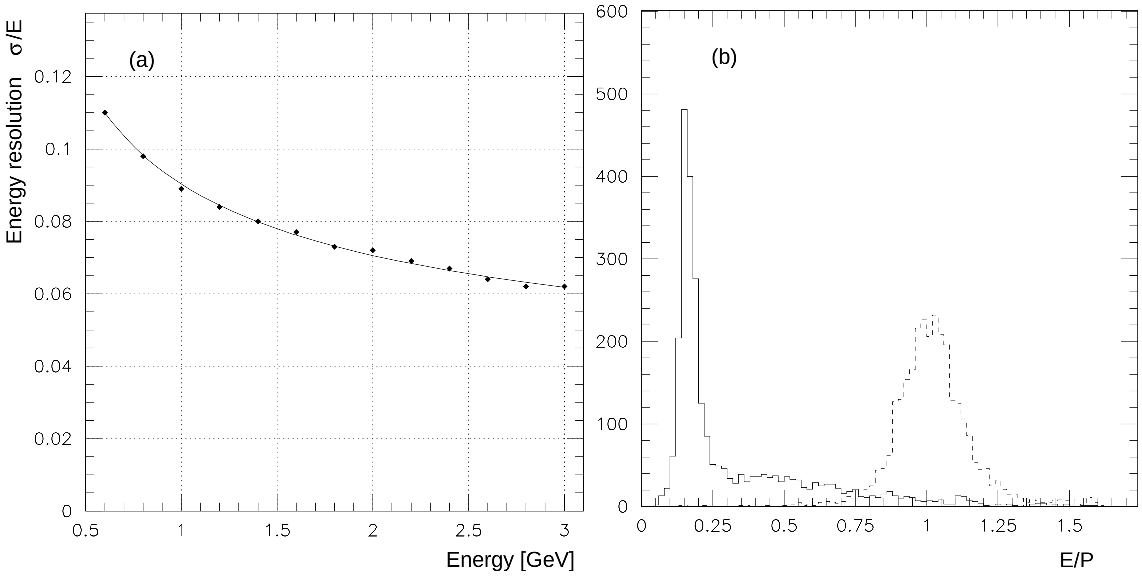

Figure 3.17: a) Energy resolution as a function of the energy. The fit is based on formula 3.4. b) Deposited energy in calorimeter divided by the momentum of the track for 1.5 GeV pions (solid) and 1.5 GeV positrons (dashed).

E/P	0.5	0.6	0.7	0.8	0.9	0.95
1.0 GeV	27	22	18	15	13	11
1.5 GeV	22	16	12	8.8	6.4	5.3
2.0 GeV	20	13	8.3	5.4	3.5	2.8
2.5 GeV	20	13	7.8	4.7	2.6	1.9
3.0 GeV	19	11	6.2	3.4	1.9	1.4

Table 3.4: Percentage of pions of a given momentum with an E/P greater than a given value (ϵ_π).

E/P	0.5	0.6	0.7	0.8	0.9	0.95
1.0 GeV	99.8	99.5	99.4	98.7	95.9	74.0
1.5 GeV	99.5	99.1	98.4	96.2	86.4	74.7
2.0 GeV	99.3	98.7	97.9	96.4	86.0	72.2
2.5 GeV	98.9	98.0	96.7	94.1	83.5	68.1
3.0 GeV	97.8	96.3	94.9	92.9	79.7	63.4

Table 3.5: Percentage of electrons of a given momentum with an E/P greater than a given value (ϵ_e).

3.8 Hodoscopes

Three trigger hodoscopes were installed during the 1995 run, called A-, B- and C-counter. The A-counter is used together with the calorimeter for the fastest trigger level of the experiment, the B- and the C-counters are used for the muon trigger. The A-counter consists of 30, the B- and the C-counter each of 48 slabs. The arrangement of the slabs is shown in Fig. 3.15. The T2 trigger level requires a horizontal arrangement of the A-counter slabs (see Chap. 3.10.2). For the B- and the C-counter a vertical arrangement of the slabs is preferred, providing the counters with a finer segmentation and reducing the time jitter. A slab is 1 cm thick and 11.4 cm wide matching the size of the modules in the calorimeter (the three outermost slabs of both sides in the B- and C-counter are twice as wide). Since the maximum length of a slab is 1.6 m, we used Bicron 408 scintillator, which has an attenuation length of 3.8 m for the emitted scintillation light compared with 2.5 m for the usual NE102A. The decay time is 2.1 ns. The slabs are connected on one side to a light guide made of UVT Lucite, which is read out by Philips XP2020s (A-counter) or Philips XP2262 (B- and C-counter) photomultiplier tubes. This means, that the light of particles hitting the hodoscope in the middle of the experiment is collected later than light from particles hitting a slab close to its PM-tube. How one corrects for this delay will be described in section 3.10.2. For the A-counter, pulseheight (ADC) and timing information (TDC) are processed, from the B- and C-counter only TDC information is used.

3.9 Muon detector

3.9.1 Construction of the muon detector

A classic muon range detector is used to separate muons from pions. It consists of a stack of twelve proportional tube chambers, instrumented with horizontal and vertical wires and separated by steel absorber plates. It covers the whole acceptance of the detector for identifying positive and negative muons. The first chamber is placed directly behind the calorimeter. The iron plates after the first eight muon chambers are 5 cm thick, the plates after muon chambers nine to eleven are 10 cm thick and the plate after the last chamber is again 5 cm thick, adding up to four interaction lengths. The B-counter is positioned after the eighth chamber, the C-counter is the last detector in beam direction and is mounted after the last muon chamber. This is sketched in Figure 3.18.

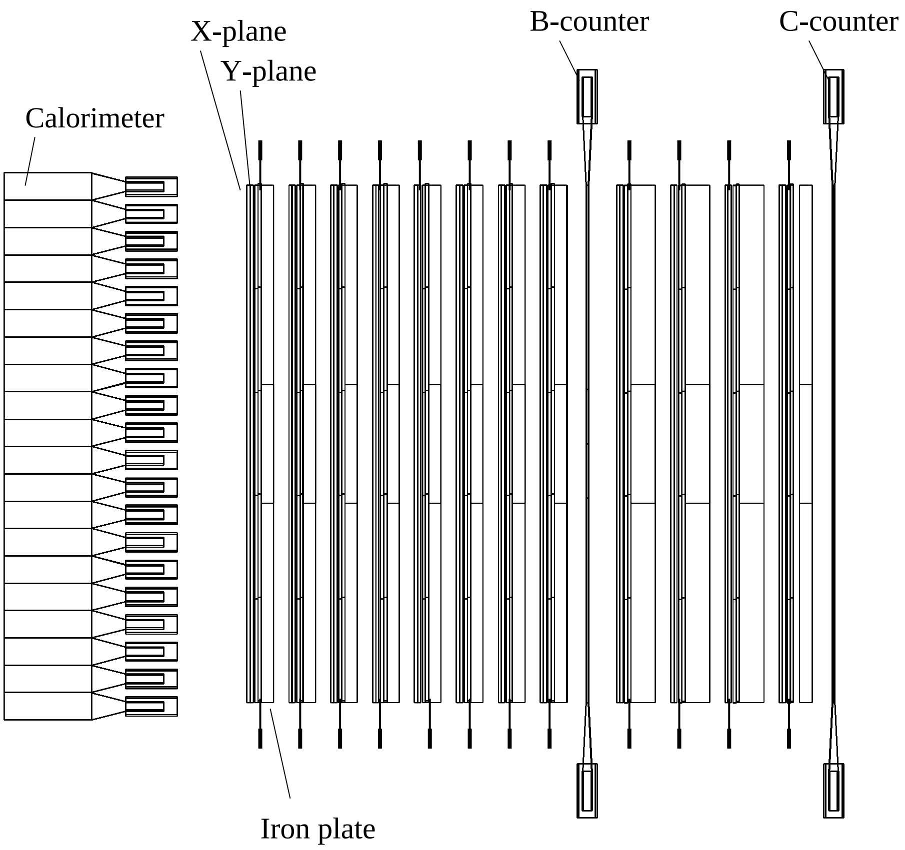

Figure 3.18: Side view of the muon detector. Also shown are the localizations of the calorimeter, the B- and the C-counter.

A chamber is comprised of individual modules with 32 read out channels each. Three walls of the cell structure of a module with two staggered layers to eliminate inefficiencies associated with particles going through the walls (Figure 3.19) is obtained from a 42 cm wide aluminum extrusion. The walls between the cells are 3 mm thick, giving the module some rigidity. The inner dimension of a single tube is 1×1 cm^2, which is chosen based on expected multiple scattering. The ends of both layers of the extrusion are capped by two pieces of insulator (Vesotell) sandwiching a printed circuit board. A narrow gap between the cell structure and the end cap allows for a free gas flow and provides a common gas volume to all cells in a module. 30 μm gold plated tungsten wire is soldered under a tension of 1.6 N to the circuit boards. The solder points are located in protective pockets in the insulator. Neighboring wires on consecutive layers are connected together. A 1 mm thin aluminum plate acts as a gas window and is glued to the extrusion thereby completing the cells.

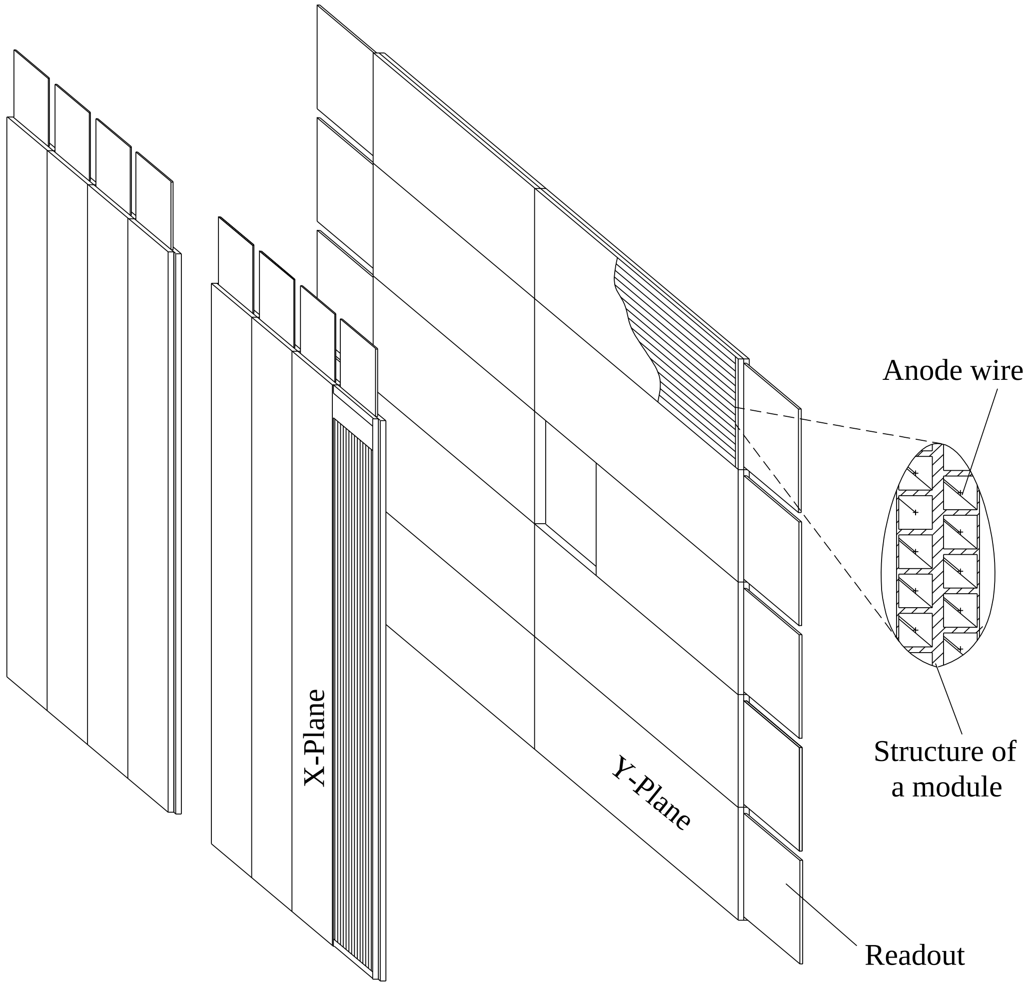

Figure 3.19: Arrangement of the modules in a X- and a Y-muon chamber plane. The cell structure of a module is enlarged.

Originally, a free region for the beam to pass was left only in the iron plates. The chambers also covered the beam region giving 32.8 cm of aluminum in the beam. The particle production caused by interactions of the beam with the material was so high that we had to remove the material from the beam region. Due to the geometry of the modules, we had to take out the corresponding module in the X-plane leading to a 30% of acceptance loss in that plane. An X-plane now consists of eight modules each 210 cm long, four on the beam left side and four on the beam right side. A Y-plane is built using ten modules. Five modules on the beam left side are 168 cm long, two modules on top and two modules on bottom on the beam right side are 210 cm long, and the central module on the beam right side is 168 cm long, making a hole for the beam (Figure 3.19).

3.9.2 Performance of the muon stack

The single most important point for the performance of the muon stack is how well pions and muons can be separated. Figure 3.20a shows a Monte Carlo simulation of the expected range of muons in the muon stack as a function of the muon energy. The step in the figure arises because double thickness iron plates are used after muon chambers 9 to 11. The threshold to reach the B-counter is below 800 MeV, just at the lower end of the momentum range of of muons in simulated $K_{\pi\mu e}$ events. To reach the end of the stack, a muon needs about 1.2 GeV. This allows to calculate an expected number of hits in the muon chambers. Muon tracks with momenta above 1.2 GeV are expected to have a hit in all twelve chambers, for those of lower momenta the expected number of hits is given by Fig. 3.20a. Figure 3.20b shows the ratio of the number of hits found in a muon track divided by the expected number of hits. Typically about 80% of the expected number of hits are found, i.e the chambers are about 80% efficient (a more detailed examination of the efficiencies can be found in [66]). Figure 3.20b also shows the same ratio for pions. Using only the range information in the muon chambers, a separation between pions and muons in the order of 20% is possible. Additional separation will be obtained using the information from the B-counter and the calorimeter.

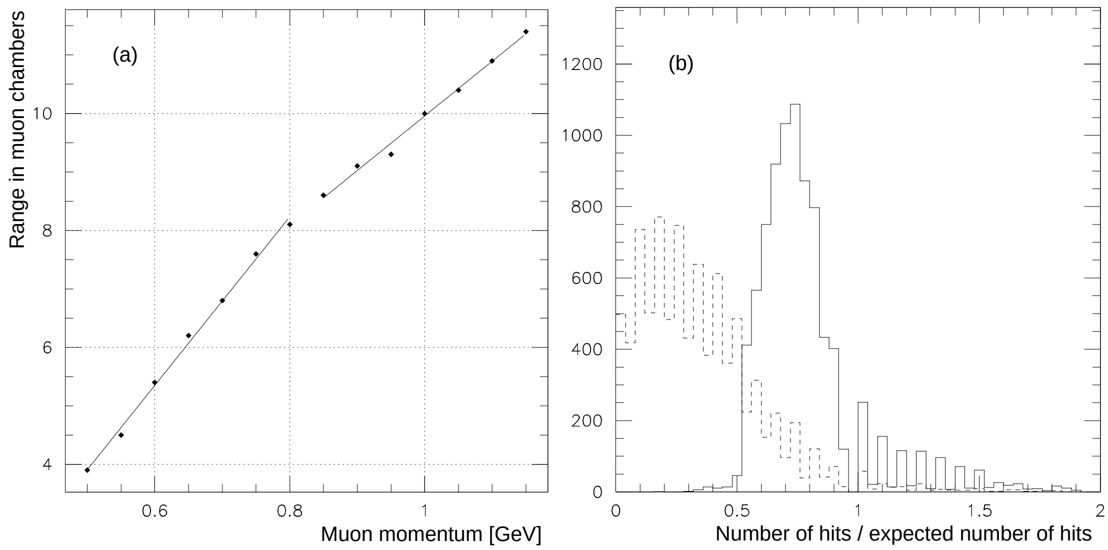

Figure 3.20: a) Range of muons in muon chambers as a function of the muon momentum. The range is given in 'number of muon chambers reached'. b) Ratio of the number of hits found divided by the number of hits expected for muons (solid) and pions (dashed).

3.10 Data acquisition and trigger

3.10.1 Overview

The total rate through the detector outside the beam region is about 50 MHz. The size of a typical event is 1-2 kBytes. A conventional tape drive records up to roughly 500 kBytes/s. Hence not more than a few hundred events per second can be written to a single tape. A fast trigger with a very high rejection for background and an almost perfect efficiency for physics events becomes crucial. As it is common nowadays, E865 uses a multilevel trigger outlined in Figure 3.21. The real situation is somewhat more complicated and will be discussed in the next two sections.

3.10.2 The trigger

The general design philosophy of the trigger is to use a multilevel structure which eliminated the largest fraction of events as early as possible with simple and fast hardware requirements. More sophisticated, and hence slower requirements are implemented in successive levels. The sensitivity of the experiment is limited by this ability to suppress background since a higher beam intensity always implies a much larger background rate

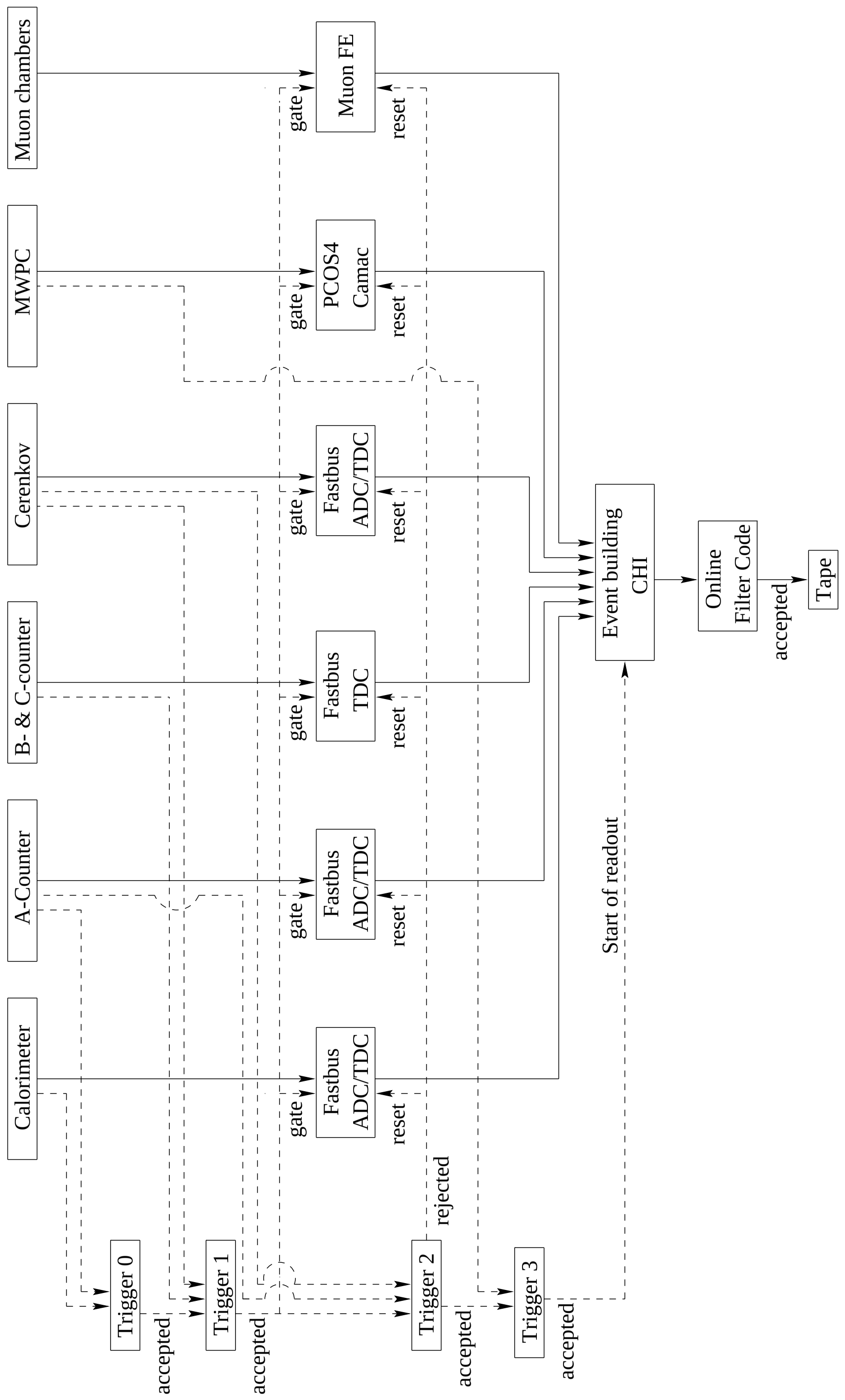

Figure 3.21: Data acquisition and trigger system. Solid lines show the flow of data, dashed lines indicate the trigger logic.

associated mainly with random coincidences of tracks in the detector and only to a small part with more kaon decays.

Three different types of events are selected by the triggers and written to tape.

1. TAU trigger, sensitive to a three charge track final state, dominated by $K^+ \to \pi^+\pi^+\pi^-$ (K_τ)

2. ELER trigger (electron on the left and electron on the right), sensitive to $K^+ \to \pi^+e^+e^-$ $(K_{\pi ee})$, $K^+ \to \pi^+\pi^0$ with $\pi^0 \to e^+e^-$ and $K^+ \to \pi^+\pi^0$ with $\pi^0 \to e^+e^-\gamma$ (K_{DAL})

3. MUE trigger (muon and electron), sensitive to $K^+ \to \pi^+\mu^+e^-$ $(K_{\pi\mu e})$

The TAU trigger accepts events which are well suited to monitor the detector (e.g. MWPC efficiency and charged track trigger efficiency) and which are important for the test of the offline software. Only minimal requirements are imposed on this trigger and the K_τ decay, the dominating contribution to the TAU trigger, is the most common kaon decay mode with three charged daughter particles.

Events accepted by the ELER trigger allow for a measurement of the branching ratio and the form factor of the decay $K^+ \to \pi^+e^+e^-$, which provides an important test for the chiral perturbation theory. This decay as well as the decay $\pi^0 \to e^+e^-$ will be the subject of other theses. More interesting for us here is the K_{DAL} decay. It is used to monitor the Čerenkov counters and the calorimeter, and to normalize $K_{\pi\mu e}$.

A trigger sensitive to $K^+ \to \pi^+\mu^+\mu^-$ is also implemented, but the high trigger rate due to muons originating from the beam allowed us to take data only with a reduced beam rate. A cosmic trigger is also installed and used for the calibration of the calorimeter. All triggers could be enabled or disabled manually.

We will now consider the individual trigger levels in detail:

T0 trigger level:

This lowest trigger level is common for all trigger types. It is designed to indicate the presence of three charged particle tracks and it is formed from three coincidences between the A-counter and the corresponding modules in the shower calorimeter directly behind it. Since the attenuation length of photons in the A-counter is large compared to the thickness of the counter, only a few photons give a signal in the A-counter and therefore the T0 trigger level is sensitive almost exclusively to charged particles. The T0 trigger logic is shown in Fig. 3.22.

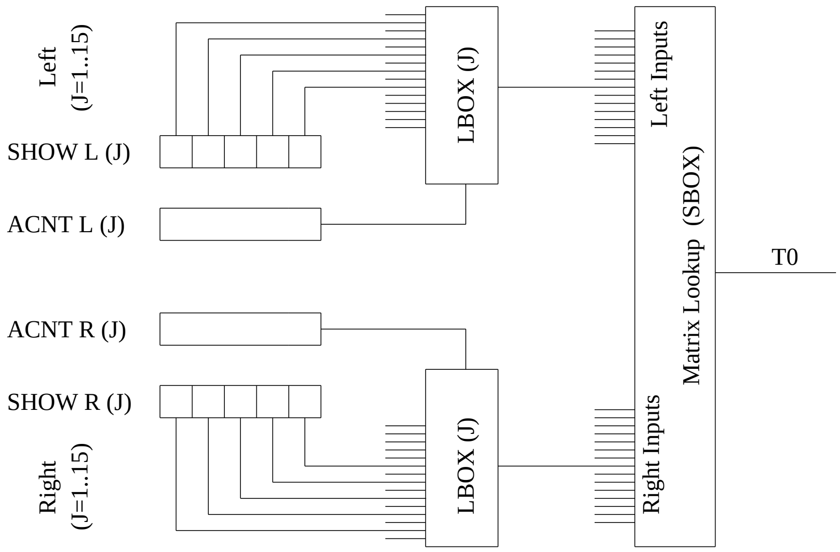

Figure 3.22: Logic of T0 trigger level (see text for description).

The signals from one A-counter slab (ACNT in Fig. 3.22) and the 15 calorimeter modules (SHOW) shadowed by this slab are the inputs to a custom-built unit (LBOX), mounted close to the detector. This unit forms coincidences between the 5 ns wide A-counter signal and the 20 ns wide calorimeter signal (A•SH, where • refers to a logical AND). Then, it corrects the timing of the A-counter signal, since light of particles hitting the A-counter in the middle of the experiment is collected later than light from particles hitting a slab close to its PM-tube. This is done by delaying the A-counter signal by $i \times 0.7$ ns, where i is the calorimeter module number, starting to count in the middle of the experiment. The output of all the 15 A•SH coincidences are then ORed together to yield the time adjusted output signal of LBOX. A third task of LBOX is to delay the calorimeter signal for the TDC readout. Another output, also a time adjusted A•SH signal, goes to a unit called SwissMix, which is used in the muon trigger.

The next step is to look for a coincidence between three LBOX signals, indicating three charged tracks. This is done in another custom-built unit (SBOX). The outputs of all 30 LBOX units are fed into a single SBOX unit. The SBOX requires two constraints to be met for a T0 signal: firstly, three LBOX signals have to be in-time and second, the pattern of the hits belonging to the three signals has to be physical. Physical hit patterns are defined by Monte Carlo generated $K_{\pi\mu e}$ events and stored in a look up table. The T0 signal is available 172 ns after the particles crossed the A-counter. We run typically at a rate of 2 millions T0 triggers per spill.

There are three different types of events, which we lose at the T0 trigger trigger level. First, events are lost when two tracks hit the same A-counter slab. The second sample that gets rejected consists of events where a track with a large slope in Y (Θ_Y) does not hit the A-counter and the calorimeter in the same row. Finally a small number of events are discarded when one track crosses between the A-counter and the calorimeter from the left to the right side or vice versa. Originally we intended to require for the T0 signal a coincidence between the A-counter with the shower counter row directly behind it, or with the shower counter one row above for tracks in the upper half or one row below for tracks in the lower half. But since this would cause an unjustifiable increase in the accidental rate, now only the row just behind the A-counter is allowed.

T1 trigger level:

At this trigger level the three trigger types are split. It is designed to indicate the presence of electrons and muons in the apparatus as shown in Fig 3.23.

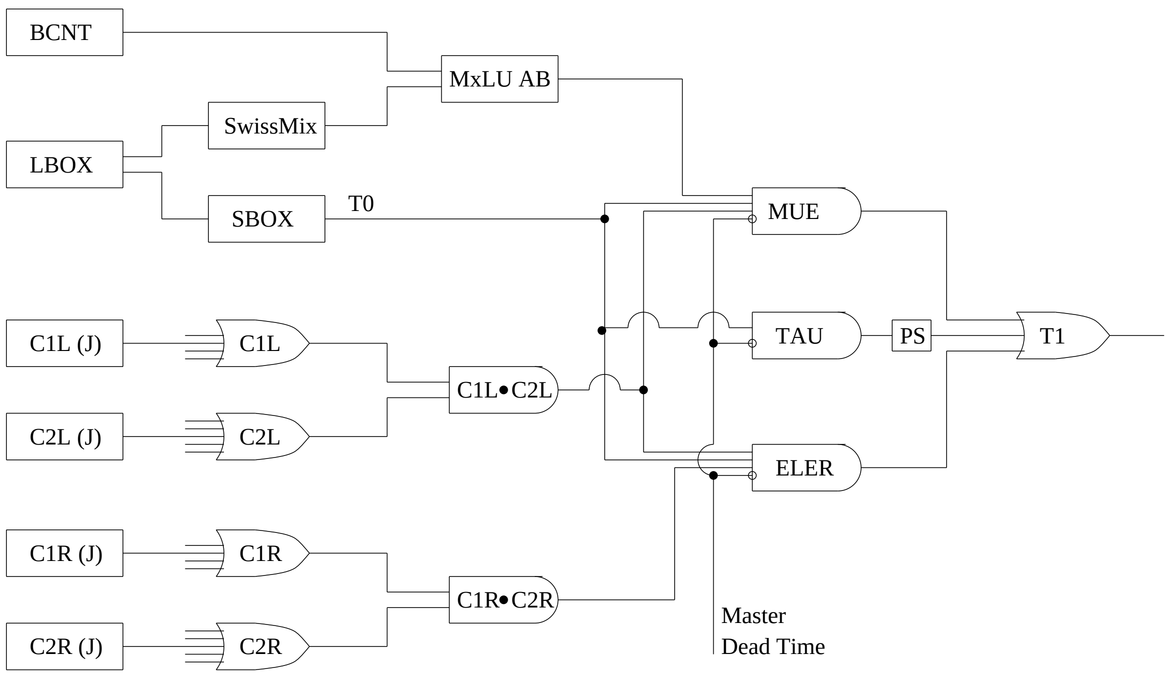

Figure 3.23: Logic of T1 trigger level. The index J runs over the PMT's on either side of the counters C1 and C2 (see text for description).

The electron condition is implemented by requiring at least one photomultiplier signal above a 0.25 photoelectron threshold in the left side of C1 in coincidence (∼13 ns) with a signal above threshold in the left side of C2, denoted C1L•C2L. A similar requirement on the right side of the Čerenkov counters, C1R•C2R, indicates the presence of a positron. A muon is defined as an appropriate coincidence between the SwissMix signal and the B-counter signal. The SwissMix maps the outputs of LBOX into the horizontal positions of the hits. The pattern of hits in the B-counter is checked against the outputs of the SwissMix in a fast matrix look-up unit (MxLU AB), similar to SBOX mentioned above. The look-up table is based on muons from generated $K_{\pi\mu e}$ decays.

For a MUE trigger a coincidence between an electron on the left side, a muon, a T0 signal and a logical NOT of the master dead time signal (MDT) is required. An electron on the left, a positron on the right, a T0 signal and a NOT of the MDT gives an ELER trigger. No particle identification is required for a TAU trigger in order to keep it unbiased. It is a coincidence between a T0 and a NOT of the MDT. But the TAU trigger was prescaled (PS) by a factor $20,000$ at the beginning of the 95 run and by $30,000$ at the end of the run, because otherwise this trigger would have swamped the data acquisition. The MDT does not allow events to enter the DAQ before a previous event is safely buffered or rejected by a higher trigger level.

An obvious addition to the MUE trigger would be to require a veto of the right side of the Čerenkov counters. However, there are two conflicting requirements. If we just veto with the AND of the right sides of the two counters (CRAND), almost 10% of the events would be accidentally vetoed. The rate in CRAND can be reduced by raising the threshold, but this also reduces the efficiency to a level where not enough rejection for e^+ is left to make it worthwhile.

T1 is a very powerful trigger level, it reduces the rate to 2000 triggers per spill, and it is also very fast, the T1 signal is available 307 ns after the particles crossed the A-counter. This makes it well suited to provide the gate for the wire chambers, the ADCs and the TDCs.

T2 trigger level:

This trigger level further insures the presence of an electron in MUE and the presence of a positron and an electron in ELER. TAU triggers are bypassed. T1 does not constrain the position where the particle crosses the two Čerenkov counters. It only requires an OR of all photomultipliers in one half of the counters. Since light, reflected by a certain primary mirror, is collected mainly by only one PMT, it is possible to divide each half of C1 into an upper and a lower quadrant, and each half of C2 into four, horizontally equally divided parts. An electron can now be defined as an appropriate coincidence between the different parts in the Čerenkov counters with a corresponding A-counter slab, validated by a calorimeter signal. To form this coincidence a horizontal arrangement for the A-counters was chosen.

A further classification of ELER events is made at this trigger level. Up to now, the ELER trigger is dominated by K_{DAL} events, a useful, but not very interesting decay mode. A kinematical feature of this decay is now used to suppress K_{DAL} events in favour of decays of greater interest like $K_{\pi ee}$. Since K_{DAL} is mediated by a virtual photon decaying into an e^+e^- pair, the decay transition probability is proportional to $1/q^2$, where $q^2 = (P_+ + P_-)^2$ and $P_{+(-)}$ is the four momentum of the positron (electron). This favours events with low q^2 highly. For the $K_{\pi ee}$ transition, on the other hand, the q^2 spectrum ranges from a lower limit of $2m_e^2$ to an upper limit of $(m_K - m_\pi)^2$. Because of their very low q^2, an e^+e^- pair from the K_{DAL} decay tends to follow parallel trajectories in the vertical plane, while pairs from $K_{\pi ee}$ will very often have large opening angles. This feature allows the following classification:

1. High mass events have a horizontal separation between the e^+ and the e^- larger than two A-counter slabs. They are latched by the T2 trigger level.
2. Low mass events have an e^+e^- pair within ± 1 A-counter slabs, the event is most likely a K_{DAL}.

ELER events are prescaled by a factor of 10 unless they contain a high mass (or a MUE or a TAU) latch. In this case, the event passes regardless of the prescale level. Typically about 1300 events per spill survive the T2 trigger level. It is available after 535 ns.

T3 trigger level:

This stage, identical for all trigger types, makes use of the OR from the LeCroy 2748 MWPC readout controller available from each half of each wire plane, a so called logical plane. It requires that three out of the four planes on the left side of P1 and also three out of four planes on the right side of P1 have at least one hit, indicating at least two tracks and hence a kaon decay upstream of P1. A further condition, which rejected mainly events with too many hits uses a likelihood function of the ORs implemented in hardware. It counts the number of cards containing data for each logical plane. These numbers are then compared to a probability distribution for the number of hits expected in a given logical chamber as determined from K_τ decays, i.e. a likelihood of these numbers is formed and a maximum cut is applied. This isolates events with a large number of tracks, which are difficult and time consuming to reconstruct. This final trigger level mainly cleaned up the TAU trigger, which relied up to now only on three A•SH signals, rejecting about 50% of the TAUs. T3 passed typically about 1000 events per spill to the data acquisition system and is available after 20 μs.

3.10.3 Data acquisition system

The data acquisition system (DAQ) is based on the system of the MEGA experiment at the Los Alamos National Laboratory [67]. It consists of Camac-, Fastbus- and VME-modules, two Digital 3000/600 Alpha Workstations and a Micro Vax as shown in Figure 3.24.

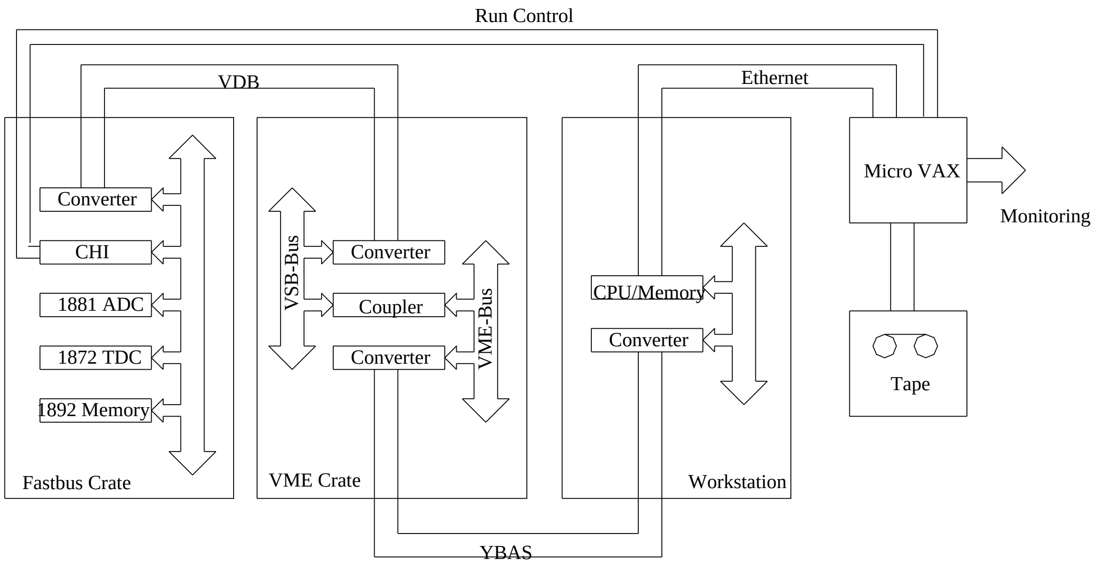

Figure 3.24: Hardware levels and bus system of the data acquisition system.

The front end electronics of the individual detector elements is described in the previous sections. We will now describe the further processing of the data. The signals, if in-time with a T1 trigger signal, from up to 16 PCOS4 MWPC read out cards are connected together in a stream (section 3.5.3) and transfered at 20 MHz to a LeCroy 2748 Camac controller. Four streams are read out in parallel by a single controller, hence it takes about 16 μs to read out 1024 wires. The 9 bit data word from each MDL108 chip is checked for parity and wires hit. If any wires are hit, the 8 bit data word and a 7 bit chip address are combined in a data block and read out using a Camac Smart Crate Controller (SCC) [68]. The SCC routes the data to a high speed parallel port, which is connected to a LeCroy 1892 Fastbus memory module with 4 MByte of memory.

The outputs from the muon chambers are transfered in parallel through long delay lines ($\sim$410 ns) to 12 Fastbus sized crates, equipped with amp/latch cards designed at Yale and Brookhaven. The signals are amplified, discriminated and, if in coincidence with a T1 trigger signal, latched and transfered serially to a Yale designed data buffer in Camac. Finally, they are sent via a SCC into a 1892 memory module.

The signals from the calorimeter, the Čerenkov counters and the hodoscopes are split, with half the signal going to NIM discriminators to be used in the trigger logic decisions described in the previous section. The discriminated signals are also sent to LeCroy 1872 Fastbus time to digital converters (TDC) and digitized, provided that a gate, sent by the T1 trigger level, is present. The other half of the signal goes to LeCroy 1881 Fastbus analog to digital converters (ADC) which integrate and digitize the charge in the signal, if a T1 signal is present. The ADC's and TDC's can store up to eight events. Only the signals from the Čerenkov counters, the calorimeter and the A-counter are fed to the ADC's. However, timing signals are available for all detectors.

The latched information from the trigger and various scaler signals, e.g. trigger rates, beam monitors (section 3.3), rates in Čerenkov photomultiplier tubes, etc. are also collected in Camac and sent via a SCC to a 1892 memory module.

The ten ADC, ten TDC and three memory modules are installed in two Fastbus crates connected by a Struck STR410 cluster interconnect, providing a common bus for the two crates. The number of events stored in the ADC's and TDC's are controlled by a custom built NIM module, the so called 'up-down' counter. Each incoming event, i.e. a T3 trigger signal, increments the counter by one, each outgoing event decrements it. After an event is buffered in the Fastbus modules, it also resets the MDT, provided the up-down counter has not reached the value 7. If it has, it will not issue a reset. The central piece of the DAQ is a Struck STR330/CPU called CHI (CERN host interface) a fast frontend processor. It contains a Motorola MC68030 chip running at 16 MHz with 1 MByte RAM and 4 Mbyte data buffer. After being activated by the up-down counter, it reads out all Fastbus modules, formats the event and stores all events until the end of an AGS spill in its data buffer. The readout of the Fastbus modules is done using a direct memory access (DMA) block transfer. No CPU is used for this transfer, and between 5 and 8 μs are used to read out a single module. At the end of a spill the buffered data in the CHI are transfered to one of the two Alpha workstations. This transfer is an intricate matter. Each workstation accesses 4 MByte of the address range of the VME bus (shared memory), i.e. a workstations can be viewed from a 'logic' point as a block of addresses on the VME bus as they are directly plugged into the VME crate. A specified byte in this address range defines the status (free or busy) of the workstations. The CHI has DMA access on the address range of the VME bus and thereby completes the connection. The connection consists of the following hardware parts: A first module sitting next to the CHI converts the local signal to a differential (VDB) signal. A short cable makes a connection to a VDB/VSB converter, sitting in the VME crate. The VSB signals are routed into a coupler, which transfers the signals into the VME protocol. A final connection exists between the VME crate and the workstations, requiring two additional converters and a YBAS bus. A maximal transfer rate of 3.27 MBytes/s for the connection between the CHI and a workstation was measured [66].

The workstations are DEC 3000/600 Alphas. Their 64-bit architecture together with the Digital UNIX (OSF V1.3.) operating system provides a high performance. The processing speed is 175 MHz. The online software trigger (filter code) running on this system rejects about 40% of the data and will be described in chapter 4.2. Remaining events are passed to a MicroVax 3100 and written to tape. The MicroVax is also used for the run control, i.e. starting, stopping, suspending or resuming a run. The transfer rate between the workstations and the tape is calculated to be 280 kBytes/s [66]. Comparing this number with the maximal taping rate of 340 kBytes/s, we recognize that the system runs close to the maximal possible rate. This means that the filter code allows to increase the data taking rate by almost 40%.

To monitor the performance of the detector, a small fraction of the events are sent from the MicroVax to a second MicroVax where they are analyzed. A set of histograms e.g. hit distributions in the detectors and a display showing the variation of different variables over time, coupled with an alarm if the variable falls below or increases above a threshold, are made available for fast online checks. This is very useful in detecting malfunctions in detector or trigger components. Additional online monitoring routines can be started, e.g. an event display or a dump of the raw data. These are used for a fast check at the beginning of a run or to track a problem down to its source.

Chapter 4

Signal search

4.1 Introduction

The main goal of the analysis is to establish an upper limit on the $K_{\pi\mu e}$ branching ratio, assuming no signal events are found. In general, the branching ratio (BR) is the total number of decays into the mode in question, divided by the total number of decays. Instead of counting the total number of decays, which is difficult, the BR is measured by comparing its frequency of occurrence with that of some other decay, the so called normalization channel, which can also be detected in the apparatus and has a known BR. The formula to calculate the BR of a particle a into the final state b then takes the general form:

$$BR(a \to b) = BR(a \to c)\frac{N(a \to b)}{N(a \to c)} \tag{4.1}$$

$N(a \to b)$ and $N(a \to c)$ are the number of particles observed for the decays $a \to b$ and $a \to c$, respectively. Of course, for both processes, only a fraction of the decays are accepted by the detector The acceptance A is a function of the kinematics of the decay, the detector geometry and the efficiency of the trigger and data analysis. Then 4.1 takes the form:

$$BR(a \to b) = BR(a \to c)\frac{N(a \to b)}{N(a \to c)}\frac{A(a \to c)}{A(a \to b)}C \tag{4.2}$$

The factor C is introduced to account for any small systematic corrections to the calculated acceptance ratios. To keep this correction factor as simple as possible, we like to select a normalization channel which has many common properties with the signal channel.

The process K_{DAL} serves well as a normalization channel. Since its branching ratio times decay probability is relatively large, collecting a statistically significant data sample is not difficult. It also shares two of the three final state particles with $K_{\pi\mu e}$. This provides a significant advantage compared with K_{τ}, the other abundant decay mode, sharing only one final state particle.

In this chapter we outline the steps taken to reduce the $K_{\pi\mu e}$ data sample and to isolate the K_{DAL} normalization sample. The data reduction proceeds in steps with increasing level of complication and refinement as the data sample is filtered into ever smaller subsets.

4.2 Online analysis

The signal search begins at the trigger level. The trigger is designed to maximize the probability of finding a $K_{\pi\mu e}$ event while rejecting as much background as possible. The next step of the search is an online analysis (filter code) of the events accepted by the trigger which is essentially a simplified offline analysis. This analysis is performed on the two Alpha machines described in Chap. 3.10.3. It is a 'real time task', and therefore limited by the time available per event. Care has also to be taken in setting the cuts, since events rejected by the online analysis are lost forever. Consequently, more emphasis is put on an efficient code, i.e. a code which rejects only a few 'good' events, than on a high rejection factor. As a final point, the code has also to be reliable, since errors like division by zero or access violation will either cause a crash of the whole DAQ system or, even worse, it will continue to reject events with a corrupted data buffer. The code is written in FORTRAN 77 with a few routines in C.

The filter code proceeds in a fashion to identify and reject non-signal events as quickly as possible. The simplest and fastest subroutines are called first, with increasingly complex algorithms applied as the analysis proceeds.

The data of a whole spill, about 1000 events, are stored on the Alpha's memory. Each event is then loaded into the analysis program's data buffer (DBUFF) in a two byte integer array, and checked for proper data format. This essentially involves checking the lengths of different fixed blocks, e.g. number of scalers or latches, and checking for the correct presence of all MWPC and muon chamber planes, and also of the TDC and ADC modules. Events failed this check very rarely as such a failure indicates a severe corruption of the data, most often caused by a hardware malfunction. These events are sent immediately to the MicroVax and from there to the monitoring system allowing a fast detection of such failures.

Events with a correct data format are subject of the following checks:

Check of the T0 trigger:

We first verify the presence of three coincidences, called clumps, between the A-counter and the calorimeter. The algorithm starts to look for an A-counter slab with a deviation from the expected timing of less than 10 ns after pedestal subtraction. If a hit is found, the calorimeter modules shadowed by the A-counter slab are scanned for a module with a deposited energy exceeding 75 MeV and an absolute timing within a 10 ns window, again after pedestal subtraction. At success, a 'clump' is built, consisting of the 3×3 modules surrounding the module found above, i.e. all the energy deposited in the nine modules is added together and a position and a timing is calculated, both weighted with the stored energy in the individual modules of the clump. Multiple clumps per A-counter slab are allowed. Figure 4.1 shows the time distributions of accepted and raw events. Figures 4.2 and 4.3 show the deposited energy of pions, muons and electrons in the calorimeter. The position of the cuts used is indicated in the figures, where the arrow points towards the part which is tossed away. The rejection factors are listed in Table 4.1.

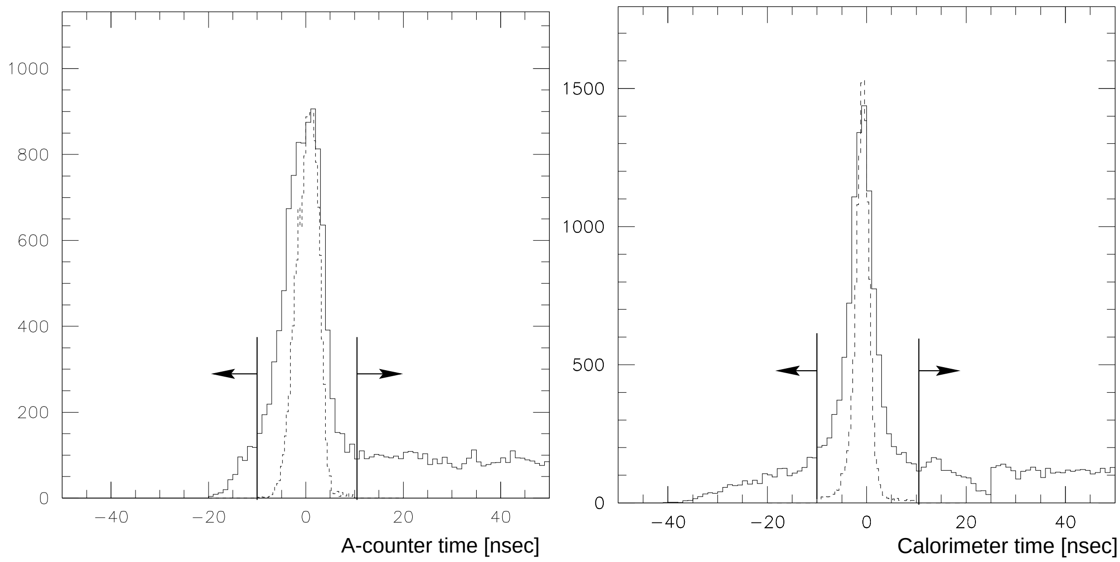

Figure 4.1: Timing of the A-counter and of the calorimeter for all hits (solid) and hits used in K_τ data (dashed). Additional timing corrections will be applied later in the analysis.

Check of Čerenkovs:

Almost 20% of the MUE and ELER events are triggered by scintillation light, delta rays or other accidental incidents in the Čerenkov counters. This algorithm identifies electrons and positrons by searching for light within a ± 10 ns wide time window in both Čerenkov counters that can be assigned to a clump with at least 0.6 GeV deposited energy. Only HIMS (high mass ELER) and PME (MUE with chamber validation) events are subjected to this test. EEPS (prescaled ELER) events are not checked because this sample is used to calculate the efficiency of the Čerenkov counters. The number of EEPS events is kept at a reasonable level by adjusting the prescale level. This can be done without losing any important information.

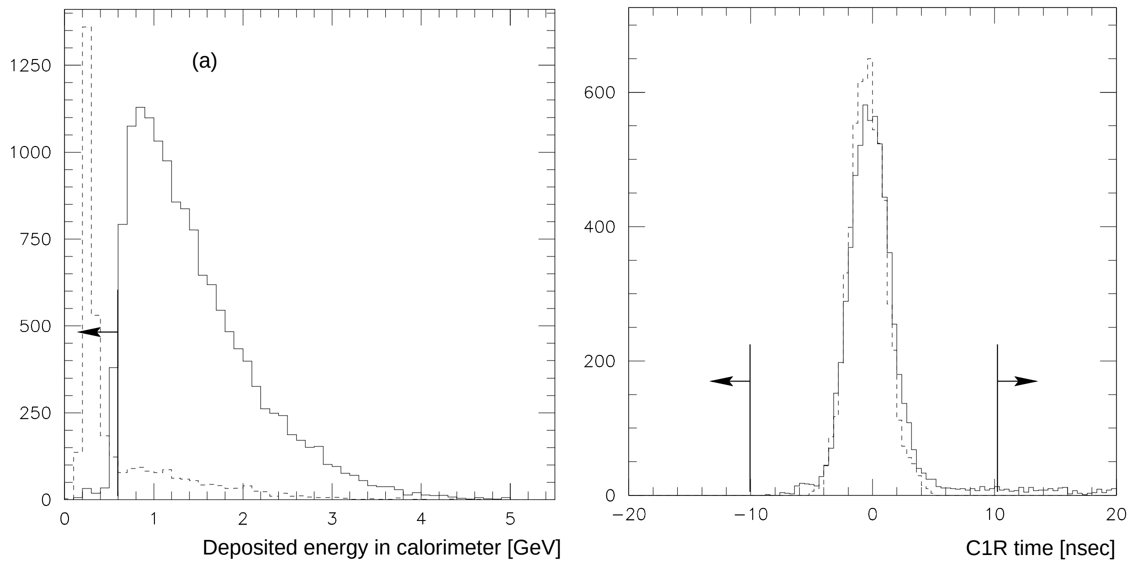

Figure 4.2: a) Deposited energy of electrons and positrons from Dalitz events in the calorimeter (solid). Also shown is the deposited energy for pions (dashed). b) Timing of the right side of C1 for all events with an ELER trigger latch (solid) and identified e^- in Dalitz events (dashed). The timing of C1 left and C2 is not significantly different.

As mentioned in chapter 3.10.2 no veto of the right side Čerenkov counters is used in the PME trigger. This routine now rejects in addition events with a positron track, where the positron is identified by a clump of at least 0.6 GeV and corresponding Čerenkov light in both counters within a ± 5 ns wide time window and an amplitude of at least 2.5 photo electrons (see Fig 3.14).

Presence of a muon:

Muon identification is based up to now only on a coincidence between an A•SH and a hit in the B-counter, no information from the muon chambers is used in the trigger. This last filter code routine checks the presence of a muon by first requiring a clump with an energy less than 0.45 GeV, an absolute B-counter timing better than ± 10 ns and a difference in X between an accepted clump and an accepted B-counter hit of less than 40 cm, where the position of the clump gets scaled by a factor 1.1 to take into account the slightly different B-fields in D5 and D6. Figure 4.3 displays these cuts. Then the algorithm scans the muon chambers in a limited region between the clump and the B-counter hit for a 'reasonable' hit pattern. This is done by combining the hits of 8 wires into cells, corresponding to the OR of the 8 wires, for the X- and Y-planes of the first 8 muon chambers. Monte Carlo simulations show that only a certain range for the slope is allowed, a real muon track can not cross more than three cells. Additionally, a track has to be straight, within certain limits given by multiple scattering. These two constraints limit the search to 58 possible patterns of the cells. Tracks agreeing in five of the maximum possible 8 cells with one of these patterns are accepted. In addition, an unlimited number of background hits can be present.

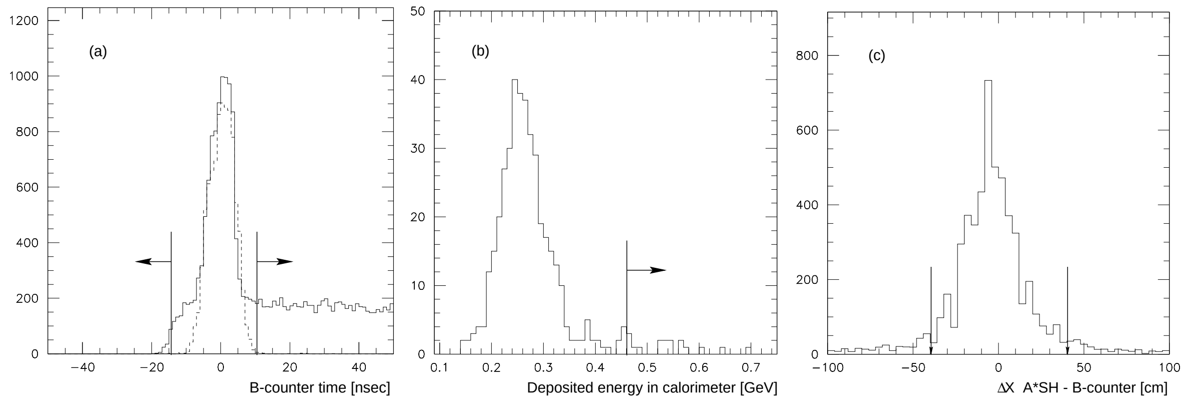

Figure 4.3: a) Timing of the B-counter for all hits (solid) and hits from beam muons (dashed). b) Deposited energy in the calorimeter from muons originating from a K_τ decay followed by a $\pi \to \mu\nu$ decay. c) Horizontal distance between the positions of the hit in the calorimeter and the position of the hit in the B-counter. Simulated $K_{\pi\mu e}$ events are used to generate this figure.

Inspecting Table 4.1, which summarizes the rejection factors, it may seem odd that fewer events get accepted if all three trigger types are examined together than if only one individual type is considered. The reason is that about 20% of the events have an ELER and a MUE trigger latch and hence bypass all tests not intended for one of the trigger

	Accepted	Rejection T0	Rejection Čerenkov	Rejection muon
MUE	63%	10%	22%	15%
ELER	69%	10%	27%	0%
TAU	63%	20%	0%	0%
MUE∘ELER∘TAU	61%	11%	25%	11%
MUE•$\overline{\text{ELER}}$	54%	10%	25%	22%
ELER•$\overline{\text{MUE}}$	53%	11%	44%	0%

Table 4.1: Rejection factors of the three filter code routines. All numbers refer to the whole sample of events. The numbers sum up to more than 100% since a few events fail more than one test. ∘ stands for a logical OR and • for a logical AND.

types. Examining triggers with only a single trigger latch, only slightly more than 50% of the events get accepted.

No high level kinematical variables are used in the filter code. A decoding of the chamber information is necessary to have access to such information. The algorithm to reconstruct tracks is very CPU time consuming, due to a large number of combinations, as we will see in the next section. It is not possible to reconstruct the kinematics of an event within the available amount of time.

The code ran in this configuration for the last few weeks of the run in 1995. During the first part of the run, there was no online analysis.

4.3 Data analysis

Before we continue with the discussion of the data rejection, we outline the logical flow of the E865 data analysis, since it is identical for all the following analysis stages.

The reconstruction of an event can be divided into two parts. The first task involves the search for charged tracks in the spectrometer and the fitting of momenta and of decay vertices. This is then followed by an examination of the response of the particle identification system.

4.3.1 Clump finding algorithm

This routine, designed to look for coincidences between the A-counter and the calorimeter, provides kinematical and also particle identification information. The algorithm is identical to the one used in the online analysis and is described above. Its main outputs are the deposited energy, the timing and the position of a charged particle striking the calorimeter. Additionally, the routine is used to identify photons as isolated electromagnetic shower clusters with no A-counter fired in front.

4.3.2 Space point building

In order to find tracks in the spectrometer, the raw wire hits in the four planes of a MWPC have to be combined into space points, i.e. positions have to be found, where the wires from different planes overlap. Since a single wire plane typically gets about 10 hits per event, a simple looping over all hits would produce a huge number of combinations and require an immense amount of computer time. A simple way to reduce the number of combinations is to narrow the region where the algorithm has to look for space points. We know from the clump finding the position where a particle presumably struck the calorimeter. For any given clump, only a limited window in space is kinematically allowed in each MWPC. The size of the window is tuned on data K_{DAL} and K_τ events taken at a very low beam intensity. The algorithm selects clusters of up to three continuous wires crossing at least one window. Only these clusters are used to find space points, all other wire hits are discarded. This procedure greatly reduces the number of clusters available to the space point finding algorithm.

The algorithm proceeds to find space points where wires from all four wire planes overlap ('quadruplets'). Let the angles between the V (or U) coordinate axis and the X-axis be $\pm\Theta$:

$$\begin{pmatrix} V \\ U \end{pmatrix} = \begin{pmatrix} \cos\Theta & \sin\Theta \\ \cos\Theta & -\sin\Theta \end{pmatrix} \begin{pmatrix} X \\ Y \end{pmatrix} \tag{4.3}$$

To find a quadruplet, a χ^2 can be defined as:

$$\begin{aligned} \sigma^2\chi^2 = (X - X0)^2 + (V - X0\cos\Theta - Y0\sin\Theta)^2 + \\ (U - X0\cos\Theta + Y0\sin\Theta)^2 + (Y - Y0)^2 \end{aligned} \tag{4.4}$$

where X, V, U and Y are the measured cluster coordinates, while $X0$ and $Y0$ are the space point coordinates. The method of χ^2 states, that the best values for $X0$ and $Y0$ are those, for which equation 4.4 is a minimum. Thus solving $\frac{\partial\chi^2}{\partial X0} = 0$ and $\frac{\partial\chi^2}{\partial Y0} = 0$ we get:

$$X0 = \frac{X + (V + U)\cos\Theta}{1 + 2\cos^2\Theta} \tag{4.5}$$

$$Y0 = \frac{Y + (V - U)\sin\Theta}{1 + 2\sin^2\Theta} \tag{4.6}$$

Substituting 4.5 and 4.6 into 4.4 leads to:

$$\sigma^2\chi^2 = \frac{2\cos^2\Theta}{1+2\cos^2\Theta}\Delta X^2 + \frac{2\sin^2\Theta}{1+2\sin^2\Theta}\Delta Y^2 \tag{4.7}$$

where

$$\Delta X = X - \frac{V+U}{2\cos\Theta} \tag{4.8}$$

$$\Delta Y = Y - \frac{V-U}{2\sin\Theta} \tag{4.9}$$

Once this is known, the hypothesis that the four clusters giving the position $(X0, Y0)$ form a space point can be tested by requiring:

$$\sigma^2\chi^2 < 2 \times PNTCUT \tag{4.10}$$

Only combinations of clusters with a $\sigma^2\chi^2$ less than a cutoff of $2\times PNTCUT$ are accepted as a space point, where the cutoff is set after study of real events. The algorithm loops over all clusters until all possible quadruplets are found. Then it continues to find triplets, i.e. points where the wires of only three wire plains overlap, by constructing a similar χ^2, e.g. for a triplet with a missing U-plane:

$$\sigma^2\chi^2 = (X - X0)^2 + (V - X0\cos\Theta - Y0\sin\Theta)^2 + (Y - Y0)^2 < PNTCUT \tag{4.11}$$

A cluster is allowed to be in more than one space point, but not more than two clusters in one space point can be the clusters that are already used in other space points. In this case, the space point with the better χ^2 gets accepted, but quadruplets are always accepted before triplets.

By requiring only three out of four possible planes, we insure that events are not lost due to chamber inefficiencies. The probability P of observing a space point is:

$$P = \prod_{i=1}^{4} \epsilon_i + \sum_{ijkl} \epsilon_i\epsilon_j\epsilon_k(1-\epsilon_l) \tag{4.12}$$

where the first term is the probability of obtaining a quadruplet and the second the probability of finding a triplet. The ϵ's are the efficiencies of the individual wire planes. We find that a wire plane is on average 90% efficient, giving a quadruplet probability of 66% and a triplet probability of 29%, and the combined probability is 95%.

Additionally, formulas 4.5 and 4.6 allow to calculate the resolution of a MWPC. Using the conventional single plane resolution of the wire spacing (2 mm) divided by $\sqrt{12}$, the resolution in X becomes 0.4 mm and in Y 0.6 mm.

4.3.3 Track finding

The task of the track finding is to group space points from different chambers into tracks. We know, that tracks form straight lines outside the spectrometer magnets, that they only bend in the X-direction in the magnet D6 (this is not strictly true due to the non-ideal field shape, but it is a good enough approximation to find tracks) and that the line from one side of D6 should intersect the one coming from the other side at the middle of the magnet. Thus, we can use the following three items to judge if a set of space points lies on a track:

1. Difference in the projected X-position between the upstream and the downstream part at the center of D6.
2. Difference in the projected Y-position at the center of D6.
3. Difference in the slope in Y between the two parts.

Since the slope and the projection in Y are not independent, we can not just write down the χ^2, but we can postulate that it is bilinear:

$$\chi^2 = P_i E_{ij} P_j \tag{4.13}$$

where P_i refers to one of the differences mentioned above and E_{ij} is the inverse of the covariance matrix.

We can write for the track:

$$\vec{x}(z) = \vec{m_j}(z - z_m) + \vec{b_j} \tag{4.14}$$

where we set $j = 1$ for the upstream part and $j = 3$ for the downstream part of the track. $\vec{m_j}$ is the slope and $\vec{b_j}$ the position at z_m, the center of D6. Thus:

$$\chi^2 = \frac{(b_{1x} - b_{3x})^2}{\sigma^2_{b_x}} + \frac{(b_{1y} - b_{3y})^2}{\sigma^2_{b_y}} + \frac{(m_{1y} - y_{3y})^2}{\sigma^2_{m_y}} + \frac{2(b_{1y} - b_{3y})(m_{1y} - y_{3y})}{\sigma^2_{b_y m_y}} \tag{4.15}$$

where the σ's are calculated from the covariance matrix.

The algorithm searches in the windows projected by a clump in the calorimeter on the MWPC's through all combinations of the space points. To be accepted as a track the X- and the Y-part of the χ^2 have to be below a cutoff that is set after a study of real tracks at low beam intensity in the detector. A set of cuts on the slopes is also applied to reduce the contribution from fake tracks made up of random hits, and the track has to point towards a limited region around the center of the clump. More than one track can be assigned to each clump and a space point can also be in more than one track.

After all tracks with space points in all four chambers (four-chamber-tracks) are found, the algorithm continues to search for tracks with one missing chamber (three-chamber-tracks). The track hypothesis for three-chamber-tracks is tested by calculating a χ^2 based on the difference of the Y-position of the space point in the middle chamber to the Y-position obtained by interpolating the space points in the first and in the last chamber. The slope and the assignment to a clump are tested as for four-chamber-tracks.

Considering that within the windows projected from a clump onto the MWPC's on average about 5 space points are found, more than one track per clump might be reconstructed. In a first version of the offline analysis, used for Pass1 and Pass2 described in the sections 4.4 and 4.5, the track with the best χ^2 was kept, all additional tracks are discarded. In a second version of the analysis, used for Pass3 (section 4.5), multiple tracks are kept, the selection of the 'best' track is part of the vertex fitting described in section 4.3.5.

Making use of the redundancy a formula similar to 4.12 is valid for calculating the probability of finding a track, where the efficiency of the single wire planes have to be replaced by the probability to detect a space point. The space point probability of 95%, as calculated above, yields a total track detecting probability of 98%.

4.3.4 Momentum fitting

The next step of the analysis consists of finding the particle momentum by fitting the curvature of found tracks to the magnetic field of the spectrometer magnets. The algorithm uses the individual clusters combined to a track in the space point and track finding, to fit the five parameters x, Θ_x, y, Θ_y and R needed to fully describe a track. The positions x and y and the slopes Θ_x and Θ_y are taken at the MWPC P1 and R is the the radius of curvature of the track in the spectrometer magnet D6 defined as the ratio of the charge to the magnitude of the momentum in the XZ-plane. Let $\overline{W}_i$ denote the measured clusters, σ_i the measurement errors (resolution of a single wire plane), α_k the five track parameters and $W_i(\alpha_k)$ the wire coordinates as a function of the parameters. Then, we can define a χ^2 as:

$$\chi^2 = \sum_{i=1}^{16} \frac{(W_i(\alpha_k) - \overline{W}_i)^2}{\sigma_i^2} \tag{4.16}$$

where the sum runs over the 16 wire planes. The goal of the algorithm is to minimize this χ^2 and to find the parameters α_k. Since the parameters are already very well known, a first order Taylor expansion of $W_i(\alpha_k)$ around the first guess α_{k0} is valid:

$$\chi^2 = \sum_{i=1}^{16} \frac{(W_i(\alpha_{k0}) - \sum_{k=1}^{5} \frac{\partial W_i(\alpha_{k0})}{\partial \alpha_k} \Delta\alpha_k - \overline{W}_i)^2}{\sigma_i^2} \tag{4.17}$$

The corrections $\Delta\alpha_k$ are then the adjustments to the guessed parameters α_{k0}, giving the best fit to the observed track hits $\overline{W}_i$.

At the minimum χ^2_{min} of the χ^2 we get the following system of linear equations:

$$\frac{\partial\chi^2_{min}}{\partial\alpha_i} = 2\sum_{j=1}^{16}\frac{(W_j(\alpha_{k0})-\overline{W}_j)}{\sigma_j^2}\frac{\partial W_j(\alpha_{k0})}{\partial\alpha_i} - \sum_{j=1}^{16}\frac{1}{\sigma_j^2}\frac{\partial W_j(\alpha_{k0})}{\partial\alpha_i}\sum_{k=1}^{5}\frac{\partial W_j(\alpha_{k0})}{\partial\alpha_k}\Delta\alpha_k = 0 \tag{4.18}$$

where only terms of first derivative in W are kept. Writing this in matrix form yields a simple expression for evaluating the corrections $\Delta\alpha_k$:

$$V_i = G_{ij}\Delta\alpha_j \Rightarrow \Delta\alpha_j = G^{-1}_{ij}V_i \tag{4.19}$$

Thus the problem is reduced to finding the first guess $W_j(\alpha_{k0})$, to numerically calculate $\partial W_j(\alpha_{k0})/\partial\alpha_i$ and to invert the matrix G_{ij}.

The most crucial part is clearly the formulation of W as a function of the first guess parameters α_{k0}. This involves tracking the particles from the first MWPC to the other MWPC's. Two sets of functions are used. The first one idealizes the spectrometer magnet as a perfect dipole ('hard-edge approximation'), i.e. only a single main field bend and entrance and exit edge focussing caused by a Lorentz force, if particles enter the fringe field of the magnet at an angle different from 90^0, are taken into account. The value of the field is adjusted to give the correct reconstructed mass to K_τ events. Although this approximation is not tremendously accurate, it is much faster than the second function, the so called 'stepper'. As mentioned in Chap. 3.4, the field of D5 and D6 is mapped on a grid in 5 cm steps. This algorithm 'steps' a track through the mapped field by first order numerical integration of the Lorentz force equations of motion:

$$\vec{P}|_{z+\delta z} = \vec{P}|_z + QC\delta z \begin{pmatrix} \Theta_y & B_z & - & & B_y \\ & B_x & - & \Theta_x & B_z \\ \Theta_x & B_y & - & \Theta_y & B_x \end{pmatrix} \tag{4.20}$$

where Q the charge of the particle and C=3×10^{-7}(GeV/c/Gauss/cm). The step size δz is usually chosen to be 5 cm. Results do not significantly change by using a shorter step size. The components of the B-field are given by linear interpolation from the nodes of the field map.

4.3.5 Vertex fitting

The next stage of the analysis is the propagation of the fitted tracks back through the magnetic field of D5 to a common vertex point. Since all K^+-decays of interest involve three charged particles, only vertices from three tracks are sought. Up to now, we have found three or more clumps with possible multiple tracks assigned to them. The task of vertex finding is the selection of three tracks originating from a common vertex and finding the coordinates of this vertex point. The algorithm propagates the fitted tracks at P1 back to the middle (in Z) of the decay volume. Then a vertex point is found for all possible combinations of three tracks, where no two tracks are allowed to originate from the same clump, by measuring the quantity s, which is the r.m.s. distance of closest approach of the tracks in X and Y to a common vertex point. The combination of three tracks having the lowest s value is assumed to have the highest probability to originate from a K^+-decay. The most crucial part of this algorithm is the backtracking through D5. Again, the same two methods used already for the track fitting are employed, i.e. the 'hard-edge approximation' and the stepwise integration of the trajectories.

The algorithm of vertex fitting (and track fitting) is very computer time intense, since at nominal beam intensity, we typically found 4-5 clumps with multiple tracks assigned to them, requiring a fitting for many different combinations. But we found that allowing multiple tracks per clump, up to 25% more K_τ events are found, compared to the analysis where only the track with the best χ^2 is sought. This makes this additional (computer) effort worthwhile. Unfortunately this was discovered only after the completion of the first two offline passes described in chapters 4.4 and 4.5. Thus only one track per clump was allowed for this analysis, while the third offline pass makes use of the full power of the improved analysis.

4.3.6 Particle identification

This section describes how the information provided by the detectors responsible for the particle identification is linked to the tracks found.

To assign light in the Čerenkov counters to a track selected in the vertex fitting, the track parameters from the momentum fitting procedure are used to predict in each Čerenkov counter the PMT(s) that would have collected Čerenkov light emitted by this track. The light detected by these PMT's is then added together and associated with the track where requirements on the TDC are imposed to discriminate against accidental light. These TDC requirements are not identical for all analysis passes and will be described later. Additionally, a signal time, weighted with the number of photoelectrons detected by the individual PMT's which contribute light, is calculated and assigned to the track.

As described above, clumps found in the electromagnetic calorimeter are the starting point to find tracks in the MWPC's. Hence it is straightforward to assign the deposited energy, timing and position of a clump (section 4.2) to a track. In addition, the ratio E/P of the energy E deposited in a clump consisting of 3×3 modules divided by the momentum

P of the track, as found in the fit, provides an excellent method to discriminate pions and muons from electrons.

The basic idea of how the muon stack is used to identify muons was outlined in section 3.9.2. However, the criteria for assigning hits to a muon track still needs to be defined. We collect hits in a cone along the track projected from MWPC's P3 and P4. The limits of the cone in the N-th chamber are defined by multiple scattering and the resolution of the chambers. We can define

$$\sigma_N = \frac{s}{\sqrt{12}} + \sum_{i=1}^{N} \Delta z_i \times \frac{0.014 \text{ GeV}}{E\beta} \sqrt{XR_i}(1 + \frac{\log XR_i}{9}) \tag{4.21}$$

where the first term is the resolution of the muon chamber ($s = 1.3$ cm is the wire spacing) and the second term gives the contribution from the multiple scattering [69]. Δz_i is the distance from the calorimeter to the ith muon chamber, XR_i is the number of radiation lengths in the ith muon chamber. Hits are required to be within $\pm 3\ \sigma_N$ from the track projected from P4 to the muon chamber N to be assigned to the muon trajectory. Additionally, a χ^2 is calculated for each trajectory.

The B-counter can be used in an analogous way for the muon identification. We calculate the horizontal distance b between an in-time hit in the B-counter and the projected track from P4 and compare to σ_B calculated using equation 4.21.

To summarize, in our apparatus we identify electrons as those particles giving light in the appropriate Čerenkov counters and having a pulse height in the calorimeter consistent with the momentum measured in the spectrometer. Muons are seen as particles giving no light in the Čerenkov counters, a minimum ionizing pulse height in the calorimeter and a range in the muon stack consistent with their momentum. Pions have no light in the Čerenkov counters, and a range in the muon detector shorter than that expected for muons.

All the necessary tools needed to search for a $K_{\pi\mu e}$ event are now described.

4.4 First offline analysis stage: Pass1

At the conclusion of the run, about 200 8 mm data tapes have been written, each containing about 3 million events of which about 70% are MUE triggers. The first off-line pass through the data serves two main purposes: First, it does a crude kinematical reconstruction of the events and rejects the events that do not reconstruct, and second, it separates the surviving data into four different output streams:

1. Tau: K_τ candidates with a TAU trigger latch, passing the kinematical reconstruction. About 5% of the surviving events are written to this stream.

2. Cosmics: Cosmic events for calibration of the calorimeter, with a cosmic trigger latch. These events are accepted by Pass1 without any requirements (about 15% of the data).

3. 5trk: Data with five tracks independent of the trigger latch, e.g. $K^+ \rightarrow \pi^+\pi^0$, followed by $\pi^0 \rightarrow e^+e^-e^+e^-$. This output stream is not a subject of this thesis and will not be considered any further. It comprises about 0.5% of the output data.

4. 3trk: Events with three tracks and a MUE or ELER trigger latch. This output stream involves all the 'interesting' physics events, as $K_{\pi\mu e}$ and K_{DAL} candidates and all the other rare decays of the K^+ not falling into one of the classes mentioned above. It is the largest output stream, about 80% of the events surviving Pass1 are written to it.

Identical cuts, summarized in table 4.2, are applied to 3trk and Tau events. The separation between these two output streams is based only on the trigger latch, no additional particle identification is made.

$N_{clump} \geq 3$	at least 3 clumps
$N_{trkinvtx} = 3$	three tracks in the vertex
s < 10	low vertex miss distance
2 pos + 1 neg	two positively and one negatively charged particles
$P < 8$	reconstructed kaon momentum less than 8 GeV.

Table 4.2: Summary of the Pass1 cuts applied to Tau and 3trk candidates.

The first cut, requiring three clumps, does not reject any data, the same cut was already employed in the offline analysis. It serves only as a consistency check. The main requirement for accepted events is that a three-track vertex with a vertex miss distance s less than 10 cm be found, using the hard-edge approximation for all track and vertex fitting. Additionally, the momentum of the kaon reconstructed from the three tracks joint in the vertex has to be below 8 GeV. No lower limit on the kaon momentum is imposed, since the K_{DAL} events are reconstructed without the photon. Figure 4.4 shows these kinematical distributions, fitted with the hard-edge approximation. Finally, Pass1 requires also that two tracks on the vertex can be assigned to positively charged particles, and one track to a negatively charged particle, where the charge of a particle is checked by examining the change of P_X/P_Z in D6, the change is positive for positively charged particles and negative for negatively charged particles.

Table 4.3 lists the rejection factors of the individual cuts for 3trk and Tau events. The large rejection factors obtained by requiring three tracks are quite conspicuous, especially for Tau events. A more detailed analysis of the rejected events shows that one third of

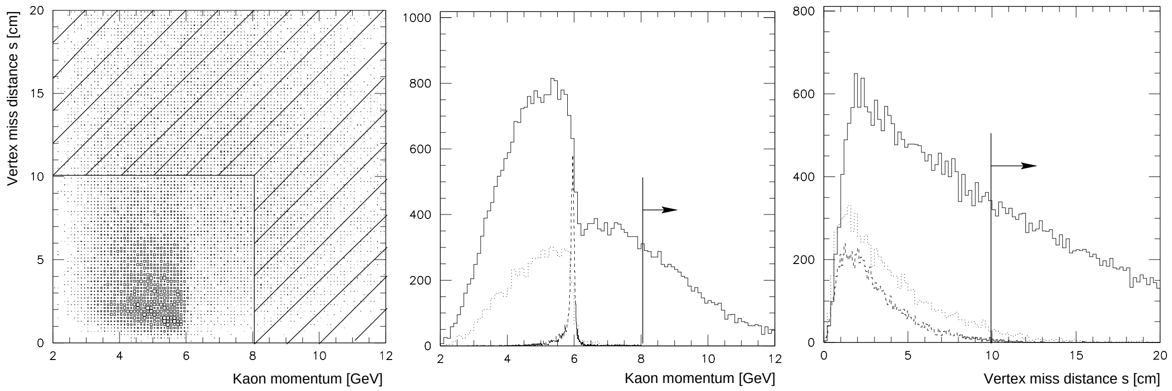

Figure 4.4: Scatter plot and projections of 3trk events, surviving all but the cuts displayed. The solid line in the projections represents all events, the dashed line shows the distribution for identified K_τ events and the dotted line is the distribution for K_{DAL} events.

them do not reconstruct the space points in the road assigned to the clump. Such events are either triggered from K^+ decays downstream of the first two MWPC's or are simply noise. Another possible source is tracks from pions in the beam decaying into a muon and a neutrino. For two thirds of the rejected events, we found enough space-points in the roads, but the space-points could not be combined into three tracks. These events are also mainly noise in the sense that the reconstructed space points do not belong to a real track, but arise from a high occupancy of the chambers. We recognize two main difficulties of our setup: the lack of a fast detector element in the upstream part of the apparatus to reject events triggered by ghost tracks or decays downstream of P1/P2 on the trigger level and the large occupancy in the MWPC. The first problem was overcome for the run in 96 by installing a fourth hodoscope between P1 and P2 and requiring three kinematically reasonable coincidences between the A•SH and this new counter. The second problem was improved by a tighter timing of the MWPC.

Cut	3trk stream	Tau stream
$N_{trkinvtx} = 3$	52%	80%
s < 10	26%	12%
2 pos + 1 neg	4%	3%
$P < 8$	3%	1%
accepted events	15%	4%

Table 4.3: Rejection factors of the Pass1 cuts for 3trk and Tau events. All numbers refer to the whole sample of events.

This first pass is very computer time consuming. It takes about 15 μsec to process a single event on a Dec Alpha 250/266. A typical, 8 mm tape needs about 13-15 hours. With 2-3 workstations continuously running, it took us several months to complete Pass1. After completion of Pass1, we had 21 8 mm tapes in hand containing about 60 million 3trk events.

4.5 Second offline analysis stage: Pass2

The main emphasis of Pass2 is particle identification. In addition, all tracks and vertices are re-fitted using trajectory integration with a step size of 20 cm. The same kinematical cuts as in Pass1 are imposed again. This does not reject many events, but it prepares for the following analysis. Pass2 generates four different output streams, as listed below, where a single event can be written to multiple streams, using the Pass1 3trk data as input:

1. EEPS: This stream is dominated by K_{DAL} events. It requires the identification (see below for a list of the criteria) of an electron/positron pair. No particle identification on the third track is imposed and no additional kinematical cuts are applied. Not only events with an ELER trigger latch, also PME triggers can be written to this stream. Contributions from the latter are events with an $e^+\mu^+e^-$ signature originating either from $K_{\mu 3}$ decay, $K^+ \to \pi^0\mu^+\nu$, followed by a Dalitz decay of the π^0 or $K_{\pi 2}$ decays, $K^+ \to \pi^+\pi^0$, where the π^+ decays into a muon and a neutrino and the π^0 undergoes a Dalitz decay. Almost 70% of the Pass1 data satisfy the above conditions. Due to this large number, this stream is prescaled in the software by another factor of 20, reducing the output to 3.5% of the Pass1 data.

2. HIMS: This stream will be used to select $K_{\pi ee}$ and $\pi^0 \to e^+e^-$ events. It requires the identification of a pion, an electron and a positron. Additionally the momentum of the reconstructed kaon is constrained to the region between 5 GeV and 7 GeV and the invariant mass of the e^+e^- pair has to be above 80 MeV. These two kinematical cuts are imposed to reject K_{DAL} events. No requirements on the trigger latch are made. This stream includes about 2.5% of the Pass1 data.

3. EEGG: This stream is dominated by $K^+ \to \pi^+\pi^0\pi^0$ with one π^0 making a Dalitz decay, $\pi^0 \to e^+e^-\gamma$, and the other π^0 decaying into two photons. This decay chain has a combined branching ratio of 2.0×10^{-4}. But the main purpose for this stream is to search for $K^+ \to \pi^+\pi^0e^+e^-$, which is a rare decay that has never been seen, and is of some theoretical interest in chiral perturbation theory. To be included in this stream, an event is required to have in addition to the three identified charged tracks

at least two photons, where the invariant mass of two photons has to be between 105 MeV and 165 MeV indicating a decay of the π^0, and the total reconstructed momentum, including the two photons, has to be below 7 GeV. About 1% of the Pass1 data fulfills these constraints.

4. PME: Events included in the PME output stream are required to have an identified pion, muon and electron in the final state and the momentum of the reconstructed kaon has to be between 5 GeV and 7 GeV. No constraint is made on the trigger latch. This stream comprises about 3.5% of the Pass1 data.

Of use to this thesis are only the EEPS and the PME output streams.

Particle identification involves matching the signals of the two Čerenkov counters, the calorimeter and the muon stack with tracks as described in section 4.3.6. For each track it is decided whether it satisfies one or more particle identification hypotheses, i.e. a track can have an ambiguous particle ID.

The cuts applied to identify a given track in Pass2 as an electron, a muon, a pion or a photon are:

Electron:	- More than 0.0 photo electrons in C1L (C1R)[†]
(Positron)	- More than 0.0 photoelectrons in C2L (C2R)
	- E/P greater than 0.5
Muon:	- Distance b between B-counter and projected track less than 10 σ_B.
	- At least 50% of the expected hits in the muon chambers.
	- Less than 450 MeV energy deposited in the calorimeter for this clump.
Pion:	Two of the three following requirements have to be met:
	- Less than 1.5 photoelectrons in C1.
	- Less than 1.5 photoelectrons in C2.
	- $\lvert E/P - 1\rvert > 0.2$
Photon:	- More than 400 MeV energy deposited in clump.
	- Deposited energy in the 2×2 clump divided by deposited energy in the 3×3 clump has to be larger than 0.9.
	- Cluster timing better than ± 5 ns.
	- A-counter veto within ± 10 ns.

[†] Considering the hardware threshold of the Čerenkov counters, this cut corresponds to 0.25 photoelectrons for in-time light.

Only Čerenkov ADC-signals with a TDC-timing better than 5 ns are assigned to a track.

The effect of the individual cuts is shown in the Figures 4.5 (electron identification), 4.6 (muon identification) and 4.7 (pion identification). Table 4.4 summarizes the efficiencies of the cuts. They are calculated by removing the element specified from the identification requirement. None of these are very stringent, the emphasis is placed on efficiency.

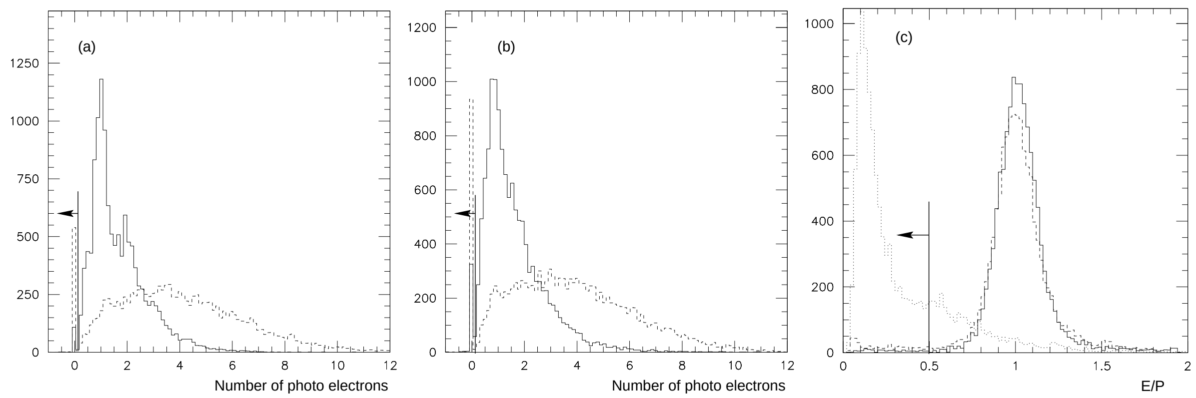

Figure 4.5: a) Response of C1L to incident electrons (solid) and of C1R to positrons (dashed) from K_{DAL} decays. Clearly visible are the one and the two photoelectron peaks. b) The same distributions, but now for C2. c) E/P for K_{DAL} events. The solid curve represents electrons, the dashed curve shows positrons and the dotted curve originates from pions.

	C1PE	C2PE	E/P	b	MEFF	ECLP	Tot. eff.
e^-	99.4%	97.4%	98%	—	—	—	95%
e^+	95.4%	93.7%	98%	—	—	—	90%
μ	—	—	—	94.2%	94.8%	93.8%	83.7%
π^-	99.6%	98.9%	94%	—	—	—	99.9%
π^+	97.5%	96.5%	94%	—	—	—	99.6%

Table 4.4: Efficiencies of the Pass2 particle identification. Values quoted for e^-/e^+ are from K_{DAL} events (ELER trigger), efficiencies for muons are based on $e\mu e$-events (see Fig. 4.6) extracted from PME trigger data and the values for the pions are estimated using K_τ events (TAU trigger).

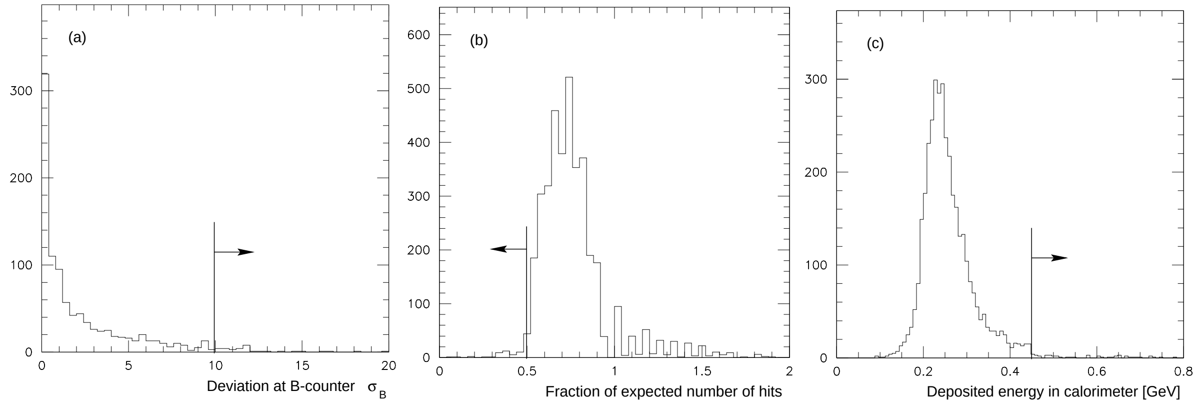

Figure 4.6: a) Deviation σ_B between hit in B-counter and projected track. b) Fraction of the expected number of hits found in the muon chambers. c) Deposited energy in calorimeter from muons. All three plots are based on events with an $e\mu e$ signature, i.e either $K^+ \to \pi^0\mu^+\nu$, followed by a Dalitz decay of the π^0 or $K^+ \to \pi^+\pi^0$, with $\pi^+ \to \mu^+\nu$ and the π^0 makes a Dalitz decay.

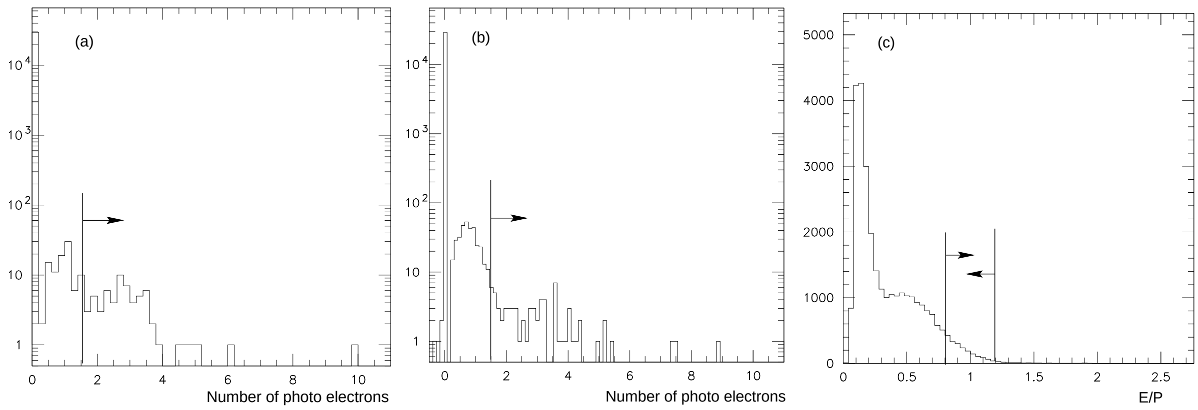

Figure 4.7: a) Logarithmic representation of the response of C1 to incident pions from K_τ decays. b) The same plot for C2. c) E/P for K_τ events. The region between the two arrows is excluded by the cut.

4.6 Final analysis: Pass3

About 2.1 million $K_{\pi\mu e}$ candidates survived Pass2. Most of these events can be assigned to one of the following three classes:

1. K_τ events as described in chapter 3.1. Such events tend to have a low $\pi\mu e$ invariant mass, since particles are identified incorrectly in the reconstruction.

2. K_{DAL} events: This is recognized as a dangerous background, because it can be measured with a correct invariant mass and is also physical, i.e. many reconstructed variables will show a 'good' distribution. The rejection comes from particle identification and from the fact that there is a missing neutral particle.

3. Accidentals, i.e. random associations of the correct final state particles: Timing cuts and kinematical reconstruction have to be used to reject this background.

This final pass analyses the remaining events with a significantly improved code. In Pass1 and Pass2, the track with the best χ^2 assigned to a clump is sought. In Pass3 up to 3 tracks per clump are kept (section 4.3.3 and 4.3.5), resulting in a 25% higher K_τ yield. For a second improvement, the collection of space points is repeated after the track finding. Since the track angle is known at this stage, hits in the MWPC's along the track can be searched and compared to the initial space point finding where only crude assumptions about the track angle could be made. The kinematical reconstruction can be further improved by looking for 'space points' with only two wire hits for those tracks that do not have space points in all four chambers. Additionally, this final pass integrates the trajectory with a step size of 5 cm to fit tracks and vertices. Finally the alignment of the MWPC's and the field maps for the two spectrometer magnets could be improved slightly. We found that mapping the left side field of D6 onto the right side of D6 leads to a tighter $M_{\pi\pi\pi}$ mass distribution and also to a slightly smaller vertex miss distance than using the original right side map of D6. All the improvements mentioned above sum up to the tighter distributions shown in Fig. 4.8.

Pass3 cuts can be divided into four classes: timing cuts checking the in-time quality of the tracks, kinematical cuts, i.e. cuts on different reconstructed parameters such as quality of the vertex fitting or phase space of the kaon, fiducial volume cuts, i.e. cuts on positions of particles in the different detector elements, and cuts on the particle identification.

At the end of the signal search, we will present a plot, showing the vertex miss distance s versus the invariant mass $M_{\pi\mu e}$ of the remaining $K_{\pi\mu e}$ candidates. It is instructive to inspect this plot after each cut from now on, to visualize the effect of the cut. We start from the situation after Pass2 presented in Figure 4.9.

4.6.1 Timing cuts

The most important factor in any timing system is its resolution. The major sources of timing variations in our system are walk, different path lengths and different momenta of the daughter particles and the jitter of the TDC start, which is determined by T0.

Walk is caused by variations in the amplitude of the signal introduced into a discriminator with a fixed threshold. Considering two signals exactly coincident in time but with

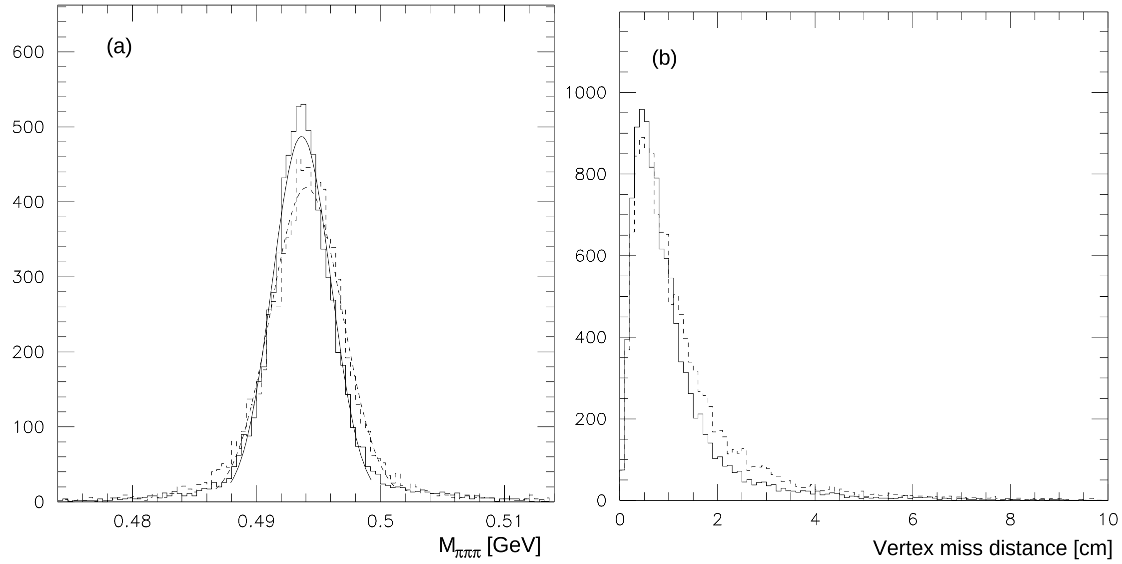

Figure 4.8: a) Reconstruction of the invariant mass of K_τ events for Pass2 kinematical reconstruction (dashed) and Pass3 reconstruction (solid). The resolution improves from 2.9 MeV to 2.3 MeV. The centroid agrees with the expected kaon mass within 0.05 MeV. b) Vertex miss distance for Pass2 (dashed) and Pass3 (solid) reconstruction.

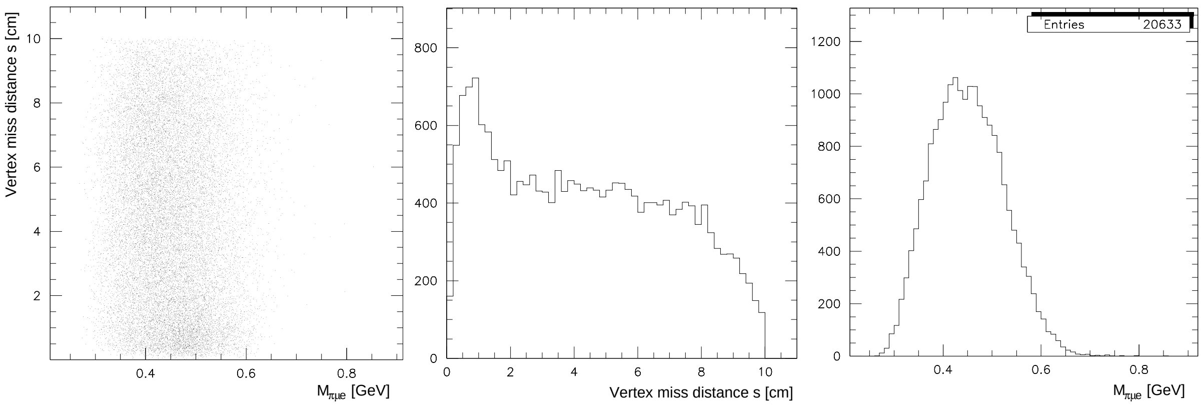

Figure 4.9: Vertex miss distance s vs. $M_{\pi\mu e}$ mass distribution after completion of Pass2. These plots comprise about 1% of the data.

a different amplitude, then the signal with the smaller amplitude will cross the discriminator threshold later than the signal with the larger amplitude. Figure 4.10a shows this correlation for electrons in the calorimeter. A lookup table of corrections as a function of the deposited energy in the detector is generated. These corrections, also called slewing corrections, produce an essentially walk-free timing as shown in Figure 4.10b. The timing resolution of electrons in the calorimeter is improved to 1.22 ns compared to 1.90 ns before the correction. A similar correction is also applied to the Čerenkov counter timing.

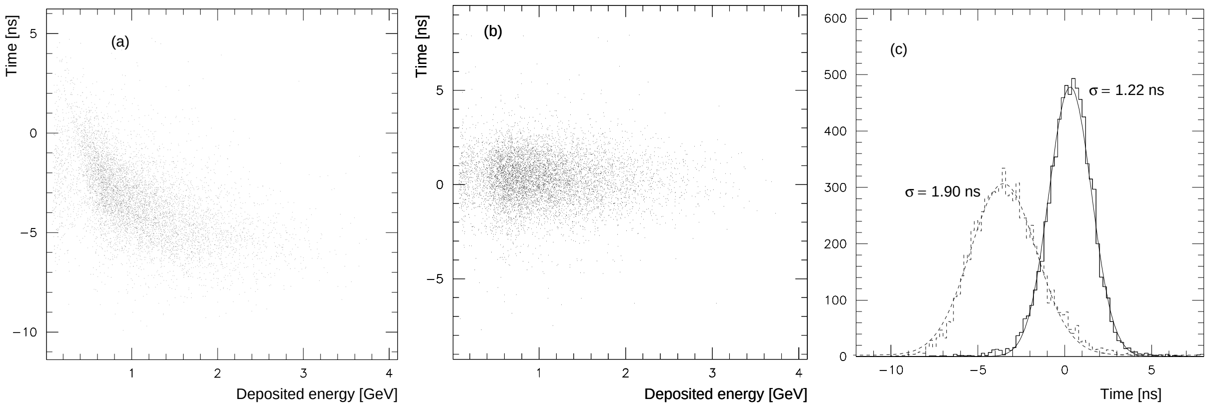

Figure 4.10: a) Timing of electrons in calorimeter versus deposited energy in the module without walk correction. b) Same plot, but now walk corrected. c) A projection shows the improvement of the corrected (solid) against the uncorrected signal (dashed).

Next we shift the mean timing of each PMT to zero and thereby correct for different effects, e.g. the slightly imperfect zero calibration of the PMT's, and the momentum dependence, since slow particles tend to have a larger X-coordinate than fast particles. This correction does not improve the resolution very much, but it centers nicely the timing at zero as shown in Figure 4.11a. More important is the correction of the T0 jitter. This is done by measuring the time of the hits relative to each other, i.e. by subtracting the mean value of the timing of the three tracks in the A-counter and the calorimeter from the individual measurements. This narrows the resolution of the timing for electrons in the calorimeter to 0.44 ns (Fig. 4.11b). Table 4.5 summarizes the timing resolution of electrons, positrons and pions obtained from K_{DAL} events in the individual detectors.

Particle type	Calorimeter	A-counter	C1L	C1R	C2L	C2R
Electron	0.44 ns	0.65 ns	0.87 ns	-	0.88 ns	-
Positron	0.45 ns	0.67 ns	-	0.71 ns	-	0.77 ns
Pion	0.56 ns	0.67 ns	-	-	-	-
Muon	0.59 ns	0.66 ns	-	-	-	-

Table 4.5: Timing resolution of different particles in the E865 detector.

After tightening the timing, we are ready to measure the in-time quality of an event.

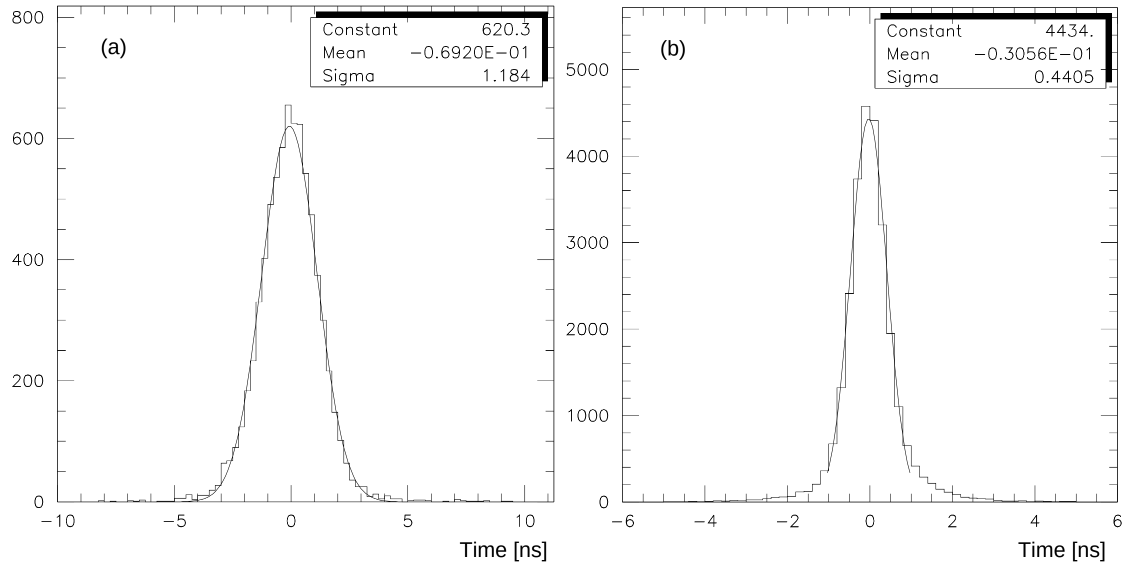

Figure 4.11: a) Timing of electrons in calorimeter after the shift of the mean time. b) Timing resolution after correction of the T0 jitter.

This is done by measuring the root mean square spread $TRMS$ of the calorimeter and the A-counter timing, i.e:

$$TRMS = \sqrt{\frac{\sum T_{ACNT}^2 + \sum T_{SHOW}^2}{6}} \tag{4.22}$$

where the sum runs over the three tracks. A cut at $TRMS = \sqrt{1.5}$ rejects about 56% of the $K_{\pi\mu e}$ candidates. About 90% of the good K_{DAL} and 81% of the good K_τ events are kept (Fig. 4.12). We calculate the latter two numbers, i.e. the efficiency of the cut, by removing the element specified, in this case the cut on $TRMS$, from the list of requirements which will be summarized in section 4.6.12.

Figure 4.13 indicates the effect of this cut. Comparing to the situation before the cut (Fig. 4.9), we recognize that this cut preferentially rejects events with a large vertex miss distance s. This is consistent with what one might expect, since a large s is an indication of an accidental association of the correct final state particles which this cut was mainly designed to reject.

4.6.2 Track quality

After fitting the track momentum, the quality of a track can be judged by a value of χ^2 (Equation 4.17). No cut on this value was made during the reconstruction of the event.

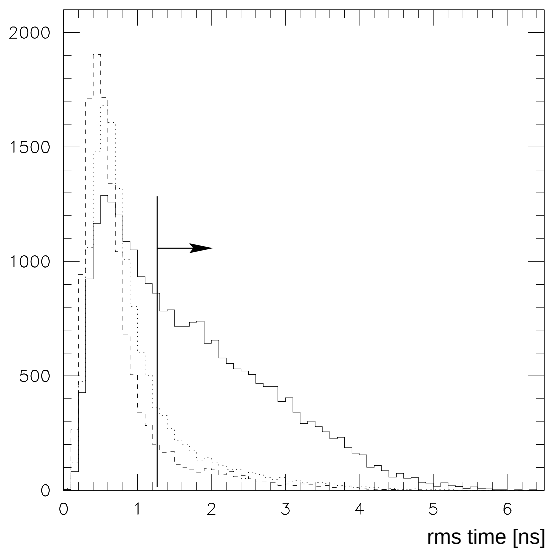

Figure 4.12: Root mean square spread of the calorimeter and A-counter timing ($TRMS$). The solid line represents $K_{\pi\mu e}$ candidates surviving Pass2, the dashed line shows K_{DAL} events and the dotted line K_{τ} events.

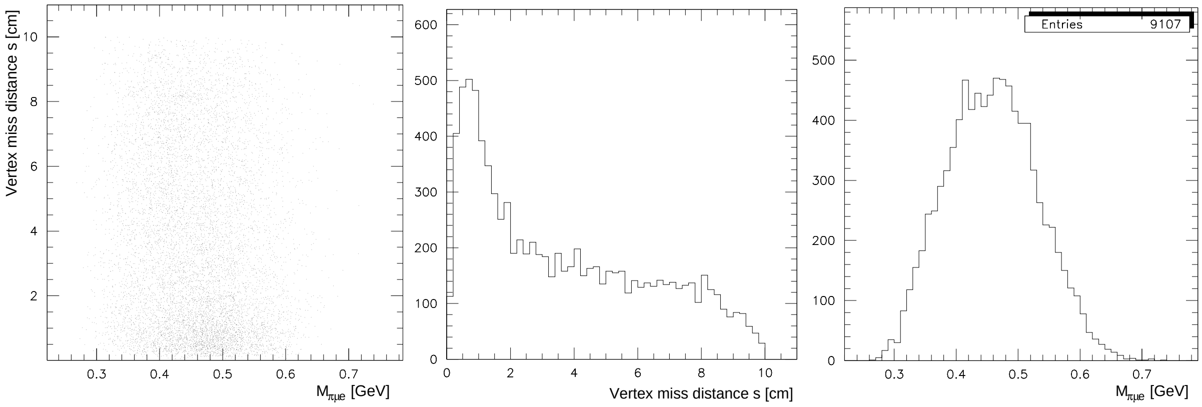

Figure 4.13: Vertex miss distance s vs. $M_{\pi\mu e}$ mass distribution after application of the timing cut. These plots comprise about 1% of the data sample.

But before we make the cut, we can improve the value of χ^2 slightly. Up to now, i.e. in Pass1 and Pass2, the measurement error σ entering the χ^2 calculation in the momentum fitting is assumed to be the resolution of a single wire plane. This neglects the contribution from multiple scattering of the particle in the detector. An improved χ^2 results when the correlation between mismeasurements in different MWPC planes due to multiple scattering are considered, too, i.e by calculating the inverse of the correlation matrix for track measurement correlations between the individual wire planes. The improvement is documented in Fig. 4.14a. The mean value of the uncorrected distribution is 2.4, while it becomes 1.8 after the correction. The main reason for the discrepancy from the expected value of one is an imperfect knowledge of the field map for the spectrometer magnets.

Figure 4.14b shows the improved χ^2 distribution for good K_τ events, good K_{DAL} events and $K_{\pi\mu e}$ candidates. No significant difference between the three channels is observed. We will apply a very loose cut on the χ^2, rejecting only the very badly mismeasured tracks. A cut at 20 rejects about 15% of $K_{\pi\mu e}$which passed all the previous cuts while keeping 94% of the good K_τ and 93% of the good K_{DAL} events. Common to all rejected events is that they are of low quality, i.e. they have in general a larger vertex miss distance s and a wider invariant mass distribution than good events. Of course, rejecting only 15% of the $K_{\pi\mu e}$ candidates, this cut does not significantly change the vertex miss distance s versus invariant mass $M_{\pi\mu e}$ plot, hence we will not display it here.

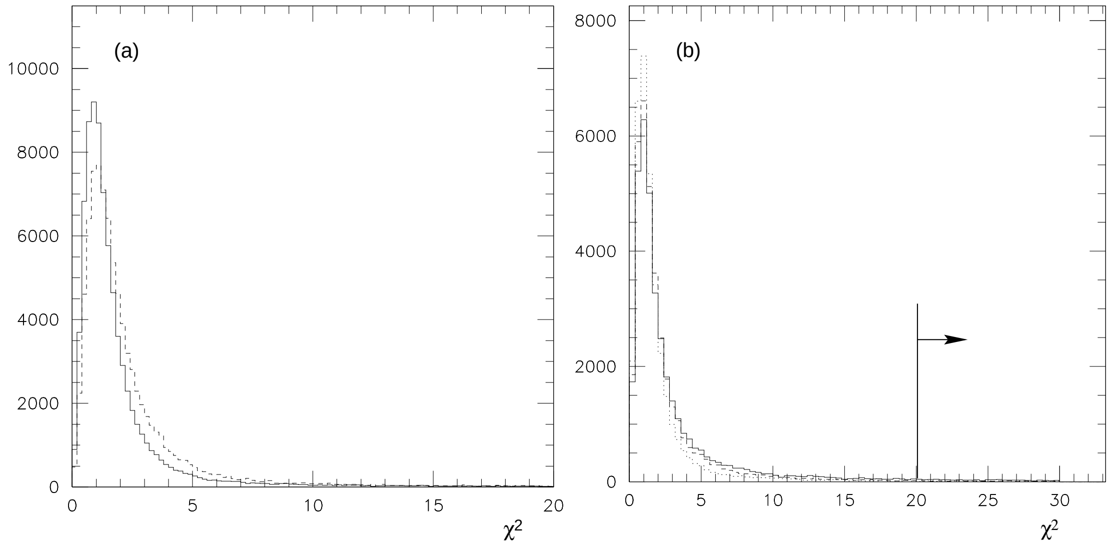

Figure 4.14: a) Track χ^2 of K_τ events corrected for multiple scattering (solid) and uncorrected (dashed) b) Track χ^2 for $K_{\pi\mu e}$(solid), K_{DAL} (dashed) and K_τ (dotted) events.

4.6.3 Target likelihood

This kinematical cut requires the phase space parameters of the kaon to be consistent with those of a beam kaon originating from the target, i.e. the reconstructed kaon is demanded to point back to the target. This is a very powerful cut for reducing background from accidentals. It will also reject decays with a missing neutral particle. Since the reconstruction of the kaon is incomplete for such events, it is very improbable that they will track back to the target.

Figure 4.15 shows a K_τ event that propagates back to the target. Such events have no missing energy and provide an excellent source of reconstructed kaons to define the phase space of the beam. A hard edge approximation of the beam line magnets is used to track the kaon back to the target. The existence of collimators and appertures in the beam line is ignored. Figure 4.16 shows the distributions of the five parameters X, Θ_X, Y, Θ_Y and P and their correlations at the location of the target for K_τ events. Rather than simply cutting on the isolated projections of the parameters, a likelihood test takes into account the partly pronounced correlations between the parameters. Lookup tables for all three scatter plots are generated by calculating the logarithm of the ratio of the numbers of entries in each 'bin' in the two-dimensional phase space divided by the total number of entries in the scatter plot. The probability that any event is consistent with the target hypothesis is now proportional to the sum of the three likelihoods. Beside the target, any point in the beam line could have been selected for this cut, but the target is preferred since the beam is most tightly focused in this point.

Figure 4.17 shows the target likelihood distributions for $K_{\pi\mu e}$ candidates surviving all the previous cuts and and good K_τ events. With a cut at -17 approximately 91.1% of good K_τ events are kept. The effect of this cut on the $K_{\pi\mu e}$ candidates is dramatical, 92% are rejected. By looking at the plot displaying the vertex miss distance, we recognize that most of the remaining events have a pretty tight s, indicating that they are real decays and not accidentals (compare e.g. with Figure 4.8 showing the vertex miss distance for K_τ data events). The invariant mass plot shows two clearly distinct regions, a first one located around 400 MeV and a second one can be found between 450 MeV and 600 MeV. Recalling the discussion of the background (section 3.1), we can expect that the first region mainly consists of K_τ events. The peak has a small width, indicating no missing neutral particles, and it is located below the kaon mass of 493 MeV, indicating an incorrect labeling of two pions as an electron and a muon. We can also expect that the second region is mainly composed of K_{DAL} events indicated by the wider peak. It is also not a contradiction that we reconstruct an invariant mass around the kaon mass, since labeling the particles wrong adds mass, which can be canceled by the lost mass due to the missing photon.

4.6.4 Fiducial volume cuts

Fiducial volume cuts are designed to exclude regions in the apparatus which provide unreliable reconstruction results, i.e. they are intended to prepare for the final particle identification and kinematical cuts.

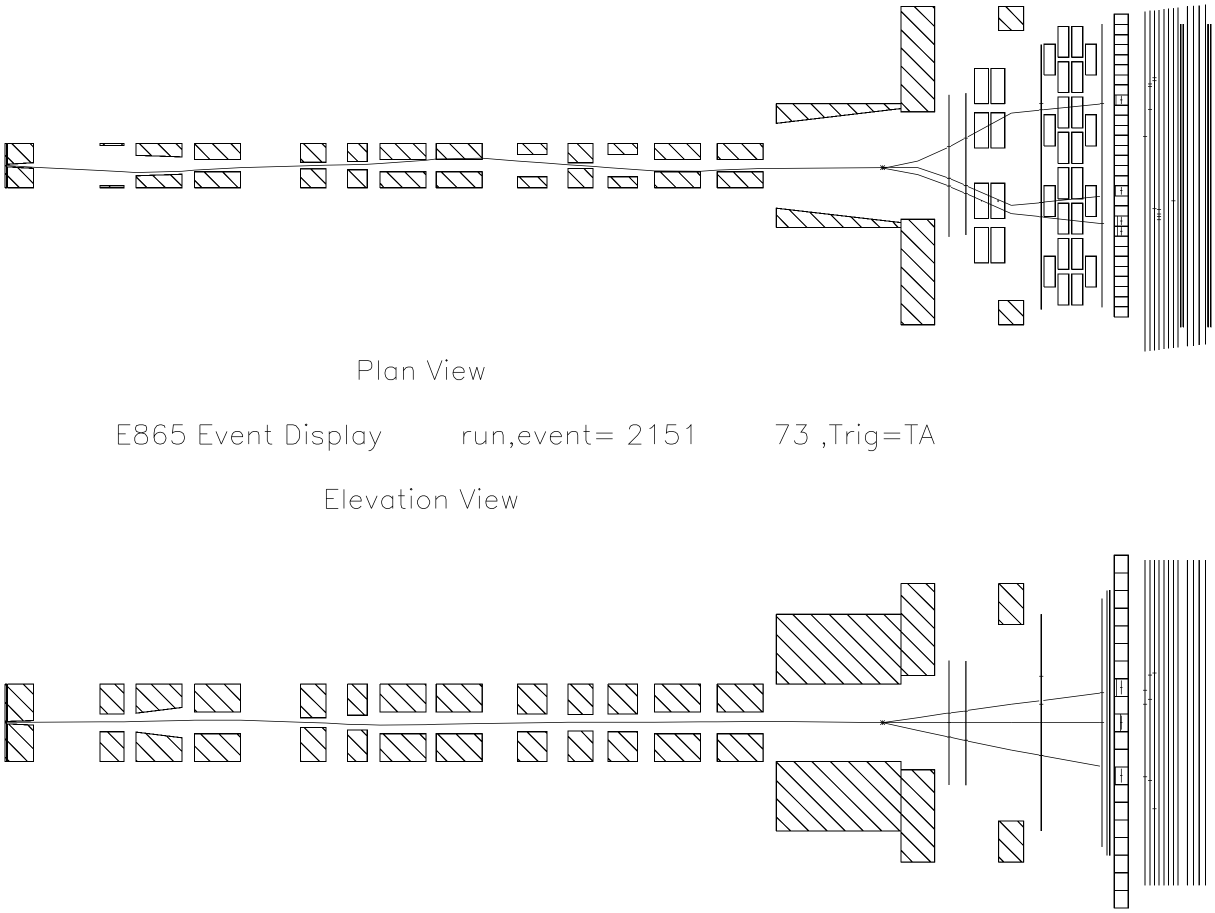

Figure 4.15: Display of a fully reconstructed K_τ event.

Decay volume

Figure 4.19 shows the resolution of the invariant mass $M_{\pi\pi\pi}$ of K_τ events vs. the Z-position of the vertex. We clearly recognize poorer mass resolution for position upstream of Z = -490 cm. There are two possible explanations for this behaviour. First, decay products in this region are influenced by the magnetic field of Q9, the last quadrupole magnet, which ends at Z = -500 cm. A second reason might be scattering in the upstream window of the decay volume. To avoid such difficulties, the vertex is required to be located downstream of Z = -490 cm. This eliminates 5% of $K_{\pi\mu e}$ events passing all the previous cuts, 6% of K_τ and 2% of K_{DAL}. The discrepancy between the K_{DAL} and K_τ rejection is easily understandable. Due to the larger mass of the daughter particles in K_τ, they tend to follow more parallel trajectories than the daughter particles originating from K_{DAL} decays. Hence, the acceptance for K_τ events is mainly limited by the dead regions in the

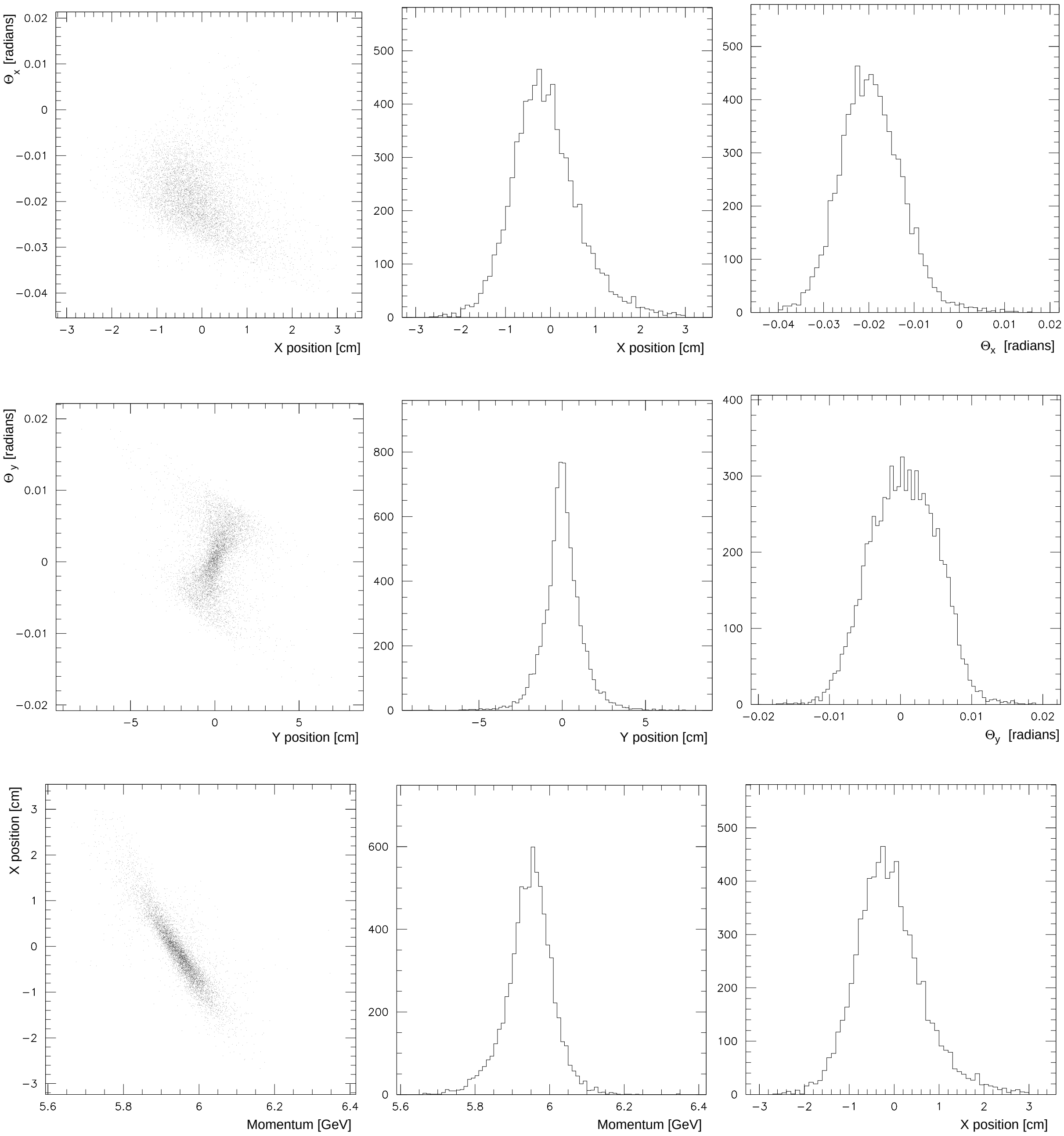

Figure 4.16: X vs. Θ_X, Y vs. Θ_Y and P vs. X distributions and appertaining projections of the individual variables of reconstructed K_τ events at the location of the target.

MWPC's, while the acceptance for K_{DAL} events is restricted by the aperture of the decay volume and of the spectrometer magnets. This explains why K_τ decays originate further upstream and K_{DAL} events further downstream in the decay volume.

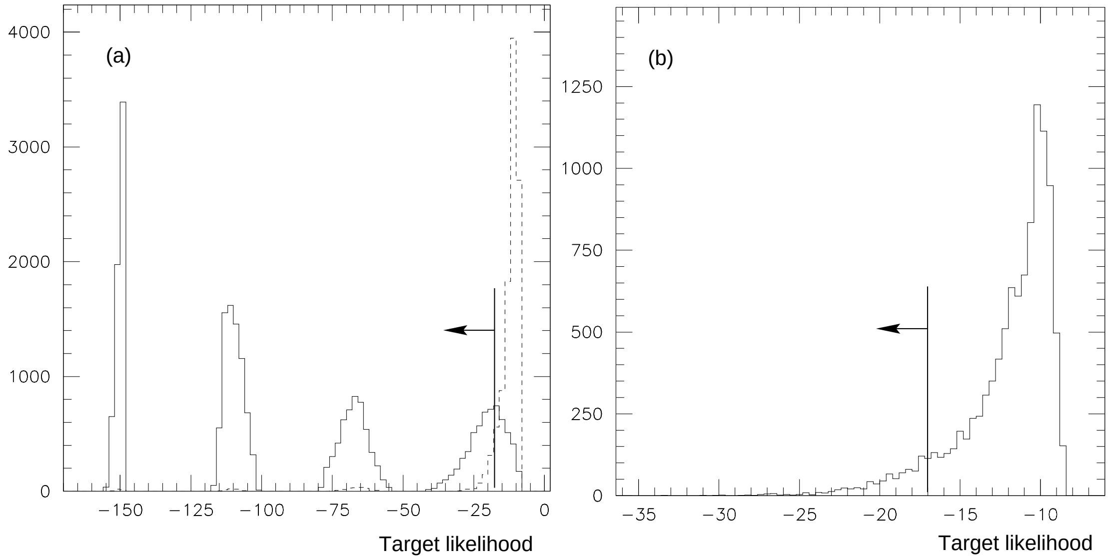

Figure 4.17: a) Target likelihood distribution of $K_{\pi\mu e}$ candidates (solid) and K_τ events (dashed). b) shows again the distribution for K_τ events.

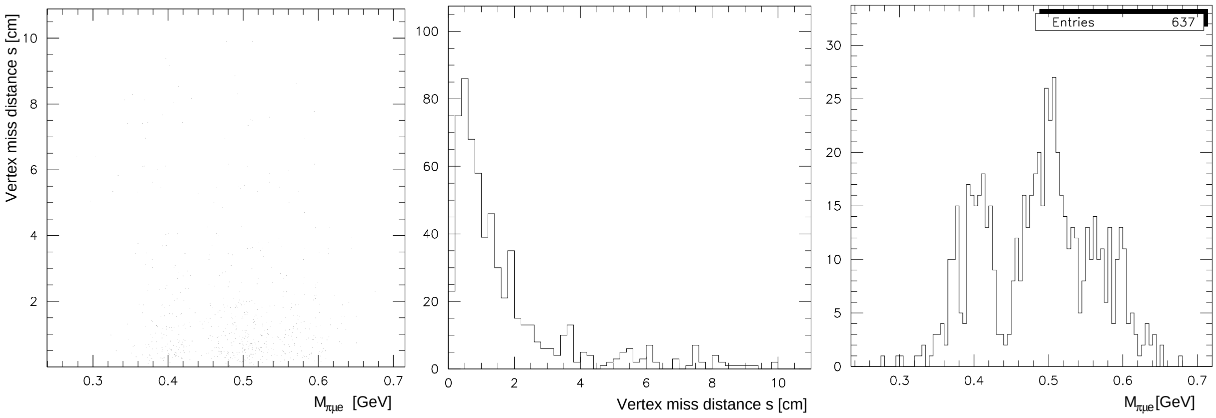

Figure 4.18: s vs. $M_{\pi\mu e}$ mass distribution after application of the target likelihood cut. These plots comprise about 1% of the data.

Čerenkov counters

Figure 4.20a shows a plot of the X-position versus the Y-position at the mirror of Čerenkov counter C1 of positrons from K_{DAL} events, being identified in C2 and the calorimeter as e^+ but not in C1. Figure 4.20b shows a similar distribution for C2. The heavily populated regions in the plots are especially dangerous since they might lead to a misidentification of an e^+ as a π^+ and hence to background. These regions of course correspond to the less

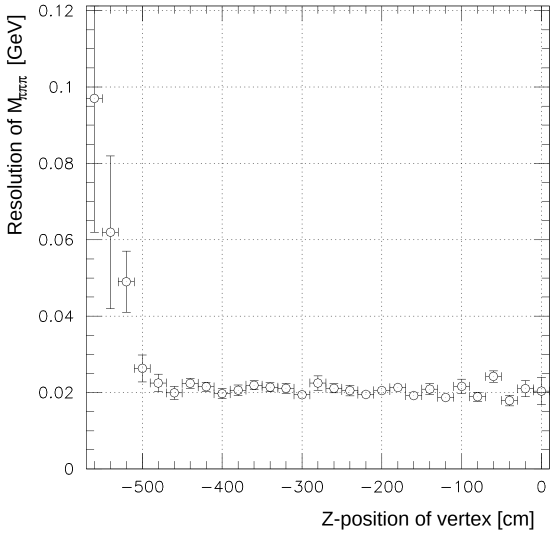

Figure 4.19: Resolution of the invariant mass $M_{\pi\pi\pi}$ of K_τ events vs. the Z-position of the vertex.

efficient parts in the Čerenkov counters (Fig. 3.13). Instead of simply vetoing all $K_{\pi\mu e}$ candidates with a pion in this region, we require that the known combined inefficiency of C1 and C2 mapped onto the position of the pion track, is less than 0.01, i.e. $(1-\epsilon_{C1}) \times (1-\epsilon_{C2}) < 0.01$. By using this requirement, we cut about 8% of the acceptance for $K_{\pi\mu e}$ events, compared with more than 40% we would loose by cutting geometrically. This cut rejects about 45% of the remaining $K_{\pi\mu e}$ candidates. It's safe to assume that most of the rejected events are in reality K_{DAL} events. This is also indicated by Figure 4.21, the lower mass K_τ-peak is now more pronounced than the higher mass K_{DAL}-peak compared to Figure 4.18.

4.6.5 Particle identification

The cuts to identify particles applied in Pass2 are pretty loose. The goal was maximum efficiency and came at the cost of some identification ambiguity.

On the beam-right side, it is important to make sure that positrons are not identified as pions or muons. This danger is already greatly reduced by the Čerenkov fiducial volume cut, described above. In combination with this cut, we require now for a track to be identified as a pion:

$$
\begin{aligned}
\text{PION} = \text{NOT}(\ &((\text{C1PE}>0.4 \text{ OR } \text{C2PE}>0.4) \text{ AND } \text{E/P} > 0.6) \text{ OR}\\
&((\text{C1PE}>0.4 \text{ OR } \text{E/P}>0.6) \text{ AND } \text{C2PE} > 0.4) \text{ OR}
\end{aligned}
$$

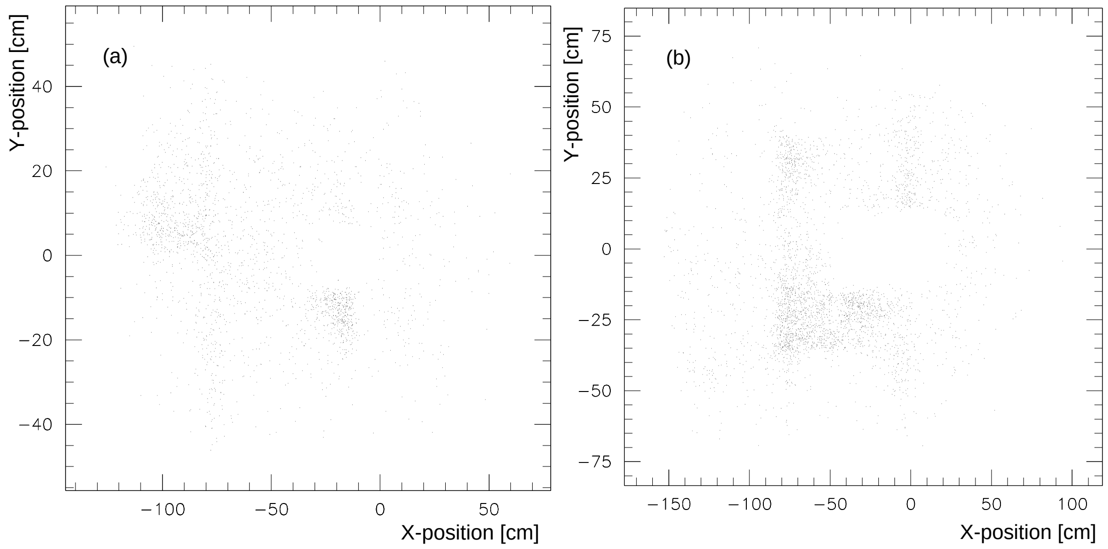

Figure 4.20: a) X vs. Y at Čerenkov counter C1 of positrons from K_{DAL} events identified in C2 and the calorimeter as e^+, but not in C1. b) Same distribution for C2.

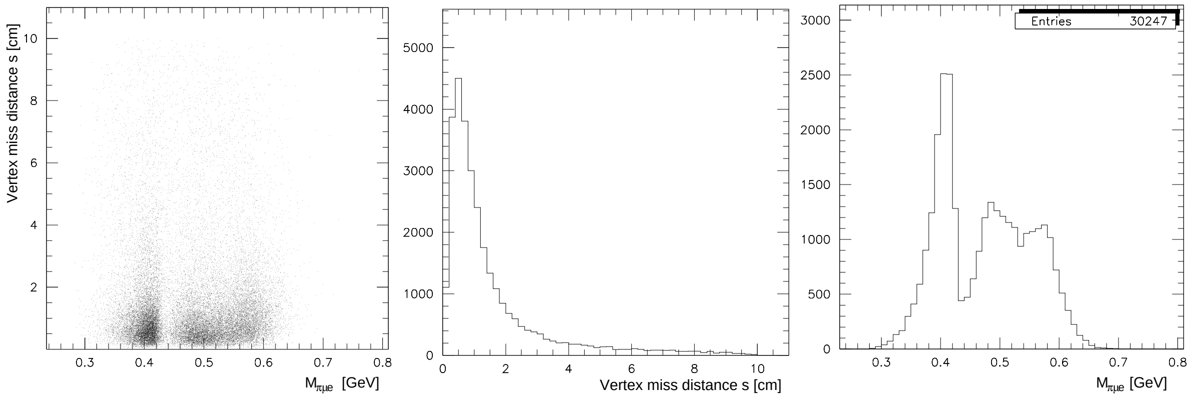

Figure 4.21: Vertex miss distance s vs. $M_{\pi\mu e}$ mass distribution after application of the Čerenkov fiducial volume cut. These plots comprise now all the remaining data.

((C2PE>0.4 OR E/P>0.6) AND C1PE > 0.4)	OR
(C1PE>1.5)	OR
(C2PE>1.5)	OR
(E/P>0.85)	)

Slightly different constraints on the TDC's than in Pass2 are used to calculate the number of photoelectrons. It is recognized that electrons might give Čerenkov light without an in-time TDC hit. This is due to the fact that the TDC stop is followed by a discriminator dead time of 20 ns while the ADC gate is 25 ns long. Hence, an early hit can block the TDC while the ADC gate is still open and can register hits. Always requiring an ADC- and a TDC-hit would result in a loss of efficiency of the Čerenkov counters. This loss can be estimated to be a few percent, since the rate in the PMT's close to the beam is about $1 - 2$ MHz. This can be avoided by adding also light which has a TDC more than 25 ns out of time associated to it, i.e. to calculate the number of photoelectrons, we add light which is either within ± 5 ns or more than 25 ns out of time and has at least 0.5 photoelectrons.

Clearly, the goal of this cut is not to properly identify pions, it is rather an 'anti-positron-cut'. Its efficiency for positively charged pions from K_τ events is 89.8% while only one in 6×10^4 positrons will pass it. The positron rejection is estimated using K_{DAL} events, where all but the cuts designed to identify positrons are applied. The rejection is then given by the ratio of total number of such events divided by the number of events where the positron pass the 'anti-positron-cut'. About 55% of the $K_{\pi\mu e}$ candidates get rejected. Applying the identical cut also on the muon rejects another 28%. Figure 4.22 documents the effects of this cut which eliminates most of the K_{DAL} background.

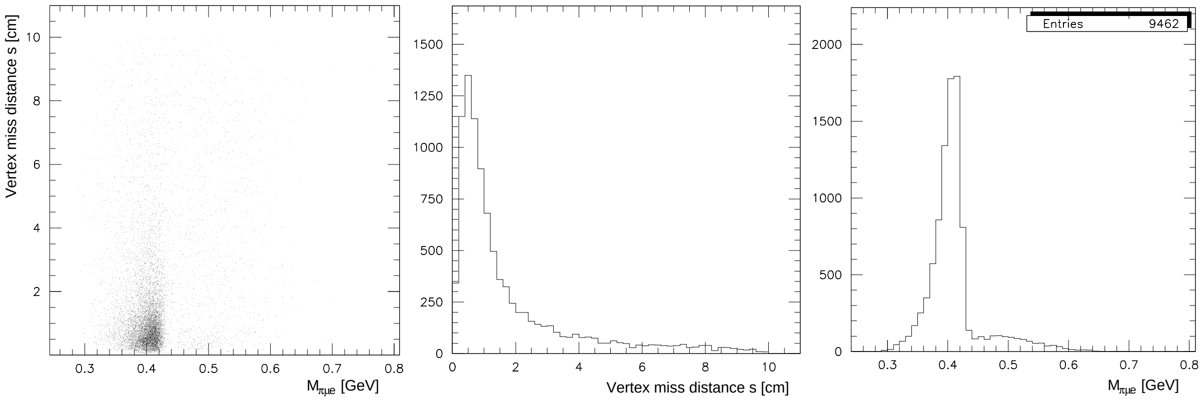

Figure 4.22: Vertex miss distance s vs. $M_{\pi\mu e}$ mass distribution after discriminating against positrons.

On the left side, the danger comes from pions being identified as electrons. Referring to chapter 3.6.2, we recognize that pions sometimes give light in the left side Čerenkov counters. The two most common causes for this activity are δ-rays produced in the counter window and parasitic electrons that cross the counter in the same area at the same time as the pion. By placing the minimum light cut at 0.3 photoelectrons and requiring the weighted mean time of all light contributing to the Čerenkov signal to be within ± 5 ns, and by tightening the E/P cut to $0.8 < E/P < 1.2$, we get a handle on this background. 89.1% of electrons and 88.2% of positrons in K_{DAL} decays pass it. The rejection against pions is estimated on a good sample of K_τ events, the requirement imposed on C1 results in a rejection of 1.2×10^{-3}, the C2 constraint gives 7.7×10^{-3} and the calorimeter adds another 4.1%, resulting in a combined rejection of pions against electrons of 4×10^{-7}, assuming the three contributions are independent. Shown in Figure 4.23 is the situation after applying the cut, it rejects about two third of the remaining $K_{\pi\mu e}$ candidates.

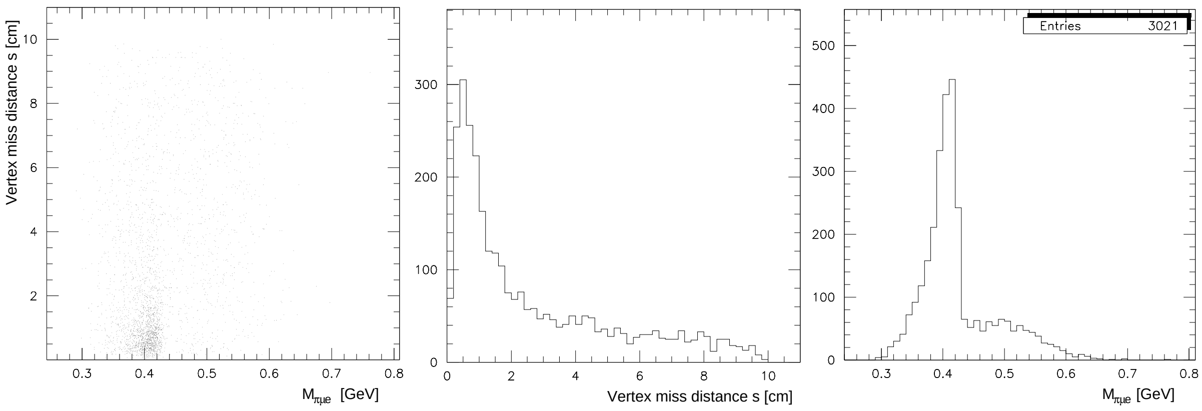

Figure 4.23: Vertex miss distance s vs. $M_{\pi\mu e}$ mass distribution after identification of the electron.

The decay of pions in flight, accompanying the kaons in the beam line, into a muon and a neutrino is an important source of background. An estimation leads to a muon rate outside the dead regions in the MWPC's of 25 MHz. An examination shows that about 10% of the 'pions' in the remaining $K_{\pi\mu e}$ candidates are in fact such beam muons. They have a typical energy of 3.5 GeV, i.e. they cross the whole muon stack. Looking at Figure 4.24 displaying the behaviour of the beam muons in the muon stack and in the muon hodoscopes, we recognize that for about 85% of the beam muons, the deviation b between the track projected from P4 onto the B-counter and the hit in the B-counter is less than 5 σ_B, about 92% have a c less than 5 σ_C (c is the deviation between the projected track and the hit in the C-counter) and for about 98% of the 'beam muons' more than 60% of the expected hits are found. Requiring the pions in $K_{\pi\mu e}$ to have a b larger than 5 σ_B, a c larger than 5 σ_C and less than 60% of the expected hits, pions can be discriminated against beam muons. On the other hand, about 2% of the pions from K_τ fulfill all the three constraints. Figure 4.25 shows the distribution of the vertex miss distance of the rejected events. No peak is recognizable, a clear indication of accidentals.

4.6.6 Additional tracks

In the previous section, we recognized that parasitic tracks are a potential source of background. This can be reduced without losing much data by limiting the number of

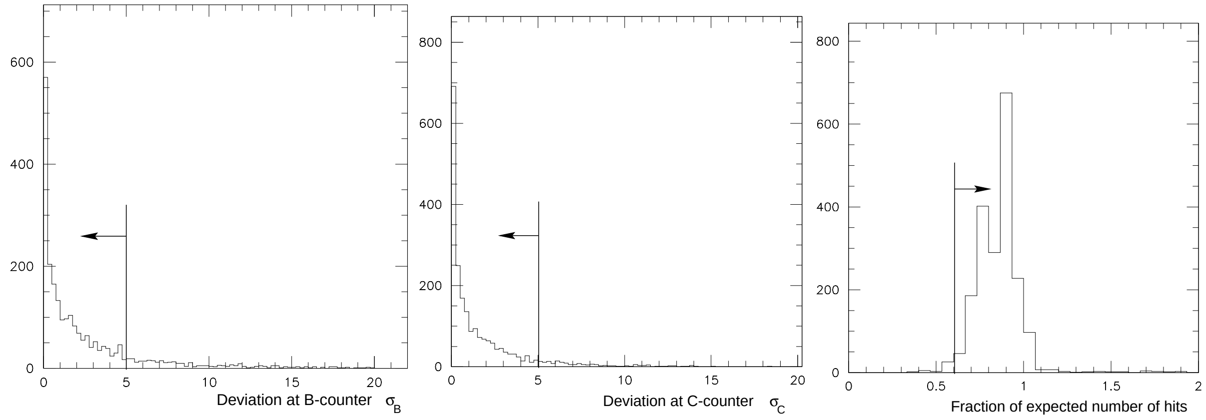

Figure 4.24: Deviations between the projected track from P3/P4 and the hit in the B-counter (b) and the C-counter (c) and the ratio of the number of found hits divided by the number of expected hits. The data in this plot are taken with a single trigger, i.e. only one A•SH is required for a T0 trigger.

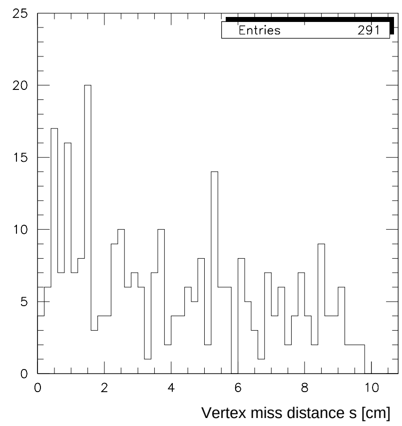

Figure 4.25: Vertex miss distance s for $K_{\pi\mu e}$ events where the pion is misidentified as a muon.

tracks in a single event to four. Even better would be, if we could restrict ourself to only events with exactly three tracks, but this would result in a loss of 15% of the K_τ data. By also allowing events with four tracks, this loss can be reduced to 1.3%. Considering the $K_{\pi\mu e}$ candidates, 9% of the remaining data is vetoed by this cut. Figure 4.26 shows the rejected events, most of them are in reality K_τ events.

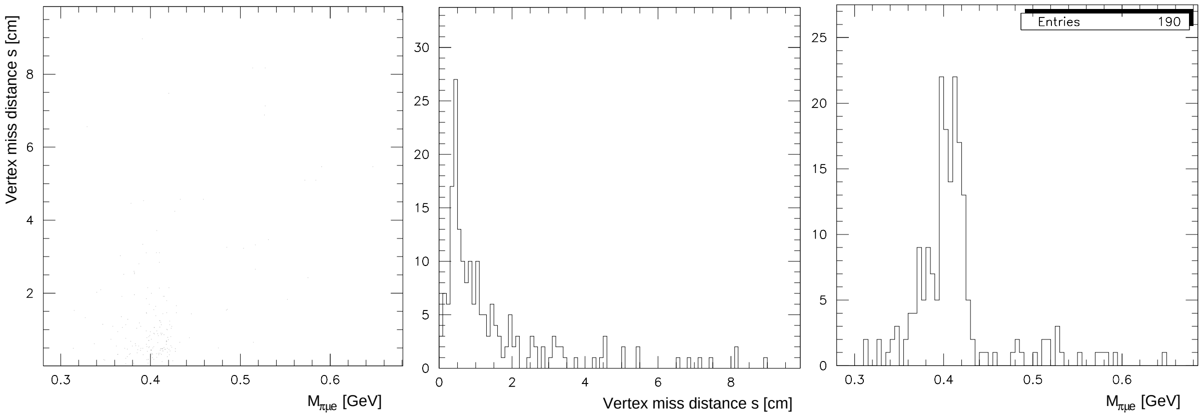

Figure 4.26: Vertex miss distance s vs. $M_{\pi\mu e}$ mass distribution for the events rejected by the restriction to maximum four tracks in a single event.

4.6.7 Pion on the left

On the beam left side, only 2.0 photoelectrons are expected in each Čerenkov counter. Poisson statistics then dictates that the left side counters will be 14% inefficient. Hence, we will reject all $K_{\pi\mu e}$ events where the pion is on the beam left side in either C1 or C2. Twenty $K_{\pi\mu e}$ candidates are rejected by this cut. Figure 4.27 displays the remaining $K_{\pi\mu e}$ events.

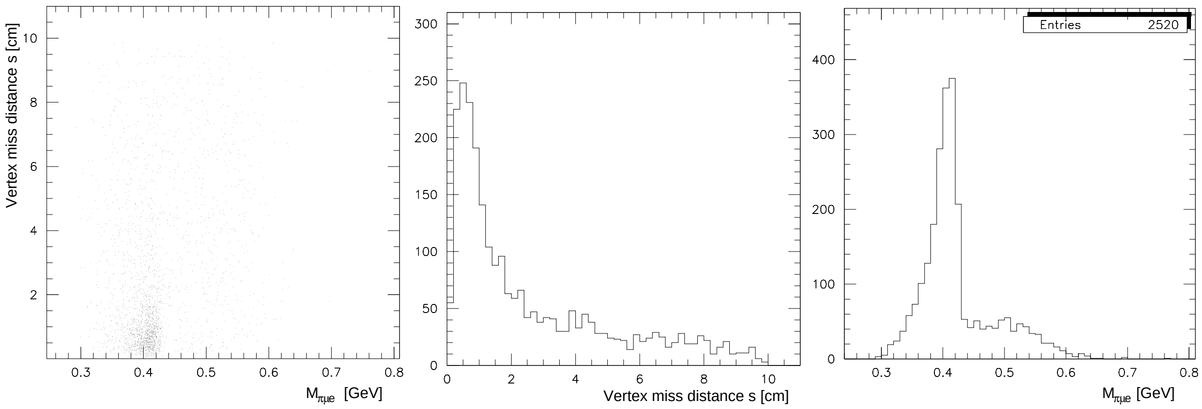

Figure 4.27: Vertex miss distance s vs. $M_{\pi\mu e}$ mass distribution after rejecting all events where the pion is found in either C1 or C2 on the beam left side.

4.6.8 $\mathbf{M}_{ee}$ invariant mass

Figure 4.27 still shows a few events with an invariant mass $M_{\pi\mu e}$ at the kaon mass of 493 MeV and with a small vertex miss distance s. We believe that most of these events are still from K_{DAL}. Since K_{DAL} is mediated by a virtual photon decaying into an e^+e^--pair, decays with a low M_{ee} invariant mass are highly favoured (section 3.10.2). Based on this supposition, Figure 4.28a shows the invariant mass M_{ee} of the electron and the pion, assigned to be a positron, and Figure 4.28b shows the same variable for the electron and the muon, assigned to be a positron. Especially in Fig. 4.28a a clear peak is visible at low invariant mass M_{ee}, indicating that these events are in reality K_{DAL}. Cutting at $M_{ee} = 50$ MeV keeps 90% of the good K_{DAL} events. Hence for $K_{\pi\mu e}$ we veto all events with a mass $M_{ee} \leq 50$ MeV. Comparing Fig. 4.27 with Fig. 4.29 we recognize that this cut almost cleaned up the region around the kaon mass at small s. This is the most dangerous part of the plot, the bulk of the remaining events located either at low mass $M_{\pi\mu e}$ or at large s can be easily rejected, as we will see below.

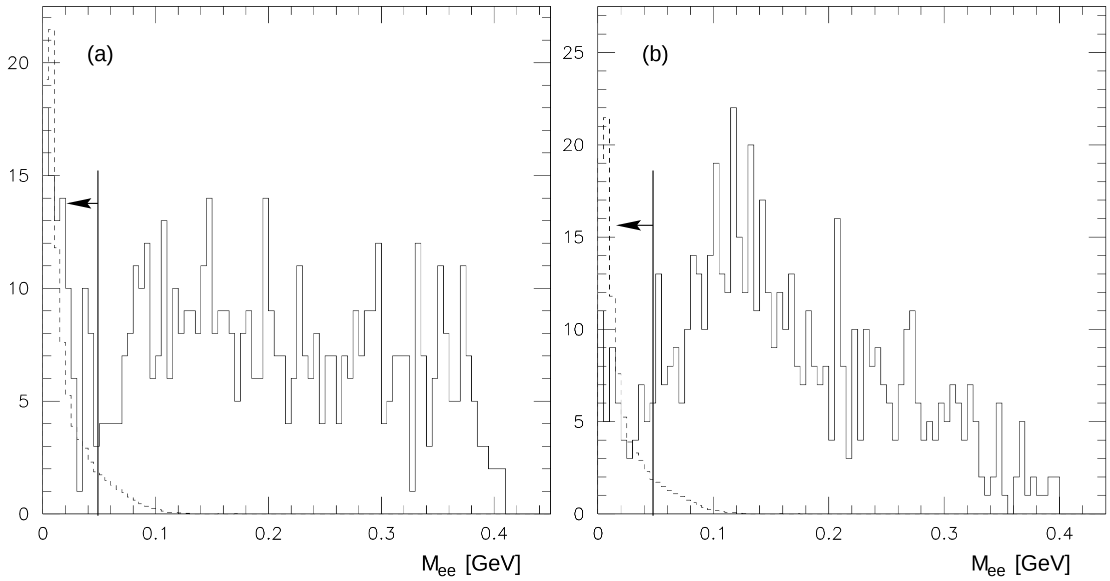

Figure 4.28: a) Invariant mass of the electron and the pion assigned to be a positron. b) Invariant mass of the electron and the muon assigned to be a positron. Both plots display only $K_{\pi\mu e}$ candidates with a mass $M_{\pi\mu e}$ above 0.44 GeV. For comparison, the M_{ee} invariant mass of K_{DAL} is also shown in both plots (dashed line).

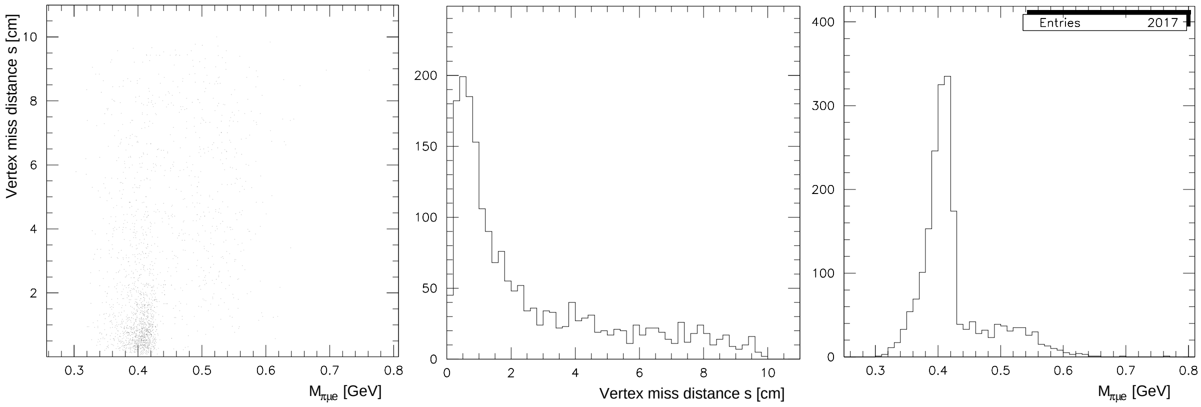

Figure 4.29: Vertex miss distance s vs. $M_{\pi\mu e}$ mass distribution after rejecting all events with an M_{ee} mass below 50 MeV.

4.6.9 Photon veto

Another handle on the K_{DAL} background is a photon veto, the detection of an in-time photon indicates a K_{DAL} decay. Photons are identified as particles having a signal in the calorimeter but not in the A-counter or, to be more precise:

- More than 400 MeV energy deposited in clump.
- Deposited energy in the 2×2 clump divided by the 4×4 clump has to be larger than 0.9.
- Cluster timing better as 2 ns.
- A-counter veto within 10 ns.

Figure 4.30a shows the ratio of the deposited energy in 2×2 modules divided by the deposited energy in 4×4 modules in the calorimeter with no associated A-counter signal for K_τ events. The events in the tail are not real photons, but leaking π-showers. A clump is defined by 3×3 modules, when energy is deposited outside this range a second clump is found with a low 2×2 divided by 4×4 ratio. Cutting this ratio at 0.9 gets rid of this background. Figure 4.30b displays the timing of photons from K_{DAL} events. The timing resolution is 0.49 ns consistent with that of the electron. Figure 4.30c shows the timing of photons in good K_τ events after elimination of all events with one or more tracks being identified as an electron or a positron. The remaining photons show no correlation in time with the tracks, i.e. they are accidental photons.

Vetoing all $K_{\pi\mu e}$ candidates with a photon fulfilling the conditions listed above, rejects 23% of the remaining events (Fig. 4.31).

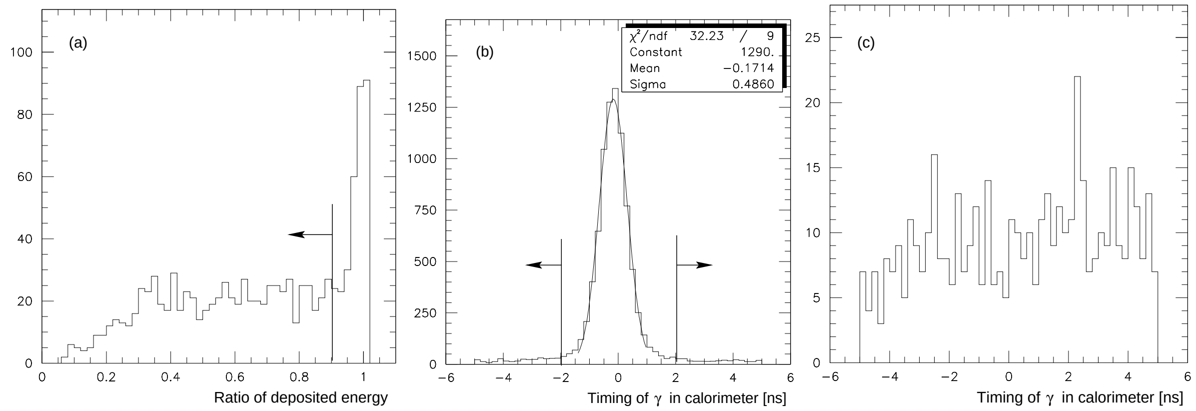

Figure 4.30: a) 2×2 divided by 4×4 ratio of the deposited energy in a clump. b) Timing of photons in the calorimeter. c) Timing of photons in calorimeter for events with no electron or positron track.

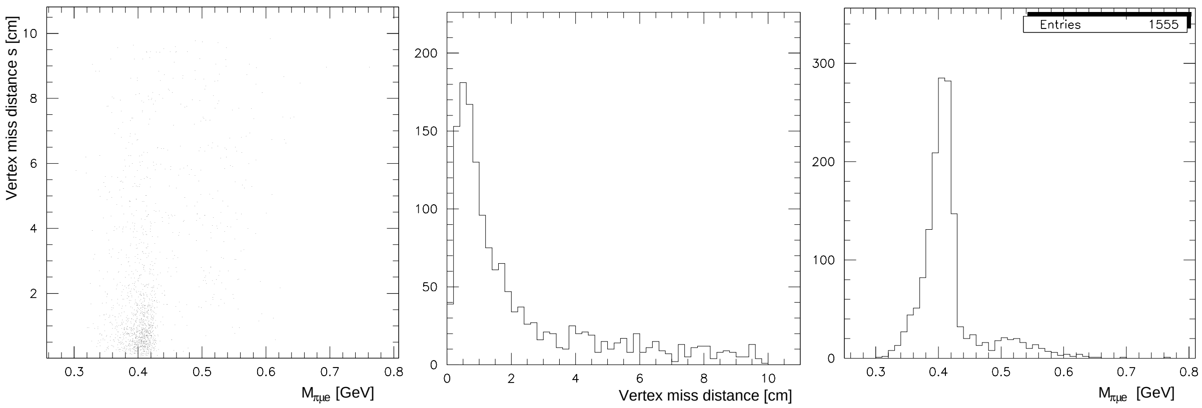

Figure 4.31: Vertex miss distance s vs. $M_{\pi\mu e}$ mass distribution after rejecting all events with an in-time photon.

4.6.10 Result of the search

At the conclusion of the previous cut, 1555 events remained in the vertex miss distance s versus $K_{\pi\mu e}$ invariant mass plot, the final step is to define the signal region.

Before we can do this, we have to remove a last obstacle. Figure 4.32 shows a strong linear dependency of the vertex miss distance s on the Z-position of the vertex, i.e. a cut directly on s would result in a loss of efficiency. Scaling s by

$$s_{NORM} = \frac{s}{0.333 - 0.00228 \times VTX_Z} \tag{4.23}$$

where VTX_Z denotes the Z-position of the vertex normalizes the s-distribution so that it becomes independent of the vertex position.

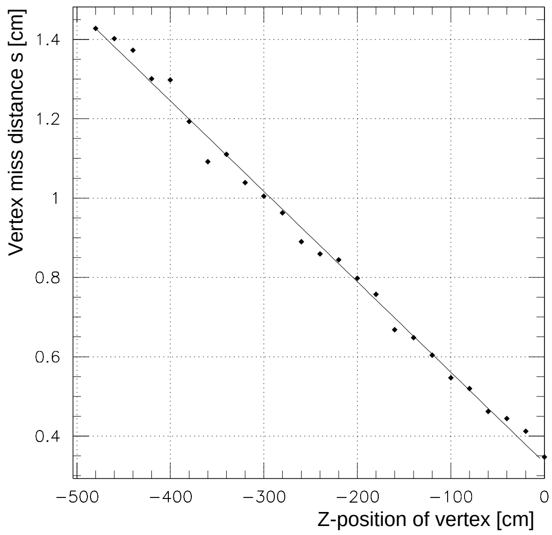

Figure 4.32: Mean value of the vertex miss distance s vs. Z-position of the vertex for K_τ events.

Because of the increase in the kinetic energy released in $K_{\pi\mu e}$ over that of K_τ we expect a slightly wider s_{NORM}-distribution for $K_{\pi\mu e}$. This is documented in Fig. 4.33a displaying the s_{NORM} for K_τ and $K_{\pi\mu e}$ Monte Carlo events. Fig. 4.33b compares s_{NORM} for simulated K_τ and data K_τ events, showing a nice agreement. Hence, we can directly scale from Monte-Carlo K_τ to Monte-Carlo $K_{\pi\mu e}$. With a cut at $s_{NORM} = 1.9$ cm, 95% of the good K_τ data events are kept. To also keep 95% of $K_{\pi\mu e}$ events, the cut has to be moved to $s_{NORM} = 2.1$ cm.

Also due to the increase in the kinetic energy, the width of the invariant mass distribution is expected to be wider for $K_{\pi\mu e}$ than for K_τ events. Fig. 4.34a displays the invariant mass for simulated $K_{\pi\mu e}$ and simulated K_τ events. One standard deviation (σ) for simulated K_τ events is 2.2 MeV, while it becomes 3.8 MeV for simulated $K_{\pi\mu e}$ events. Figure 4.34b compares the reconstructed invariant mass $M_{\pi\pi\pi}$ for data and simulation. The width in the data is slightly broader than in the simulation (~ 2.2 MeV for MC and ~ 2.3 MeV for data).

Figure 4.35 shows the final s_{NORM} vs. invariant mass distribution of the decay products for $K_{\pi\mu e}$. The signal region includes all events within $\pm 3\sigma = \pm 11.9$ MeV of the K^+ mass and with an s_{NORM} less than 2.1 cm. No events are found in the $K_{\pi\mu e}$ signal region. An equivalent plot for K_τ data events is shown for comparison in Fig. 4.36.

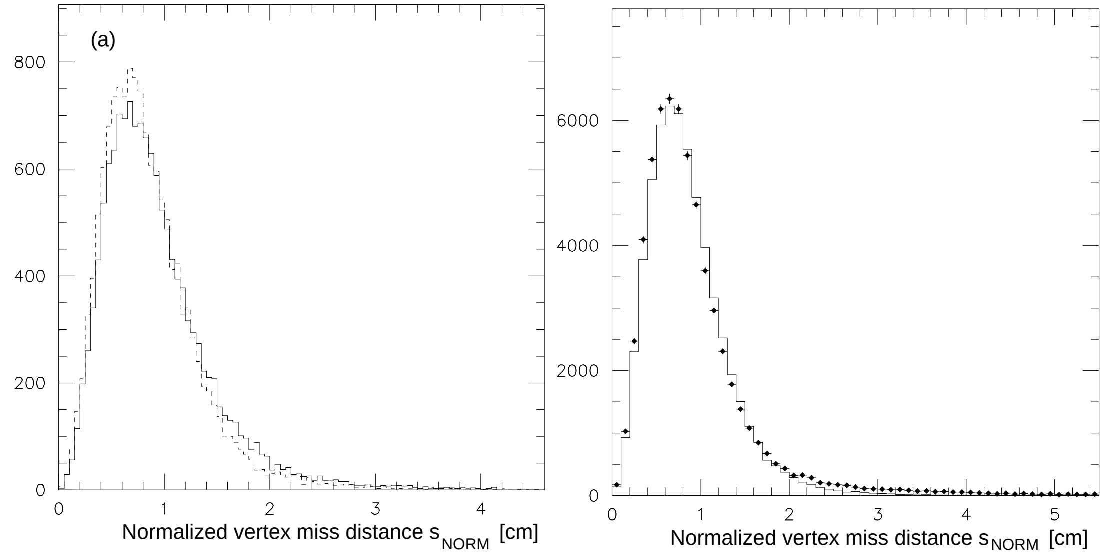

Figure 4.33: a) Reconstructed normalized vertex miss distance s_{NORM} for simulated $K_{\pi\mu e}$ (solid) and simulated K_{τ} (dashed) events. b) Normalized vertex miss distance s_{NORM} for MC (histogram) and data (error bars) K_{τ} events.

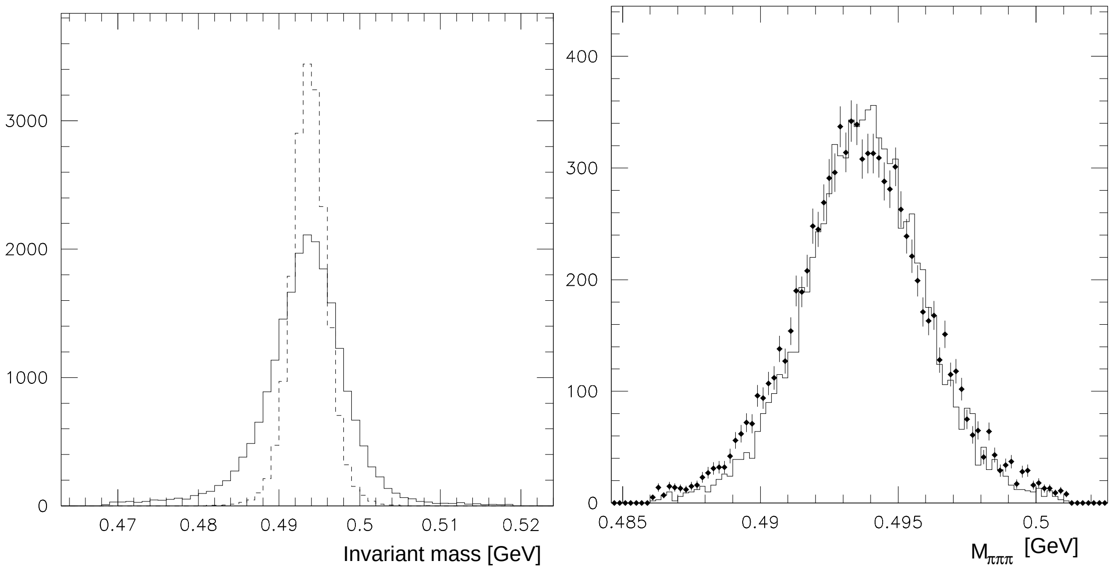

Figure 4.34: a) Reconstructed invariant mass for simulated $K_{\pi\mu e}$ solid and simulated K_{τ} (dashed) events. b) Invariant mass for MC (error bars) and data (histogram) K_{τ} events.

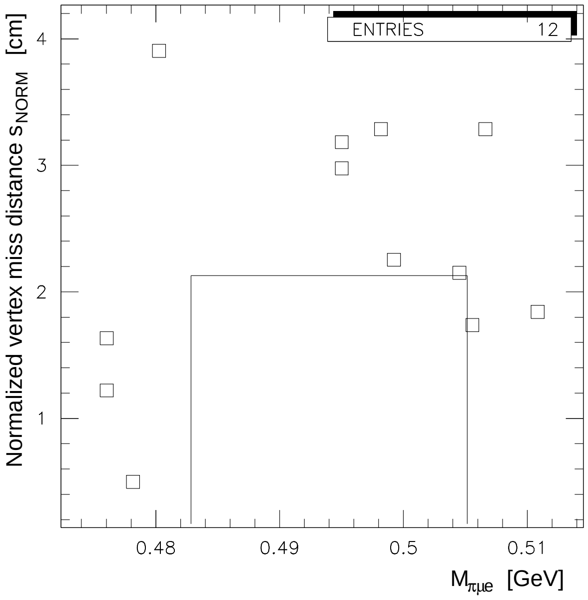

Figure 4.35: Final invariant mass $M_{\pi\mu e}$ vs. normalized vertex miss distance s_{NORM} scatter plot. The signal region is defined by $\pm 3\sigma$ on the $\pi\mu e$ mass, and the 95% point on s_{NORM}.

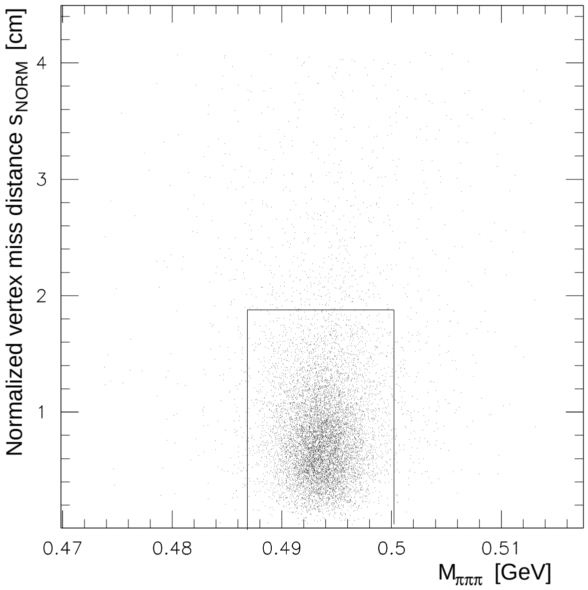

Figure 4.36: Final invariant mass $M_{\pi\pi\pi}$ vs. normalized vertex miss distance s_{NORM} scatter plot. The signal region is defined by $\pm 3\sigma = 6.9$ MeV on the $\pi\pi\pi$ mass, and the 95% point (1.9 cm) on s_{NORM}.

4.6.11 Discussion of $K_{\pi\mu e}$ candidates close to signal region

With the previous section, the end of the search is reached with a background free result. But there are a few events very close to the signal region, and it is well worth it to try to understand their origin. Figure 4.37 labels the seven events that will be examined in this chapter.

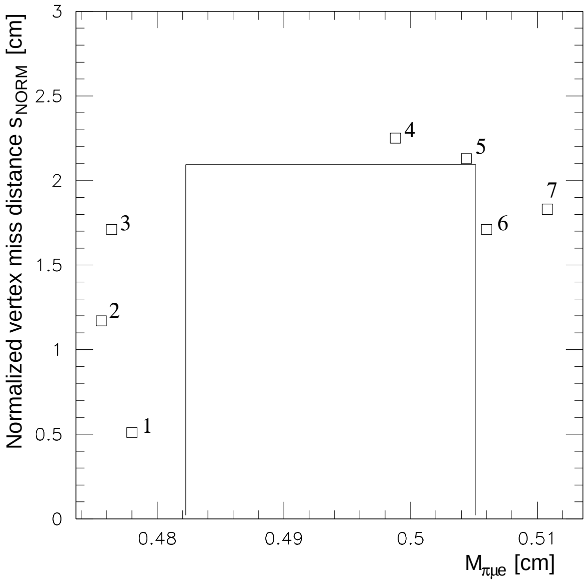

Figure 4.37: $K_{\pi\mu e}$ candidates that fall nearest to the signal region.

Event 1

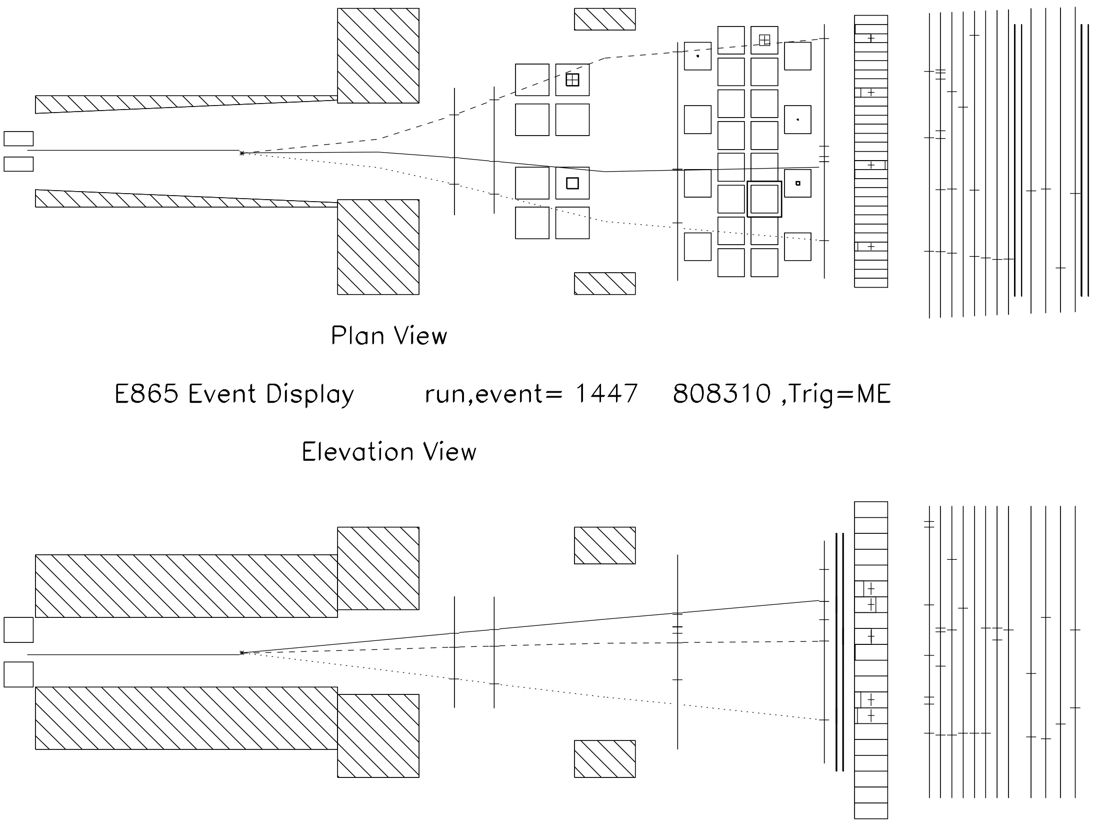

Figure 4.38: Event 1.

Fig. 4.38 shows the first event that lies close to the signal region in the E865 event display. We recognize on the beam left side the electron (dashed track) having in-time light (a TDC is indicated in the Čerenkov counters and also in the calorimeter by a cross, an ADC is given by a box with a size proportional to the deposited light) associated with it. The dotted track can be identified as a muon having a track, indicated by the ticks representing hits, in the muon stack. But the third track (solid), which should be a pion is in fact a positron. Its E/P is 0.67. There are early Čerenkov signals, at -19 ns in C1 and at -17 ns in C2, with large ADC's (2.0 photo electrons in C1 and 7.8 photoelectrons in C2). The electron and the positron have together a mass $M_{ee} = 0.091$ MeV. This event is likely to be a Dalitz decay, where the Čerenkov TDC's are blocked by an early hit.

Event 2

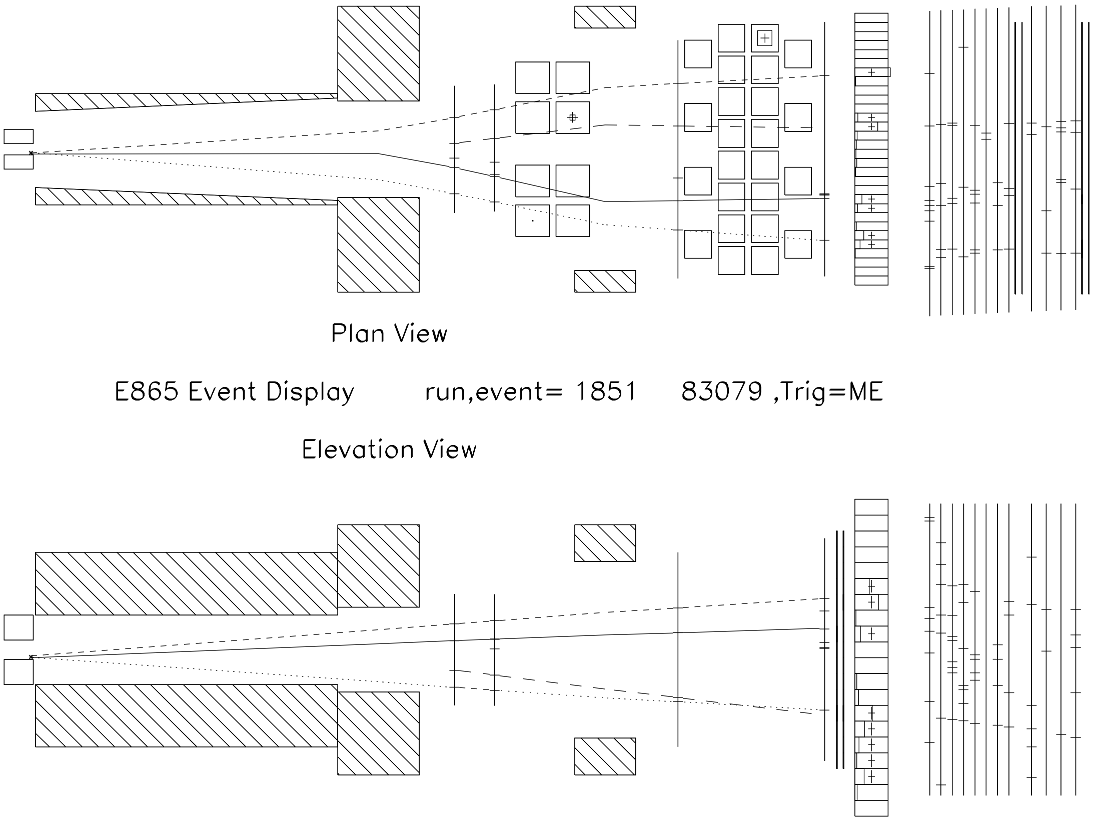

Figure 4.39: Event 2.

Event 2 has a normalized vertex miss distance s_{NORM} of 1.2 cm, a target likelihood of -15.4 and a tight timing ($TRMS$ = 0.42 nsec). Furthermore, the vertex is located at $Z = 460$ cm. It is very improbable that the electron (dashed) is misidentified, it produced 0.94 P.E. in C1, 3.28 P.E. in C2 and has $E/P = 1.02$ assigned to it. There is also a clear muon with good particle identification: 75 % of the expected hits are found, the deviations at the B-counter and C-counter are 1.28 σ_B and 1.72 σ_C, respectively. This event is most likely a K_τ, where the π^- decayed into an electron and a neutrino and one of the π^+ into a muon and a neutrino.

The fourth track in this event (long dashes) is an accidental, combining it with the two positively charged tracks gives a vertex miss distance s of 20 cm.

Event 3

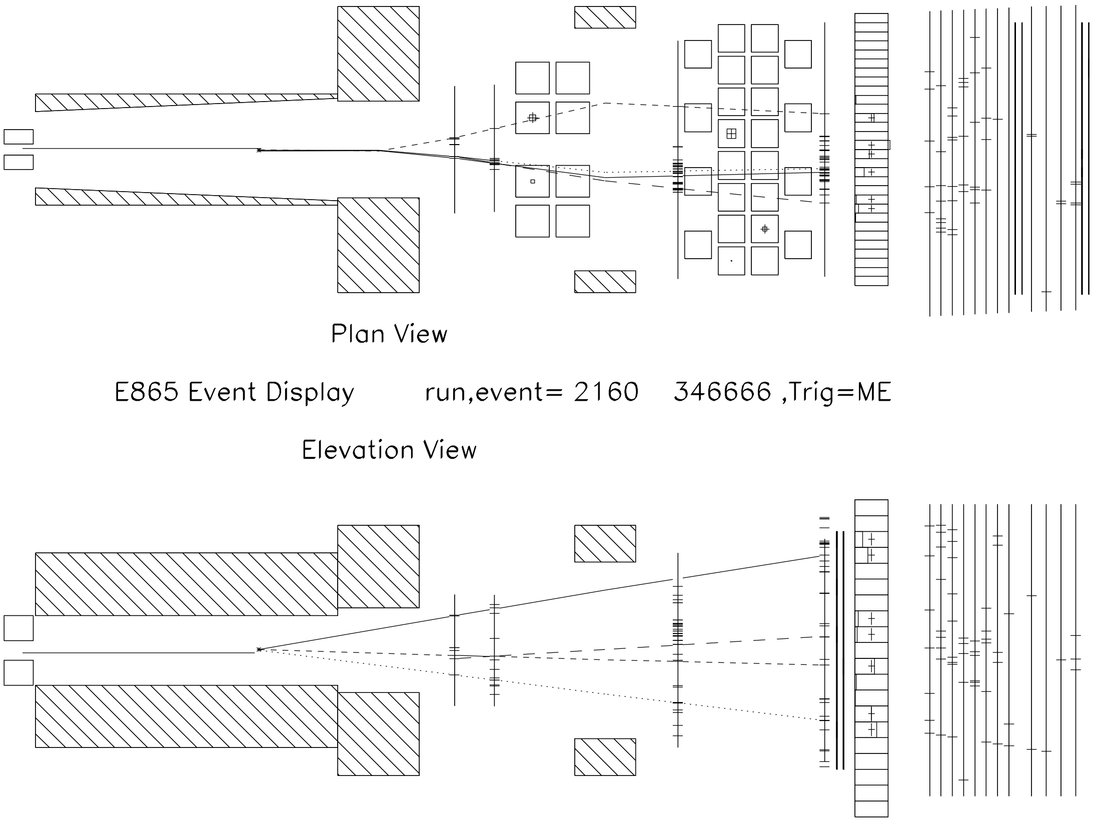

Figure 4.40: Event 3.

Event 3 has a huge combinatoric background in the MWPC's P2, P3 and P4. Most of the space points found are not physical, they are built because partly all channels in certain PCOS4 cards fired. The muon and the pion track are found due to such background. This is also indicated by a fairly bad track quality, namely $\chi^2 = 4.2$ for the muon and $\chi^2 = 6.7$ for the pion. This event is not a K^+ decay.

Event 4

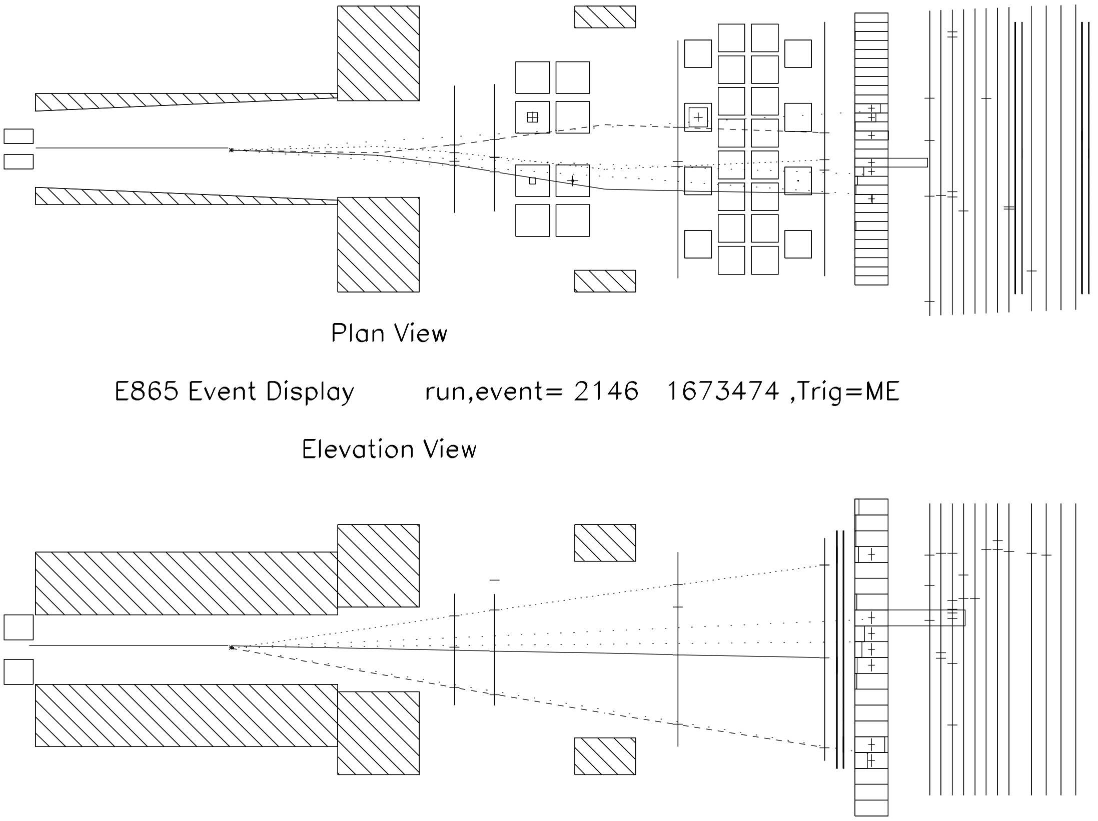

Figure 4.41: Event 4.

We believe that event 4 is in reality a mismeasured K_{DAL}, there are several indications that the pion is in fact a positron. This track has 1.4 P.E. in C1 assigned to it. It also hits the calorimeter just next to the beam hole, there might be significant leakage. Additionally, requiring the cuts listed in section 4.5, three photons are found (dotted tracks with large spacing between the dots). Two of them fail the Pass3 photon veto because they are just out of time (2.2 ns and -2.9 ns) and the third would be in-time, but it has a ratio of the deposited energy in 2×2 modules divided by the deposited energy in 4×4 modules of 0.89.

Event 5

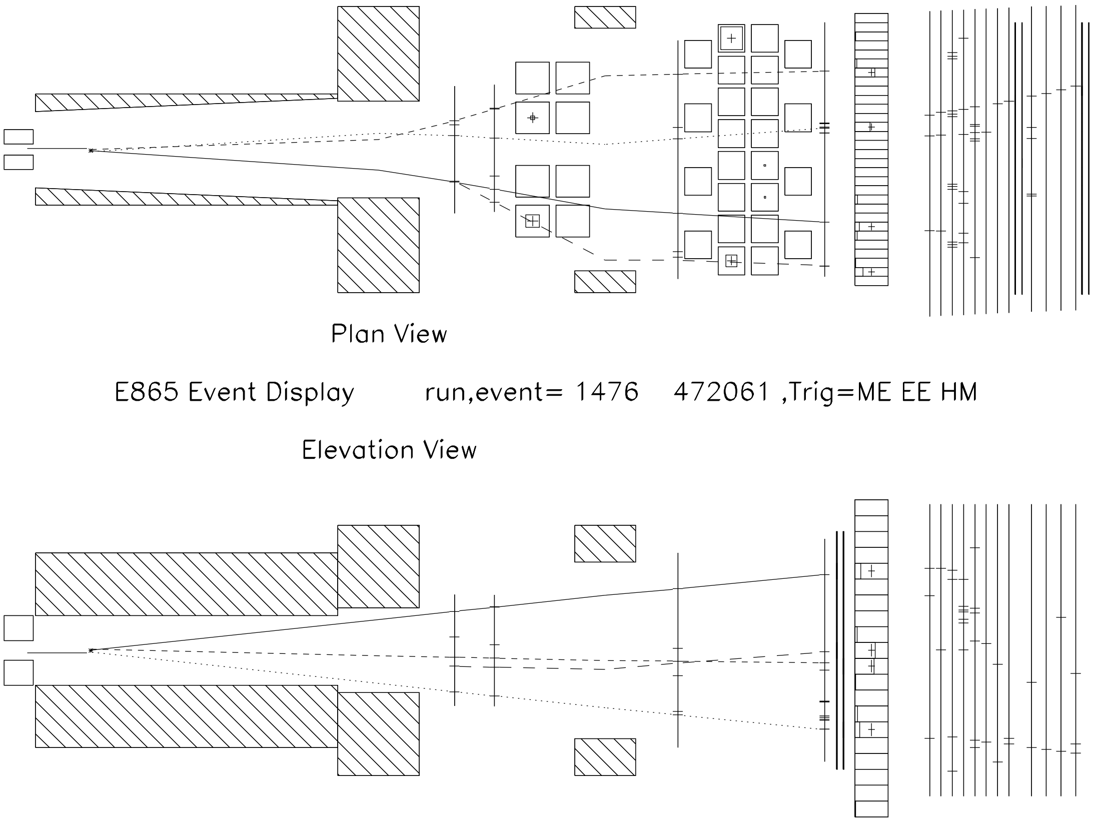

Figure 4.42: Event 5.

Event 5 has an additional fourth track (long dashes) that can be clearly identified to be a positron (2.4 P.E. in C1, 2.5 P.E. in C2 and $E/P = 0.94$). Furthermore, this track together with the electron yields a mass $M_{ee} = 16$ MeV. The normalized vertex miss distance is calculated to be below 4 cm if the 'e^+e^--pair' is combined with either the pion or the muon. This event is most likely a badly mismeasured K_{DAL}.

Event 6

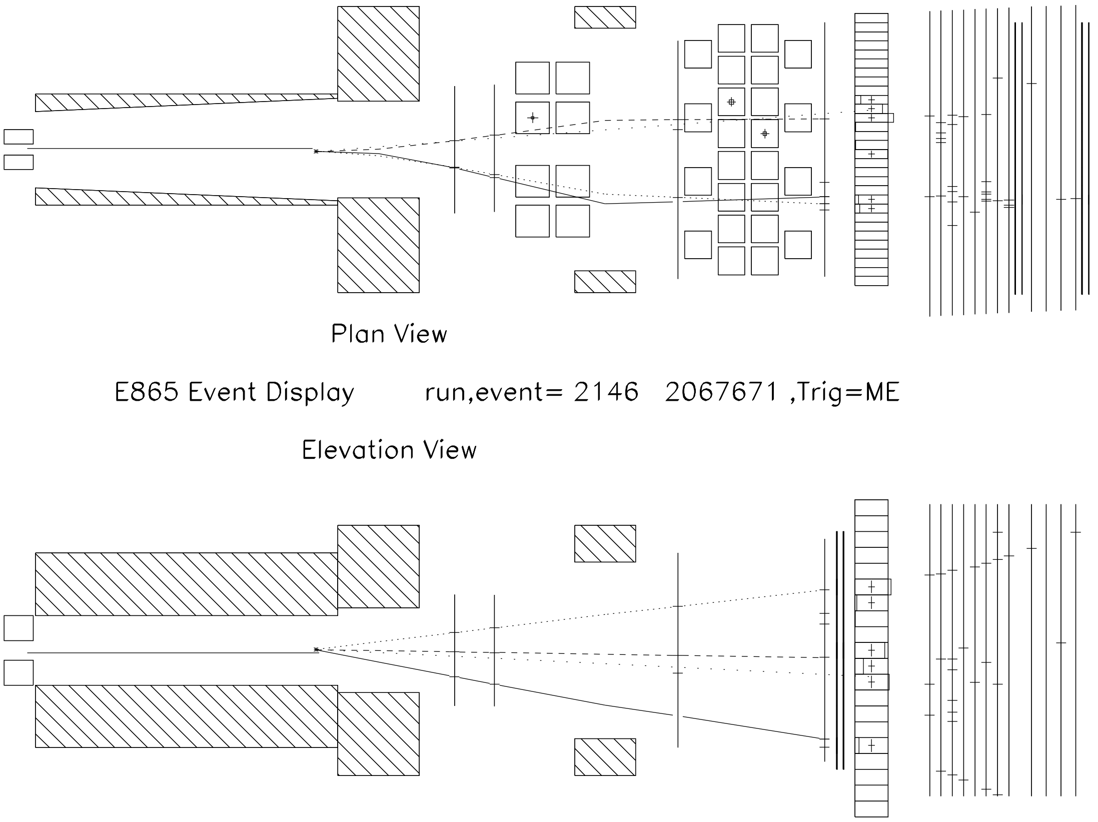

Figure 4.43: Event 6.

Event 6 is the most intriguing. It has a tight timing ($TRMS = 0.41$ nsec), s_{NORM} is low and it also has a good target likelihood (-12.6). The particle identification on the muon and electron track is good, and there is also no background in the MWPC's. But the pion has a clear track in the muon stack that goes out of bound just before it hits the B-counter. This track has a high probability to be a muon.

Event 7

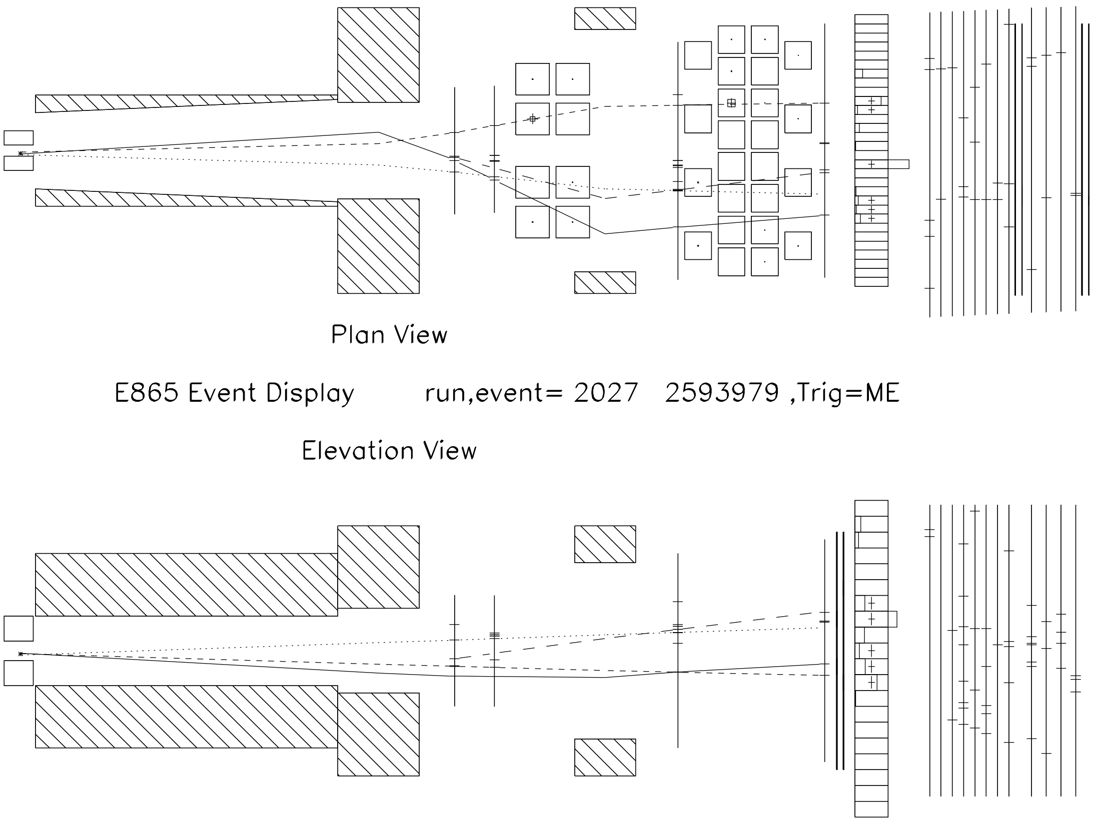

Figure 4.44: Event 7.

We believe that event 7 is an accidental. Its timing is just barely acceptable ($TRMS =$ 1.14 ns) and the vertex is located at -475 cm. Furthermore, the momentum of the muon is 3.5 GeV which is typical for beam muons.

4.6.12 Summary of Pass3 analysis

Table 4.6 summarizes the the Pass3 cuts for $K_{\pi\mu e}$, K_{DAL} and K_{τ}. Additional cuts, used to find space points, tracks, etc. are listed in Appendix A.

For the normalization channel K_{DAL}, no target likelihood cut is applied, since the K^+ reconstruction is incomplete for such events due to the missing photon. Also no restriction on the number of tracks and, obviously, no photon veto is used. There is no physical reason why we do not cut on the number of tracks in K_{DAL}, omitting this constraint only simplifies the normalization. Finally, the reconstructed invariant mass $\mathrm{M}_{\pi ee}$ of the K_{DAL} events is required to be at least 380 MeV. This cut is motivated by the fact that the K_{DAL}

	$K_{\pi\mu e}$	K_{DAL}	K_τ
Timing	TRMS$< \sqrt{1.5}$ sec	$TRMS < \sqrt{1.5}$ sec	$TRMS < \sqrt{1.5}$ sec
χ^2 of momentum fit	$\chi^2 < 20$	$\chi^2 < 20$	$\chi^2 < 20$
Target likelihood	TGLK > -17	—	TGLK > -17
Decay volume	$\mathrm{Z_{vertex}} > -490$ cm	$\mathrm{Z_{vertex}} > -490$ cm	$\mathrm{Z_{vertex}} > -490$ cm
Čerenkov counters	comb. ineff $< 1\%$	—	—
Particle ID	$\pi\mu e$	$ee\pi$	$\pi\pi\pi$
Max. tracks	4	—	—
π on left	$\surd$	—	—
M_{ee} mass	< 50 MeV	> 50 MeV	—
Photon veto	$\surd$	—	—
K^+ mass	± 11.9 MeV	> 380 MeV	± 6.9 MeV
s_{NORM}	< 2.1 cm	< 4.0 cm	< 1.9 cm

Table 4.6: Summary of the Pass3 cuts applied to $K_{\pi\mu e}$ candidates and K_{DAL} and K_τ events.

sample is contaminated by decays like $K^+ \to \pi^0\mu^+\nu$ followed by $\pi^0 \to e^+e^-\gamma$, $(K_{\mu 3})_{DAL}$, $K^+ \to \pi^0 e^+\nu$ with $\pi^0 \to e^+e^-\gamma$, $(K_{e3})_{DAL}$ and $K^+ \to \pi^+\pi^0\pi^0$ with $\pi^0 \to e^+e^-\gamma$ and $\pi^0 \to \gamma\gamma$, $(K_{\tau'})_{DAL}$. These decays tend to have a low mass $\mathrm{M}_{\pi ee}$ as shown in Fig. 4.45. The cut, however, is somehow arbitrary and it remains to be proven that it does not affect the $K_{\pi\mu e}$ branching ratio.

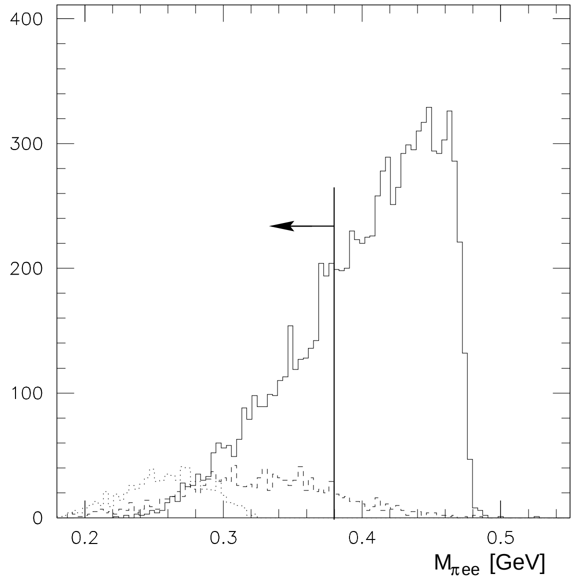

Figure 4.45: $M_{\pi ee}$ mass distribution for simulated K_{DAL} (solid), simulated $(K_{\mu3})_{DAL}$ (dashed) and simulated $(K_{\tau'})_{DAL}$ (dotted) events.

Chapter 5

Monte Carlo simulations

5.1 Overview

The interactions of the beam particles and the decay products with the apparatus are simulated by the program KAY [70] based on the GEANT3 [71] software package, provided by CERN. It sets up the initial particle and tracks it to a randomly chosen decay point. The daughter particles are then tracked through a simulated E865 detector, and information about positions, momenta, energy loss, etc. in the individual detector elements are stored in memory. This information is then digitized, i.e. the ADC values have to be calculated from the deposited energy, positions in the wire chambers have to be converted into wire numbers, and (local) inefficiencies have to be taken into account. Finally, the calculated response is combined to an event in the standard format, so it can be read and analyzed by the same programs used to analyze real data.

5.2 The initial particle

The definition of the initial kinematics of the event turns out to be tricky. Although the beam line is implemented in the geometry, it does not make a lot of sense to set up the initial particle at the target and to trace it through the beam line each time, since this part of the simulation is identical for all K^+-decays. A better solution is to produce an array of five beam parameter (X, Θ_X, Y, Θ_Y and P) at the exit of the last quadrupole magnet in the beam line, as is necessary to fully describe the initial kinematics of a kaon. Two beam simulations are available to generate this array: GEANT itself and the program BETRAF [72]. Figure 5.1 compares the parameters for reconstructed simulated K_τ decays with those of reconstructed data K_τ decays. The agreement is fairly limited, except for the Y-position, where it is good. This is somewhat expected since our knowledge of field magnitudes and relative positions of the beam line magnets is not accurate enough.

There are two major concerns if these simulated distributions are to be used: First, we would have to check how such discrepancies affect the geometrical acceptance and second, there are regions of limited efficiency in some of the detector parts, using a simulated distribution, these regions would be at the wrong positions. To avoid such difficulties, we decided to use reconstructed K_τ data to simulate the beam parameters.

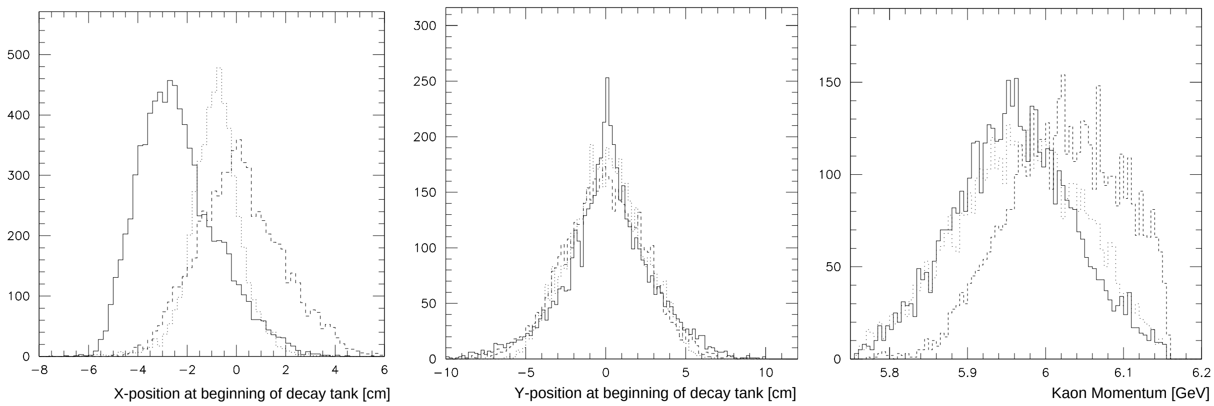

Figure 5.1: X-position, Y-position and momentum at the beginning of the decay tank for data K_τ kaons (solid lines) compared with reconstructed Monte Carlo kaons where BETRAF (dashed) or GEANT (dotted) is used to generate the beam parameters.

5.3 Decay mechanisms

The life time and branching ratios of the six most common decay modes of all 'basic' particles are stored in GEANT. In its default version the decay points are chosen according to an appropriate exponential distribution for one of the decay modes stored. This procedure is not well suited for a study of rare decays. We always want the kaon to decay at certain positions in the apparatus and into the same rare mode. Since it is possible in GEANT to define additional particles, we define a new kaon, which is forced to undergo a certain decay within a defined volume. Lastly, appropriate matrix elements can be used to assign momenta to each of the decay products.

K_τ and also $K_{\pi\mu e}$ decays are simulated with an approximately uniform angular distribution of the decay products in the K^+ center of mass system. The decay products are only required to conserve energy and momentum. Finally, they are boosted into the lab frame. The simulation of K_{DAL} decays is more involved. First the momenta for the decay products of the two body decay $K^+ \to \pi^+\pi^0$ have to be calculated. They are simulated with an isotropic distribution in the K^+ center of mass system. Then the π^0 is forced to decay into an e^+e^- pair and a photon. The dynamical dependence of the differential decay rate of $\pi^0 \to e^+e^-\gamma$ can be written in lowest order as [73]:

$$\frac{d^2\Gamma}{dxdy} \sim \frac{(1-x)^3}{x}(1+y^2+\frac{r^2}{x}) \equiv G(x,y) \tag{5.1}$$

Integration over y yields:

$$\frac{d\Gamma}{dx} \sim \frac{(1-x)^3}{x}\beta(1+\frac{r^2}{x}) \equiv F(x) \tag{5.2}$$

where x is the invariant mass squared of the Dalitz pair in units of m_π^2:

$$x = \frac{(q_1+q_2)^2}{m_\pi^2} \tag{5.3}$$

The variable y is defined as:

$$y = \frac{2p(q_1-q_2)}{m_\pi^2(1-x)} \tag{5.4}$$

where p, q_1, q_2 are the four momenta of the pion, the positron and the electron and

$$r = \frac{4m_e^2}{m_\pi^2} \tag{5.5}$$

To impress this form on the generated decays, a value of x between the limits $4m_e^2/m_\pi^2$ and 1 according to the distribution function 5.2 is randomly selected. Knowing now the mass of the virtual photon, a set of momenta and energies for the decay $\pi^0 \to \gamma\gamma^* \to e^+e^-\gamma$ is generated with an isotropic angular distribution of the decay products in the π^0-CM system. This also fixes the variable y. Since $y = \beta\cos(\Theta)$, where Θ is the angle of the pion with respect to one of the electrons, y has a flat distribution in phase space, and can be picked using the acceptance/rejection Monte Carlo technique, i.e. only events are accepted satisfying the condition:

$$RN \leq \frac{G(x,y)}{G(x,y_{max})} \tag{5.6}$$

where RN is a randomly generated number between 0 and 1, and $y_{max} = \beta = \sqrt{1-r^2/x}$ is the maximum value of y. Radiative corrections to equation 5.2 can be expressed by

$$\frac{d^2\Gamma^{rad}}{dxdy} = \delta(x,y)\frac{d^2\Gamma}{dxdy} \tag{5.7}$$

The correction factors $\delta(x, y)$ are tabulated [73]. This allows to use the acceptance/rejection Monte Carlo technique again by requiring:

$$RN \leq \frac{1 + \delta(x, y)}{1 + \delta_{max}} \tag{5.8}$$

where δ_{max} is the maximum value in the table. In 5.2 we also neglected the form factor of the π^0. The form factor is generally expected [74] to vary slowly in the available energy range and is therefore approximated by $f(x) = 1 + ax$, where the particle data book [75] lists $a = 0.032$. An acceptance/rejection Monte Carlo technique is used again by requiring:

$$RN \leq \frac{f(x)^2}{f_{max}^2} = \frac{(1 + ax)^2}{(1 + a)^2} \tag{5.9}$$

5.4 Simulation of the physical processes within the apparatus

GEANT allows to describe the experimental apparatus by specifying a set of volumes. Each volume is characterized by a shape, a medium describing the material which fills the volume, the tracking precision of particles crossing the volume and the presence or absence of a magnetic field. A volume can be positioned inside another volume, where the properties of the inserted volume ('daughter volume') replace the properties of the original volume ('mother volume'), resulting in a geometrical tree structure. The positions are read in from a data file, also used for the offline analysis. To simulate the magnetic field present in the detector, the actual field map of the spectrometer magnets is used.

GEANT steps the generated particles through the geometry with the selected tracking precision simulating the interactions of the particles with the material. The simulated processes are:

- Hadronic interactions, using the GHEISHA hadron shower Monte Carlo.
- Multiple scattering according Molière theory.
- Electromagnetic processes like energy loss due to ionization, bremsstrahlung, annihilation and generation of Čerenkov light for charged particles and photoelectric effect, Compton scattering and pair production for photons.

For additional information about the simulation of the physics processes be refer to [71].

Each particle can be constrained to cross or not to cross certain volumes in the geometry setup. If the particle fails to fulfill such a condition, the event immediately gets aborted. This allows to make sure that only events are kept where all daughter particles remain within the active area of the detector, i.e. only events that can be fully reconstructed. This feature also saves a lot of computer time during the generation of the Monte Carlo events. For instance, typically about 10% of the events get accepted by requiring all daughter particles to hit the A-counter. Aborting the generation of the event as soon as a daughter particle fails to hit the A-counter saves more than 50% of CPU time.

5.5 Digitization of the simulated events

At the end of the tracking phase, information about the position of penetration, momentum, energy loss, particle ID, time and number of generated Čerenkov photons in the individual detector elements is stored in a ZEBRA [76] bank for each track. This information has to be digitized, i.e. the response of a given detector has to be simulated, and written to E865 data format, so that it can be read and analyzed by the same programs used to analyze real data.

It is almost impossible to consider each effect affecting the digitization, hence certain simplifying assumptions are made to reduce the CPU usage and also the programming work:

MWPC

There are a few effects that need to be considered: chamber efficiency, local inefficiencies caused by electrically disconnected wires, cluster size and gate width.

- The chamber efficiency varied slightly during the run. It is affected by small changes in the gas mixture and by the voltage difference maintained in the MWPC, which also changes from plane to plane. To account for this, spatially uniform chamber efficiencies for the beam left and the beam right side of each wire plane for different periods of the run, determined using K_τ data, are read from a data file.
- The local inefficiencies also changed during the run, hence dead wires are stored in a file as a function of different run periods.
- The cluster size is a function of the slope of the track, the chamber operation voltage, amplifier threshold, etc. To calculate the cluster size only geometrical factors are considered, while all other parameters are neglected, i.e. all wires in the drift region of the primary electrons are assigned.
- All hits are assumed to be within the time gate.

Čerenkov counters

The single most important aspect of the simulation is how many of the the generated Čerenkov photons will be detected by a photomultiplier tube. Two different approaches are available. The first one traces the photons through the mirror geometry, assuming a mirror reflectivity and a PMT quantum efficiency appropriately dependent on the photon energy. The resulting number of photons is then smeared to simulate the statistical nature of the electron multiplication in the PMT-dynodes. This approach will not be used in this thesis. The second one, the one which will be used, is based on the counter efficiency ϵ as a function of the position and the slope of the track in X and Y. The mean number of created photoelectrons is then given by $-\log(1-\epsilon)$, provided that the particle crossing the Čerenkov counter is above the threshold for Čerenkov radiation. To take into account that the created number of photoelectron in the counter is a priori a discrete number, we pick one randomly from a Poisson distribution with a mean given by the number of photoelectrons calculated above. This discrete number finally gets smeared by a Gaussian with a σ resulting from the jitter of the pedestal and the jitter of the gain at the first dynode. For electrons and positrons the number of generated photons does not depend significantly on the momentum. For non-electrons and particles which are created in the counters and hence have a shorter track, the number of photoelectrons is scaled down by the number of photons generated in GEANT for this track divided by the average number of photons for electrons in this side of the counter. No attempt is made to simulate the timing distribution. A perfectly timed TDC hit is assigned to each ADC hit.

Electromagnetic calorimeter

The response of the calorimeter depends on the scintillator, the wavelength shifting fibres, the photomultiplier tube and the position of the hit in the module. The light output of the scintillator is a function of its ability to convert ionization energy to photons. This quantity determines the resolution of the scintillator. A semi-empirical model is known as Birks' law [77, 78]:

$$\frac{dL}{dx} = A\frac{dE}{dx}\left[1 + B\frac{dE}{dx} + C\left(\frac{dE}{dx}\right)^2\right]^{-1} \tag{5.10}$$

where $\frac{dL}{dx}$ is the light emitted per unit path length and A the scintillation efficiency. The parameters B and C are quoted in [79] for Pilot-B, which is used to model the scintillator of the calorimeter. This light is then conducted to the PMT via the fibres. For this transport, the absorption length in the fibres has to be taken into account, since the exponential loss of light affects the constant term in the energy resolution. The couplings of the fibres to the scintillator and to the PMT are assumed to be linear. To simulate the photoelectron statistics in the PMT dynodes the light yield is smeared by [65]:

$$\sigma/E = \frac{1}{\sqrt{2000 \times E(GeV)}} \tag{5.11}$$

Finally, to take into account the jitter of the pedestal, etc. the energy deposited in each module is smeared with a Gaussian centered at 0 mean and a width $\sigma = 25$ MeV. Concerning the timing, again a perfectly timed TDC hit is assigned to each ADC hit.

Muon chambers

Spatially uniform efficiencies for the beam left and beam right sides of the X- and Y-planes of each muon chamber, obtained using beam muons, are read from a file. No local inefficiencies are taken into account and all hits are assumed to be in-time.

Trigger

Up to a certain limit, the trigger can be simulated using the conditions mentioned in chapter 5.4. No further refinements are made, but crucial parts of the trigger, e.g. trigger conditions requiring an appropriate hit pattern, are simulated during the reconstruction of the event in the offline analysis.

Monte Carlo data block

Finally, a Monte Carlo data block is added to the event, intended to be used as a check of the offline reconstruction of the event. It contains information, together with the particle ID for each daughter particle of the decaying kaon, about the position of the track in the MWPC, the number of generated photoelectrons in the Čerenkov counters and the energy deposited in the calorimeter.

It also contains the weight assigned to each event. As it is explained in chapter 5.3, particles can be forced to decay within a certain length. A weight for each event is calculated to take into account this restricted decay range. This is essential to speed up the generation, especially of background events, since it allows to force the daughter particles to decay within certain positions.

5.6 Comparison with data

By far the most effective way of assessing the accuracy of the Monte Carlo simulation is to compare the generated decays with real data. We will present the comparison for K_τ and K_{DAL} in the next two sections.

5.6.1 K_τ comparison

K_τ events are a useful diagnostic tool since there are no missing neutral particles involved in this decay, i.e. the kaon properties can be completely reconstructed. K_τ is also the dominant decay of the K^+ with three charged particles in the final state making it easy to collect a clean data sample.

In all plots described below, the histogram represents reconstructed Monte Carlo (MC) events while the markers with the error bars show the distribution for reconstructed data events. All plots are based on Pass3 analysis.

Figures 5.2, 5.3 and 5.4 show the distribution of kaon momenta, the vertex position and the momenta of the daughter particles. The agreement between data and simulation is satisfactory. The target likelihood (Fig. 5.5) shows poor agreement, which is expected. The reasons for this are easy to understand. In section 5.2 the definition of the initial kinematics of the event is described. The use of beam parameters from reconstructed K_τ decays most closely resembles the actual experimental kaon beam. Now, when the kaon for the MC events is reconstructed, the experimental resolution is imposed twice, once in the K_τ reconstruction that produced the kinematics of the initial particles in the MC and once again in the MC reconstruction. As expected, this results in a broader resolution for MC than for data kaons. The disagreement in the χ^2 distribution (Fig. 5.6) is mainly due to our imperfect knowledge of the magnetic field of the spectrometer magnets. Finally, for reasons of completeness, we show the comparison for the normalized vertex miss distance and the $\pi\pi\pi$ invariant mass again (Fig. 5.7).

5.6.2 K_{DAL} comparison

In section 4.6.12 we found that the decays $(K_{\mu3})_{DAL}$ and $(K_{\tau'})_{DAL}$ also contribute to the K_{DAL} data sample. To minimize such contributions, a cut was placed on the invariant mass $\mathrm{M}_{\pi ee}$. Figure 5.8 shows $\mathrm{M}_{\pi ee}$-distributions for various decay modes. The K_{DAL}, $(K_{\mu3})_{DAL}$ and $(K_{\tau'})_{DAL}$ events are weighted with their branching ratio and acceptance. We recognize that the weighted sum of all three contributions match the data fairly well. This gives us confidence that the mass scales for MC and data are the same. In what follows, K_{DAL}will refer to a weighted sum of the different contributions and the $\mathrm{M}_{\pi ee} > 0.38$ GeV cut will be applied.

The simulation is good for the Z-position of the vertex (Fig. 5.9) and the mass M_{ee} (Fig. 5.10). K_{DAL} decays are also extremely useful in testing the particle identification. Figures 5.11 through Fig. 5.13 compare the response of the Čerenkov counters and the shower counter. In general, the agreement is satisfactory indicating the absence of any serious unaccounted systematic effects.

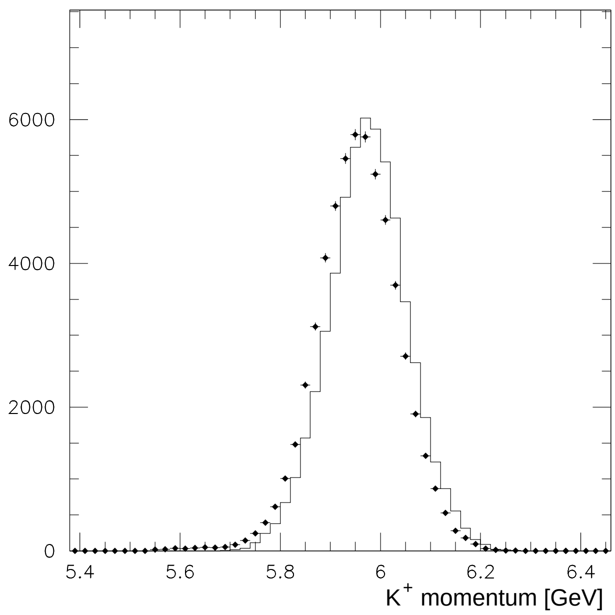

Figure 5.2: Momentum of the reconstructed kaon for MC (histogram) and data (marker) K_τ events.

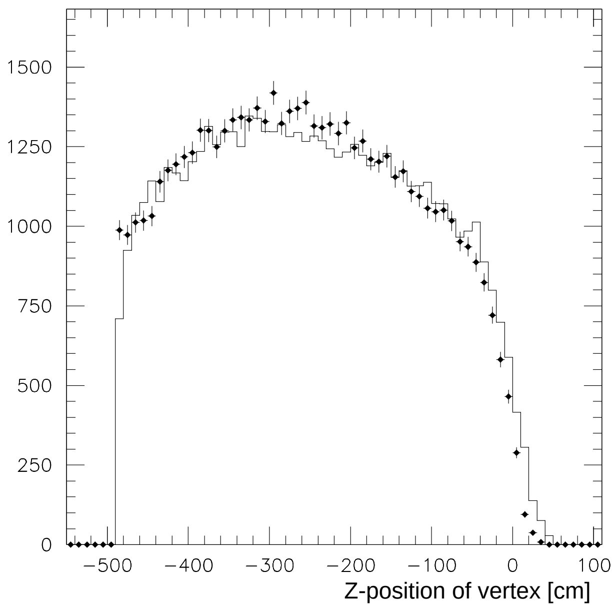

Figure 5.3: Distribution of the vertex position for reconstructed MC (histogram) and data (marker) K_τ events.

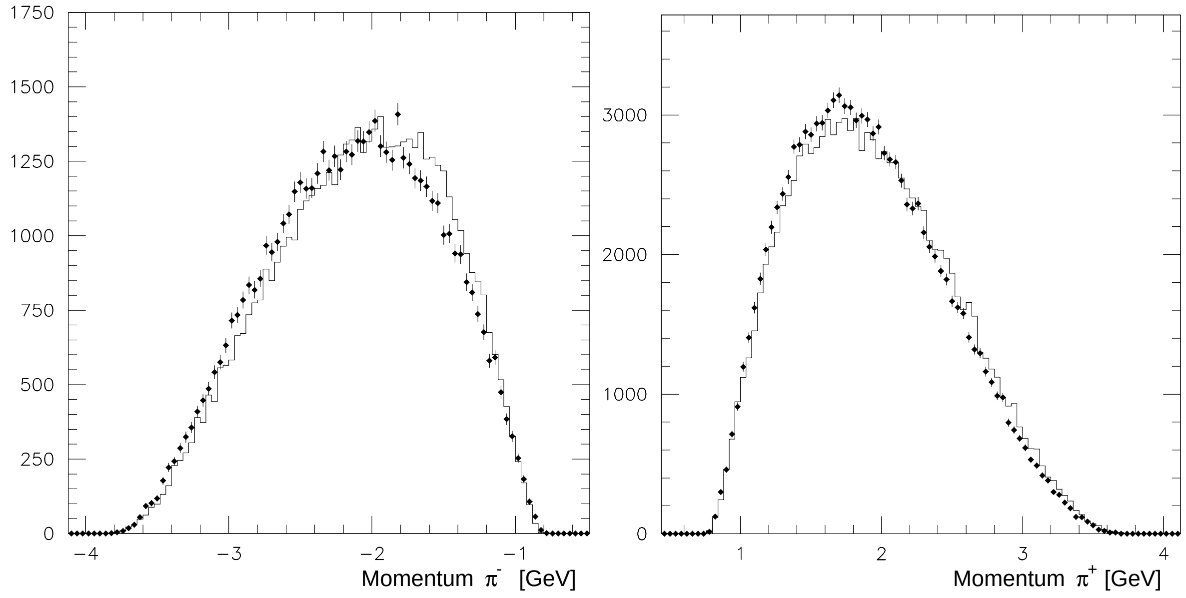

Figure 5.4: Momentum spectra of the π^+ and the π^- for MC (histogram) and data (marker) K_τ events.

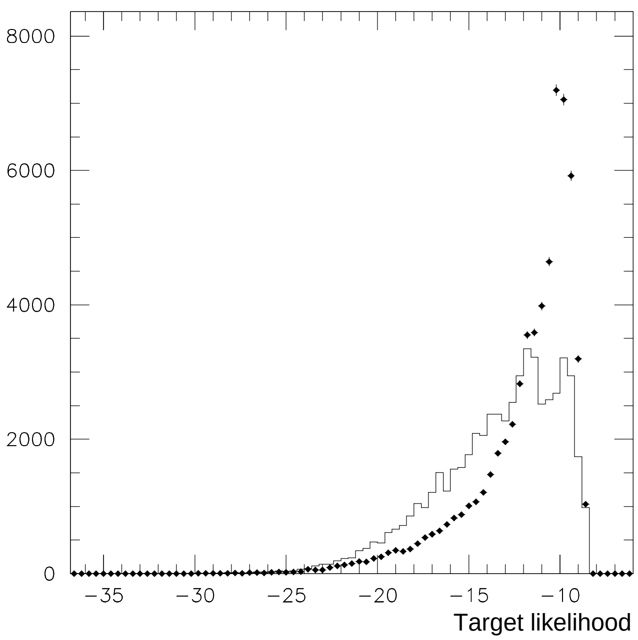

Figure 5.5: Target likelihood distribution for MC (histogram) and data (marker) K_τ events.

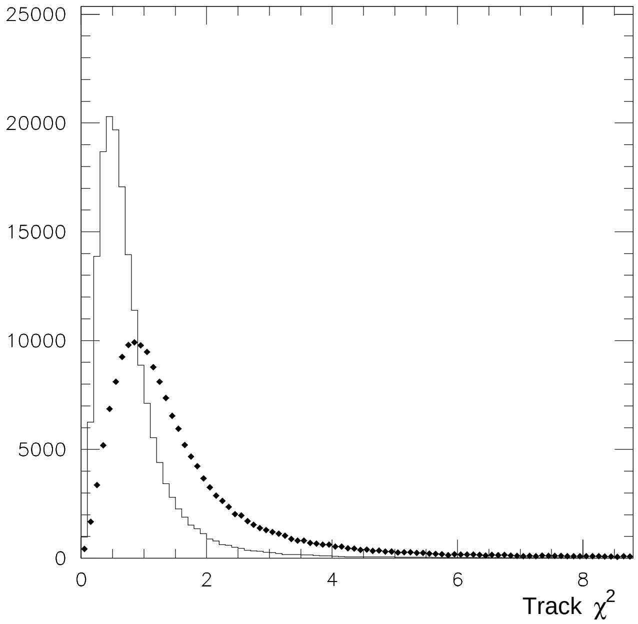

Figure 5.6: Track χ^2 distribution for MC (histogram) and data (marker) K_τ events.

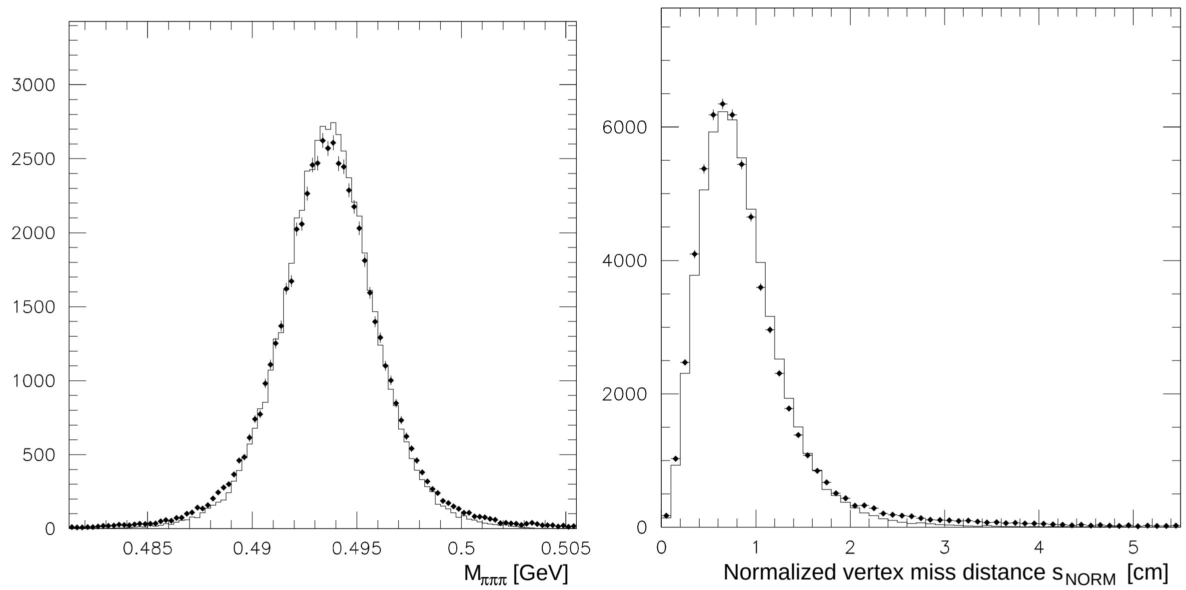

Figure 5.7: $M_{\pi\pi\pi}$ invariant mass and normalized vertex miss distance s_{NORM} for MC (histogram) and data (marker) K_τ events.

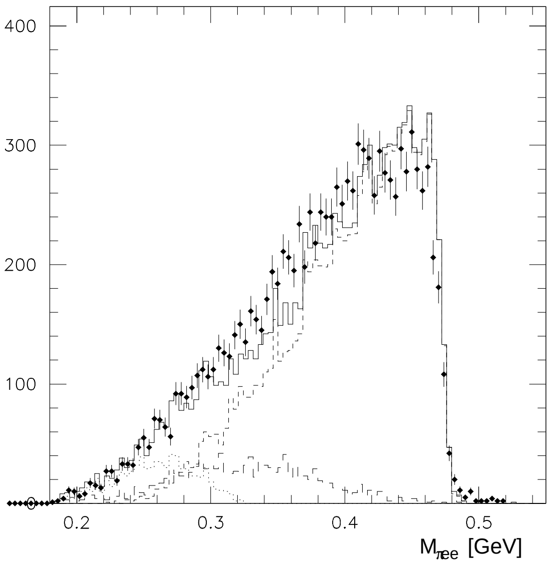

Figure 5.8: $M_{\pi ee}$ mass spectrum for MC K_{DAL} (dashed), MC $(K_{\mu 3})_{DAL}$ (long dashes), MC $(K_{\tau'})_{DAL}$ (dotted) and the sum of all three channels (solid) compared with the $M_{\pi ee}$ mass spectrum for data events (marker).

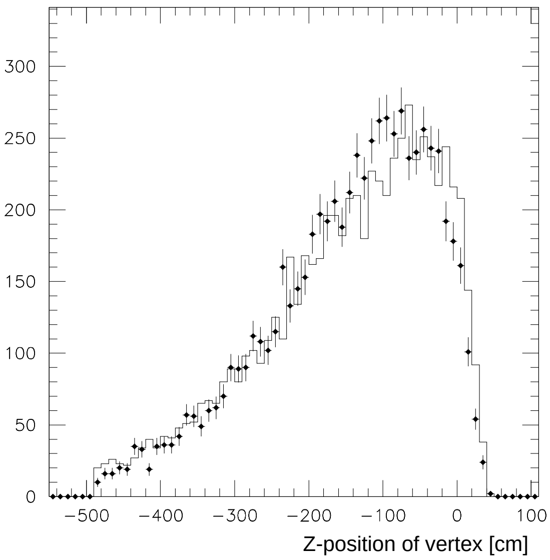

Figure 5.9: Vertex position for MC (histogram) and data (marker) K_{DAL} events.

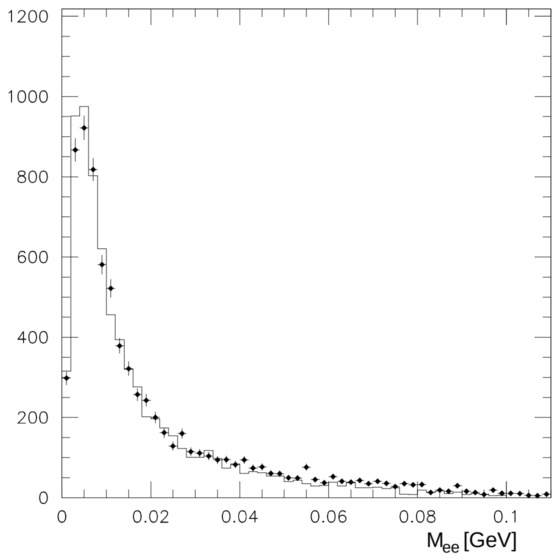

Figure 5.10: M_{ee} mass for MC (histogram) and data (marker) K_{DAL} events.

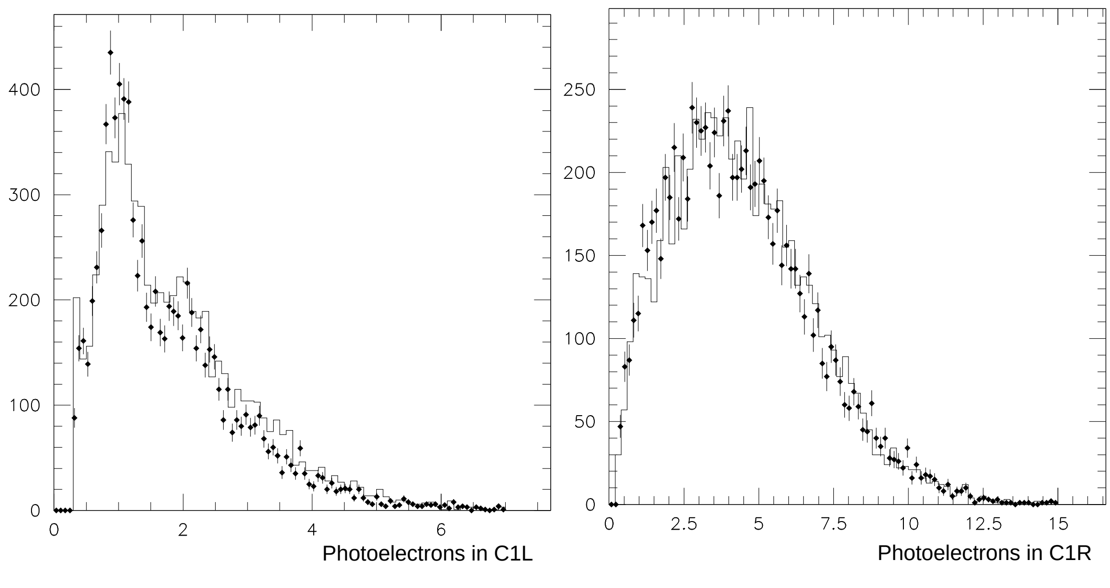

Figure 5.11: Number of photo electrons yielded by C1 Čerenkov counter.

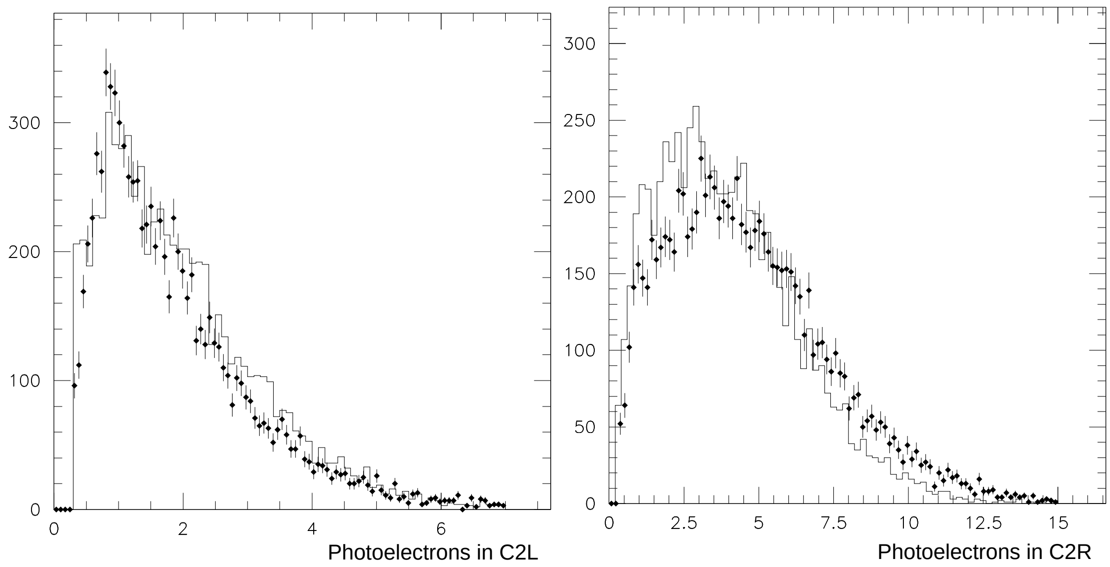

Figure 5.12: Photoelectron yield in Čerenkov counter C2.

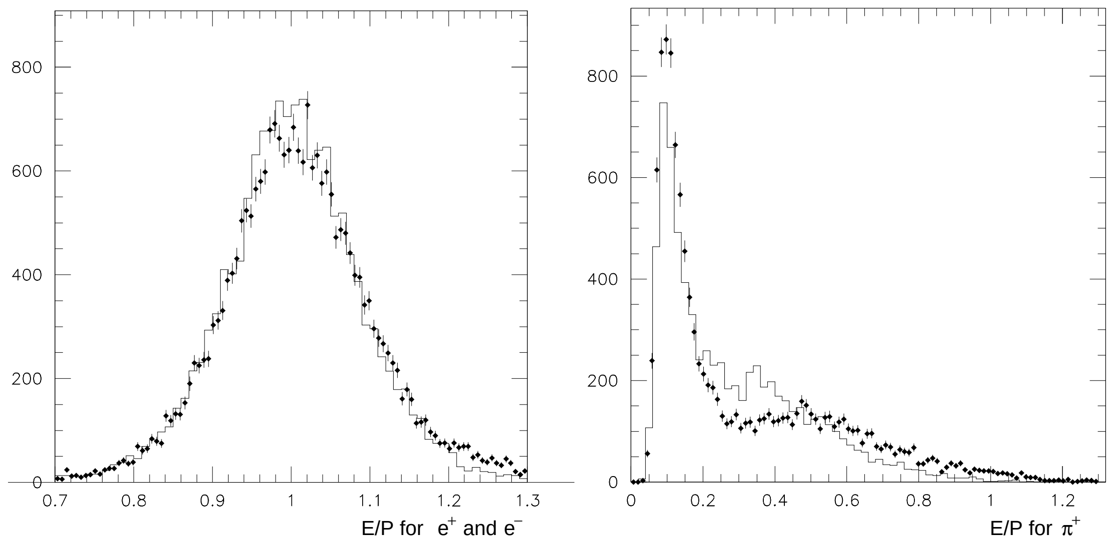

Figure 5.13: E/P for electrons and pions.

Chapter 6

Normalization

6.1 Introduction

Equation 4.2 in section 4.1 states how the branching ratio (BR) for the decay of a particle a to a final state b is obtained. It is adapted here to the $K_{\pi\mu e}$ and K_{DAL} channels. In the previous chapters, we showed that no signal events were found and that there is also no background. In such a null experiment, one usually quotes an upper limit of the BR, defined as follows:

$$BR_{\pi\mu e} < BR_{DAL} \frac{N_{\pi\mu e}}{N_{DAL}} \frac{A_{DAL}}{A_{\pi\mu e}} C \tag{6.1}$$

$N_{\pi\mu e}$ is usually set to 2.3, corresponding to a 90% confidence level (C.L.), i.e the probability is 10% to see a null experiment, if the expected number of events is 2.3. N_{DAL} is set to 1.408×10^7, the number K_{DAL} events found, while the acceptances A_{DAL}, $A_{\pi\mu e}$ and the correction factor C remain to be determined. The estimation of these factors is the goal of the following sections.

6.2 Calculation of the acceptance and of the correction factor

6.2.1 Overview

Equation 6.1 gives a formula for determining an upper limit on the branching ratio for $K_{\pi\mu e}$. The acceptance A for a given decay is a function of the kinematics of the decay, the geometry of the detector, the efficiency of the detector elements, the efficiency of the hardware and software triggers and finally also of the various cuts applied to the data during the signal search. Hence, the acceptance values for the signal and the normalization decay are generally not the same, necessitating some means of independently determining each. A Monte Carlo simulation of the experiment is used to determine the acceptance of $K_{\pi\mu e}$ and K_{DAL}. This can be divided into two steps. The first one comprises a generation of Monte Carlo events with KAY, as described in the previous chapter. The events that are geometrically accepted by KAY are then, in a second step, subjected to almost the same chain of analysis as the real data.

6.2.2 Generation of Monte Carlo events

About 1.5 million $K_{\pi\mu e}$ and 2.5 millions K_{DAL} events were generated with KAY. A detailed list of the physics processes simulating the interaction of the particles with matter and of additional parameters is given in Appendix B. The MWPC's are assumed to be uniformly 95% efficient but all dead wires are also removed in the Monte Carlo. This matches the efficiency observed for good K_τ data very well. The efficiencies of the muon chambers are taken from [66]. Finally, to speed up the generation of events, all three charged daughter particles in $K_{\pi\mu e}$ or K_{DAL} are required to hit the A-counter. As soon as a charged daughter particle fails to hit the A-counter, the event gets aborted. 20.4% of the $K_{\pi\mu e}$, 8.3% of the K_{DAL} and 25.6% of the K_τ events pass this requirement, reflecting the basic kinematical acceptance of our setup for these decays.

6.2.3 Trigger simulation

Although the T0 trigger is common for all trigger types, it has a slightly different acceptance for $K_{\pi\mu e}$ and K_{DAL} due to the different regions of phase space the daughter particles occupy. To model this trigger level for the analysis of Monte Carlo events, a clump is assumed to correspond to an A•SH coincidence. The requirement of a physical hit pattern is implemented in software.

Running this simulation on Monte Carlo data, 19.01% of $K_{\pi\mu e}$, 8.05% of K_{DAL} and 24.1% of K_τ reconstruct three clumps. Requiring in addition a physical hit pattern, the acceptance drops to 13.53% for $K_{\pi\mu e}$, 5.08% for K_{DAL} and 18.8% for K_τ. While only about 7% of the events are lost, because no A•SH is found, the requirement of a physical hit pattern leads to a 29% loss in acceptance. A deeper look shows that most of the events rejected by this requirement are badly mismeasured ones which would be discarded anyway later in the course of the analysis. In fact the requirement rejects only about 5%

of the good $K_{\pi\mu e}$ events. It would be easy to catch also these events, but it would come at the cost of a significantly higher T0 trigger rate.

Running this implementation of the T0 trigger on data events, 99.7% of good K_τ and 97.1% of good K_{DAL} events pass it. There are several reasons why less than 100% pass. First, a clump imposes slightly tighter timing requirements than an A•SH. Requiring an A-counter hit within ±7.5 ns, corresponding to 3 times the width of the A-counter signal, and a hit in the calorimeter within ±20 ns, corresponding to twice the width of the signal, would allow us to re-gain about one third of the 'lost' triggers. A second reason is lost information. The T0 trigger is physically located just above the calorimeter, while the ADC/TDC's are located in the electronic house. Especially at high trigger rates some information gets lost on the way from the trigger to the TDC/ADC's. Hence some events might have triggered on additional A•SH signals, which got lost.

There are still a few smaller differences between data and Monte Carlo simulation which we must consider, e.g. parasitic background is not simulated. Hence Monte Carlo events reconstruct less clumps than data events, on average 3.9 clumps are found in good K_τ MC events compared to 4.9 in K_τ data. The additional clumps introduce the possibility that some of the events pass the T0 trigger level additionally, since the trigger examines all possible combinations with two A•SH coincidences on one side and a third A•SH on the other side for a physical hit pattern. If any of the combinations is acceptable, the event is kept. Especially also a few good events might pass that would be rejected otherwise. This possibility is examined on good data events by allowing only the clumps that belong to a track coming from the vertex. 98.3% of the K_τ and 92.2% of the K_{DAL} events pass. This means that, by neglecting the events which reconstruct less than three clumps, 1.4% of the good K_τ and 5.0% of the good K_{DAL} are triggered by additional A•SH signals. Applying the same analysis to Monte Carlo events, 1.3% of good K_τ, 1.6% of good K_{DAL} and 0.7% of good $K_{\pi\mu e}$ passed T0 due to additional A•SH signals. To correct for this difference between data and Monte Carlo events, a correction factor $C_{T0} = 1.050 \times 0.984 \times 0.9925 \times 1.007 = 1.033$ is introduced, where it is assumed that 0.75% of good data $K_{\pi\mu e}$ events would have passed the T0 trigger due to additional A•SH signals. This assumption is based on (kinematical) similarities between $K_{\pi\mu e}$ and K_τ events.

The electron and positron requirement of the T1 trigger level is implemented by requiring at least 0.25 photoelectrons in one of the photomultipliers in C1 and C2 on the appropriate side, identical to the requirement of the hardware trigger. The coincidence between the SwissMix and the B-counter, required to identify a muon, is simulated in software. The acceptance after the T1 trigger level drops to 5.24% for $K_{\pi\mu e}$ and 2.15% for K_{DAL}, where the main source of loss is due to the electron identification. To conclude the examination of the T1 trigger level, we have to estimate the efficiencies of the MUE and the ELER T1 trigger for data. Since MUE requires (A•SH) • (C1L•C2L) • (SwissMix) while ELER asks for (A•SH) • (C1L•C2L) • (C1R•C2R), we can not a priori assume that they are identical. The most unbiased way to conduct this examination is to select events with an $e\mu e$ signature from the Tau data stream written in Pass1. These events should satisfy the MUE as also the ELER requirement. Unfortunately, we do not expect to find more than a few hundred of $e\mu e$ events in the Tau data, and therefore the statistical error would dominate. The EEPS stream offers a second possibility to search for $e\mu e$ events. Taking the ratio of the number of the prescaled ELER events with a MUE latch divided by the number of prescaled ELER events, the level one MUE trigger efficiency is calculated to be $74.6 \pm 1.5\%$. The ELER T1 trigger efficiency is calculated to be the ratio of the number of $e\mu e$ events having an ELER and a MUE latch divided by the number of $e\mu e$ events having only a MUE latch. This yields to an ELER efficiency of $89.7 \pm 0.5\%$. This leads to a correction factor $C_{T1} = 0.897/0.746 = 1.202$.

The T2 trigger level does not affect the $K_{\pi\mu e}$ data, and for K_{DAL}, we count only events for which the prescale level is set and hence are independent of the subdivision into low mass and high mass events. But, we like to exclude the possibility of hardware failures of the prescale unit, i.e. to ensure that the prescale level was really 10 during data taking. Since we know that the events with a high mass or a MUE trigger latch are not prescaled, the number of K_{DAL} events can also be calculated to be:

$$N_{total} = N1 + N2 \times 10 \tag{6.2}$$

where $N1$ is the number of events with ELER.and.(HIMASS.or.MUE) and
$N2$ is the number of events with ELER.and.(.not.HIMASS).and.(.not.MUE)

This leads to within 0.25% to the same number of K_{DAL} events than counting the number of events with a prescale latch set and multiplying them by 10. This small difference is mainly due to a slightly different treatment of the data by the online analysis, EEPS events are not subject to the test of the Čerenkov counters.

No additional precaution is required in modeling the T3 trigger level, although the Monte Carlo does not include background. T3 is identical for $K_{\pi\mu e}$ and K_{DAL}, hence a possible rejection of events in the data and normalization channel cancels.

6.2.4 Monte Carlo online analysis

The remaining Monte Carlo events are subjected to an identical filter code as the one used on real data, i.e. $K_{\pi\mu e}$ MC events are required to pass the Čerenkov counter and muon tests, while the three clump requirement for a T0 trigger is automatically fulfilled. The filtering reduces the acceptance for $K_{\pi\mu e}$ to 4.65%. But we have to be careful. The online analysis was running only during the second part of the run in 95, and furthermore many data events have a MUE and an ELER trigger latch due to background, while we do not find such events in the MC. The additional ELER trigger latch changes the online analysis slightly, e.g. such events are not required to pass the check for the presence of a muon. For $K_{\pi\mu e}$ events with a PME and an ELER trigger latch the acceptance drops only to 4.91%. Weighting the three different acceptances with the appropriate number of events in the different classes, we get an acceptance for the online analysis of 5.06%. To avoid any complications, we will state in the following only this weighted acceptance for $K_{\pi\mu e}$. Only the clump finding routine affects the K_{DAL} events with a prescale latch set (EEPS latch) which are used in the normalization. Neither the check of the Čerenkov counters nor the test for the presence of a muon rejects any EEPS events, i.e. the acceptance for K_{DAL} remains unchanged.

6.2.5 Pass1 and Pass2 Monte Carlo analysis

There would be no need to examine the Pass1 and Pass2 analysis closer, since all the significant cuts will be applied later in Pass3 again with tighter requirements. But just for reasons of completeness, we subject the remaining MC data to the Pass1 and Pass2 requirements.

In section 5.6 a good agreement between real data and Monte Carlo data for the reconstructed K^+ momentum (Fig.5.2) and the vertex miss distance s (Fig.5.7) was found. The drop in the acceptance for Pass1 to 4.16% for $K_{\pi\mu e}$and to 1.50% for $K_{DAL}$is therefore related mainly to the fact the we do not reconstruct three tracks due to inefficiencies in the MWPC's.

Since the agreement between data and MC is also reasonable for the response of the Čerenkov counters and the calorimeter (Fig. 5.11 - 5.13), we write down at this point only the acceptances for Pass2 and will examine the particle identification efficiencies in the next section dealing with the Monte Carlo analysis of Pass3. We get an acceptance of 3.42% for $K_{\pi\mu e}$ and of 1.47% for K_{DAL}.

In summary, the various inefficiencies and trigger requirements reduce the acceptance at this point to 16.8% and 17.7% of its bare geometrical value for $K_{\pi\mu e}$ and K_{DAL}, respectively.

6.2.6 Pass3 Monte Carlo analysis

Since the Monte Carlo does not include the timing aspects, differences in the timing resolution have to be taken into account by the correction factor C. Referring to Table 4.5, we recognize that the timing of the positron in the calorimeter is better than the timing of the muon in the calorimeter. An estimation gives that 84.9% of the potential $K_{\pi\mu e}$ events would pass the timing cut while 89.9% of the K_{DAL} events pass it. This leads to a correction factor $C_{TRMS} = 0.899/0.849 = 1.059$.

Maybe the most notable difference between the Monte Carlo and the data is the track χ^2 distribution (Fig. 5.6). As already mentioned, this is mainly due to our imperfect knowledge of the field in the spectrometer magnets. But since the track χ^2 does not depend on the particle type all effects cancel. To aim for an identical rejection as in data, the cut on Monte Carlo data is tightened to $\chi^2 = 8$.

The target likelihood cut does not serve to define K_{DAL} events since the K^+ reconstruction for these events is incomplete due to the undetected gamma. Consequently, the cut is only applied to the $K_{\pi\mu e}$ sample. Ideally, the kaon phase space at the target for reconstructed Monte Carlo events would match that of data events. Unfortunately this is not the case (Fig. 5.5) for reasons which are explained in section 5.6.1. Hence, no target likelihood cut is applied to MC data, requiring a measurement of the efficiency of the cut for which we turn to K_τ data. Here the cut is 91.1% efficient. Figure 6.1 compares the target likelihood distribution for MC K_τ and MC $K_{\pi\mu e}$ events. No difference is observed. Hence the target likelihood cut is also 91.1% efficient for potential $K_{\pi\mu e}$ events yielding a correction factor $C_{TGLK} = 1.098$.

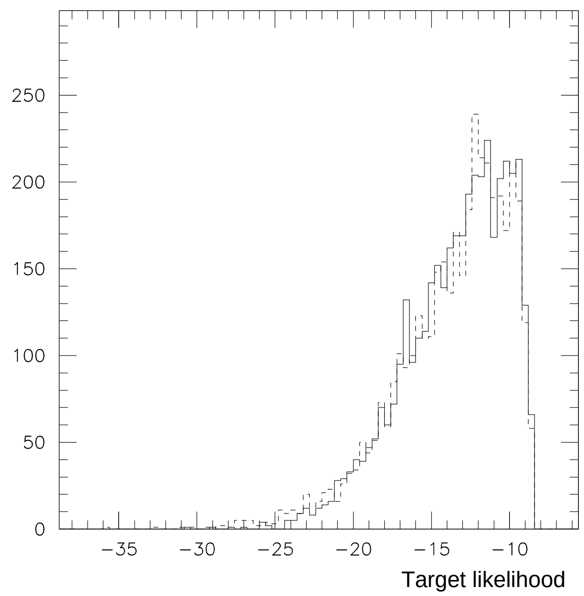

Figure 6.1: Target likelihood for MC K_τ (solid), and MC $K_{\pi\mu e}$ (dashed) events.

$K_{\pi\mu e}$ and K_{DAL} share only two of the three final state particles. Therefore we need to ensure that the Monte Carlo models the response of the detector for the positron and the muon correctly, i.e. we have to compare the efficiencies of the particle identification cuts for MC and real data.

Concerning the positron, the Čerenkov inefficiencies (section 3.6.2) are already taken into account during the generation of the Monte Carlo events, i.e. no correction for the positron due to the Čerenkov counters is necessary. The shower counter efficiency on positrons with an E/P cut of $0.8 < E/P < 1.2$ is 89.7% for data events and 95.2% for MC events. The inefficiency of this cut is mainly due to additional particles hitting the shower counter at the same spot as the positron. This also explains the difference between MC and data, since the MC does not simulate background, more clumps are found in data than in MC. This is taken into account by a correction factor $C_{positron} = 0.897/0.952 = 0.942$.

Four cuts are made to identify the muon. It is required to have a distance b between the hit in the B-counter and the projected track from the MWPC's of less than 10 σ_B (4.3.6), at least 50% of the expected hits in the muon chambers, less than 450 MeV energy deposited in the calorimeter, and finally, it is required not to be consistent with a positron. To extract a clean sample of data muons is difficult. Only muons from $e\mu e$-events promise sufficient statistics and cover the whole phase space. But since the decay $K_{\mu 3}$ is suppressed compared to $K_{\pi 2}$ by almost an order of magnitude and since the rejection of pions against muons is not better than 10%, the muon sample will be heavily contaminated by pions, making it almost impossible to estimate the efficiencies of the cuts (see Fig 3.20b). The way out of this dilemma is the use of beam muons, recorded with all the beam line magnets switched off, to estimate the efficiencies of the muon chambers and the implementation of the efficiencies found in the Monte Carlo. Beam muons have sufficient energy to reach the C-counter and are free from background. A good possibility to ensure a correct modeling of the interactions in the muon stack is to compare the deviation b measured at the B-counter (Fig. 6.2). The excellent agreement found, together with the efficiencies determined from data secures that no corrections for the first two cuts are required. For the cut on the energy deposited in the calorimeter, we have to consider again the absence of background in the Monte Carlo, i.e. the possibility that two particles hit the calorimeter at the same spot is larger in data than in MC. This gives rise to a correction factor of 0.983/0.948, where 0.983 is the efficiency of the cut for MC events and 0.948 is the efficiency for data events (section 4.5). The 'anti-positron-cut' requires a final correction, again due to the lack of background. While it is 96.9% efficient for MC-events, the efficiency drops to 93.8% for data events. Since a muon is required to have less than 0.45 GeV deposited in the calorimeter, the efficiency of this cut for muons is higher than the comparable efficiency for the pions. All corrections for the muon combined together leads to $C_\mu = (0.983/0.948) \times (0.969/0.938) = 1.071$

In section 4.6.6, it is mentioned that the restriction to a maximum of four tracks results in a loss of 1.3% of the good K_τ events. Since this cut is only applied to $K_{\pi\mu e}$ data, but

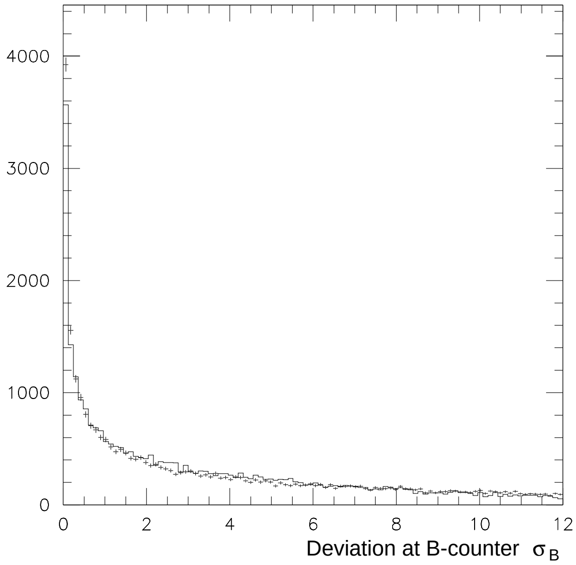

Figure 6.2: Deviation σ_B for MC (histogram) and data (error bars) $e\mu e$ events.

not to K_{DAL} data and MC events, this implies a correction factor $C_{track} = 1.013$.

Only the $K_{\pi\mu e}$ data events are subject to the photon veto described in section 4.6.9. By studying good K_τ data events, the efficiency of the photon veto is estimated to be 98.2%, yielding to a correction factor of $C_{photon} = 1.018$.

In section 4.6.12 we found that the decay chain $(K_{\mu 3})_{DAL}$ also contributes to the final sample of K_{DAL} data events. The muon veto for the pion is not designed to reject $(K_{\mu 3})_{DAL}$, its main goal is to suppress beam muons. The branching ratio of this decay chain is only 6.7 times lower than that of K_{DAL} events, so that the contamination is not negligible. To estimate the correction factor, we count the number of Monte Carlo $(K_{\mu 3})_{DAL}$ events, weighted by the $(K_{\mu 3})_{DAL}$ branching ratio, which pass all the cuts used to define K_{DAL}. This yields $C_{e\mu e} = 1.021$.

Table 6.1 gives an overview of the acceptances after the different Pass3 cuts. The statistical errors $\sigma_{\mathrm{A}}/\mathrm{A}$ are below 1%. We find a final acceptance of 1.91% for $K_{\pi\mu e}$ and of 0.65% for K_{DAL}. Table 6.2 summarizes the correction factors C.

Cut	$A_{K_{\pi\mu e}}$	$A_{K_{DAL}}$
KAY	20.4%	8.3%
T0	13.53%	5.08%
T1	5.24%	2.15%
Filter code	5.06%	2.15%
Pass1	4.16%	1.50%
Pass2	3.42%	1.47%
Track χ^2	3.27%	1.41%
Fid. volume	2.75%	1.40
Pion ID	2.70%	1.34%
Muon ID	2.60%	—
Electron ID	2.45%	1.20%
Positron ID	—	1.10%
μ veto for π^+	2.39%	1.09%
π on the left	2.38%	—
M_{ee} mass	2.20%	0.99%
K^+ mass	1.99%	—
$M_{\pi ee}$ mass	—	0.69%
s_{NORM}	1.91%	0.66%

Table 6.1: Summary of acceptances.

Correction	Value	$\pm\sigma_C/C$
T0 trigger level	1.033	0.010
T1 trigger level	1.202	0.016
Timing	1.059	0.007
Target likelihood	1.098	0.006
Positron ID	0.942	0.011
Muon ID	1.071	0.014
Additional Tracks	1.013	0.006
Photon veto	1.018	0.006
$(K_{\mu 3})_{DAL}$ contamination	1.021	0.015
Total	1.502	0.029

Table 6.2: Correction factors C.

Chapter 7

Results and conclusions

7.1 $K^+ \to \pi^+\mu^+e^-$ branching ratio

We are now in a position to quote an upper limit on the branching ratio of $K^+ \to \pi^+\mu^+e^-$. For convenience, we write down equation 6.1 again:

$$BR_{\pi\mu e} < BR_{DAL}\frac{N_{\pi\mu e}}{N_{DAL}}\frac{A_{DAL}}{A_{\pi\mu e}}C \tag{7.1}$$

The values of all factors in equation 7.1 are determined in the previous chapters and summarized in table 7.1. They yield:

$$BR_{\pi\mu e} < 2.1 \times 10^{-10} \tag{7.2}$$

BR_{DAL}	2.53×10^{-3}
$N_{\pi\mu e}$	2.3
N_{DAL}	1.408×10^{7}
$A_{\pi\mu e}$	1.91×10^{-2}
A_{DAL}	0.66×10^{-2}
C	1.502

Table 7.1: Numerical values substituted into equation 7.1.

7.2 Conclusions

In section 1.2.4, we studied different extensions of the standard model allowing for violation of the lepton number conservation law. We found that forbidden decays like $K_{\pi\mu e}$ can seriously challenge models involving horizontal bosons and leptoquarks. Unfortunately, the branching ratio is only proportional to one over the fourth root of the mass (equations 1.6 and 1.8), hence combining the old and our result, yielding an upper limit of 1.1×10^{-10}, results only in a 20% increase in the mass limit. This improvement does not allow to rule out any theoretical model. But considering the data collected during the run in 1996, now in the process of being analyzed with an anticipated improvement of the branching ratio of a factor of five and in view of a future run in 1998, we will finally be able to more than double the mass limit or, even more exciting, eventually find lepton number non conservation.

It is not only additional running time, but also an improved apparatus that will allow this. One of our main obstacles during the run in 1995 was a large trigger rate of events not reconstructing three tracks (see Chap. 4.4). To overcome this, we added for the run in 1996 a new trigger hodoscope, consisting of twenty, 3 mm thick, horizontally arranged scintillation counters (ten on each side) between the first two MWPC's. Requiring coincidences (time and position) between the A•SH and the new hodoscope for a T0 trigger, this trigger rate could be significantly reduced allowing us to run at higher beam intensity. For the run in 1997, dedicated to measure the decays $K^+ \to \pi^+\mu^+\mu^-$, $K^+ \to \pi^0 e^+\mu$, K_{e3}, and $K^+ \to \pi^+\pi^- e^+\nu$, K_{e4}, Fastbus Smart Crate Controllers were installed, reducing the readout time of the fastbus modules and permitting us to double the trigger rate. Additionally a beam pixel counter consisting of 384 7×7 mm^2 scintillating pixels, with each tile viewed by an individual photo tube through an air light pipe, was installed between Q9, the last beam line magnet and the decay tank. This counter is maybe less important for $K_{\pi\mu e}$, but is critical for decays like K_{e3} and K_{e4} with a missing neutral particle, allowing us to better track the kaon back to the target and estimate its momentum.

Appendix A

Cuts for offline reconstruction

Variable	Cut	Description
ATCUT1	10.0 ns	A-counter TDC cut in clump finding on raw data
ATCUT2	10.0 ns	A-counter TDC cut in clump finding after LBOX
SHTCUT1	10.0 ns	Calorimeter TDC cut in clump finding on raw data
SHTCUT2	10.0 ns	Calorimeter TDC cut in clump finding for data that passed ATCUT2
ESHMIN1	0.075 GeV	Min. deposited energy in central module of clump
ESHMIN2	0.075 GeV	Min. deposited energy in clump consisting of 3×3
NCMAX	3	Max. number of wires in a MWPC cluster
PNTCUT	15.0	χ^2 cut in space point finding
WINP1X WINP1Y WINP2X WINP2Y WINP3X WINP3Y WINP4X WINP4Y	$0.37 \times XCLP^{+17.9}_{-16.4}$ $0.375 \times YCLP^{+18.2}_{-19.7}$ $0.50 \times XCLP^{+18.2}_{-17.7}$ $0.517 \times YCLP \pm 17.4$ $0.94 \times XCLP \pm 36.0$ $0.81 \times YCLP \pm 24.0$ $0.95 \times XCLP \pm 25.0$ $1.00 \times YCLP \pm 25.0$	Upper and lower border in cm of windows in space point and track finding for all four chambers in X and Y. $XCLP$ and $YCLP$ are the X-position and the Y-position of the clump, respectively.
X4TRCT	30.0	χ^2 cut in X for four chamber tracks
Y4TRCT	10.0	χ^2 cut in Y for four chamber tracks
TR3CUT	30.0	χ^2 cut for three chamber tracks
DXYSH	12.0 cm^2	Square deviation between position of clump and position of track at calorimeter in track finding.

TRKCHI2	100000	χ^2 cut on track after momentum fitting
MTRKCL	3	Max. number of tracks that can be assigned to a clump
VTLPMX	3000	Max. number of combinations between all tracks and all clumps
NTRKL	1	Min. number of tracks on beam left side in vertex
NTRKR	1	Min. number of tracks on beam right side in vertex
VPH	8.0 GeV	Max. total momentum of tracks in vertex
VXCUT	10.0 cm	Cut on X-position of vertex
VYCUT	10.0 cm	Cut on Y-position of vertex
SP2WIND	1.0 cm	Window half size for 2 wire space points
SPTT_WIN	45	Window for wires in vicinity of original space point to re-find space point using track angle.
SPTT_LSE	15.0	DX, DY cut for quadruplets and triples in re-finding space points.
SPTT_TGT	15.0	χ^2 cut for re-finding space points
CKTIME	5.0 ns	Čerenkov timing cut for (in-time) light to be assigned to a track
C1PEMIN C2PEMIN CKTOUT	0.5 photo electrons 0.5 photo electrons 25.0 ns	Light in the Čerenkov counter x gets also collected, if more than CxPEMIN is deposited and the timing is larger than CKTOUT
MUTIME	10.0 ns	B- and C-counter timing cut

Appendix B

Input card for generating $K^+ \to \pi^+\mu^+e^-$ MC events

C⟶ GENERAL INPUT:
C
C⟶ Run number, first event number:
RUNG 2000 1
C⟶ Automatic computation of the tracking medium parameters:
AUTO 1
C
C⟶ BEAM INPUT:
C
C⟶ Beam phase space distribution:
C⟶ 1=Gaussian, 2=flat, 3=Sanford Wang, 4=read datafile with particles
C⟶ 5=read FZ-file
BSHA 4
C⟶ Z-position at start
BRMP -490.0
C⟶ Index type of primary particle type:
IBPA 41
C
C⟶ MAGNETS:
C
C⟶ Switch on magnet field in beam line:
C⟶ MFBE = 0 magnet fields off
C⟶ = 1 magnet fields taken from fieldmap and GRKUTA
C⟶ to transport particle (NOT YET ESTABLISHED)

C⟶ = 2 magnet fields taken from fieldmap and GRKUTA
C⟶ to transport particle (NOT YET ESTABLISHED)
C⟶ = 3 magnet fields taken from approx. and GHELIX
C⟶ to transport particle
MFBE 3
C⟶ Scale magnet fields of beam line dipoles (5-10 are spare):
MFSD 1.00 1.00 1.00 1.00 0.00 0.00 0.00 0.00 0.00 0.00
C⟶ Scale magnet fields of beam line quadrupoles (10 is spare):
MFSQ 1.00 1.00 1.00 1.00 1.00 1.00 1.00 1.00 1.00 0.00
C⟶ Switch on magnet field of M48D48:
C⟶ M48D = 0 magnet fields off
C⟶ = 1 magnet fields taken from fieldmap and GRKUTA to transport particle
C⟶ = 2 magnet fields taken from fieldmap and GHELIX to transport particle
C⟶ = 3 magnet fields taken from approx. and GHELIX to transport particle
M48D 1
C⟶ Scale M48D48
MSC1 1.020
C⟶ magnet field of M120D36:
C⟶ M120 = 0 magnet fields off
C⟶ = 1 magnet fields taken from fieldmap and GRKUTA to transport particle
C⟶ = 2 magnet fields taken from fieldmap and GHELIX to transport particle
C⟶ = 3 magnet fields taken from approx. and GHELIX to transport particle
M120 1
C⟶ Scale M120D36
MSC2 1.019
C
C⟶ <u>PHYSICS STEERING PARAMETER SEE PHYS-001 OF GEANT MANUAL:</u>
C⟶ Decay in flight
DCAY 1
C⟶ Allow Pi+- decay (user parameter):
PDCA T
C⟶ Allow K+- decay (user parameter):
KDCA T
C⟶ Track neutrinos (user parameter):
TNEO F
C⟶ Track neutrons (user parameter):
TNEU F
C⟶ Multiple Scattering: =1,2 Moliere formula used ; =3 Gauss used:
MULS 1

C⟶ Nuclear fission induced by Photon:
PFIS 0
C⟶ Muon-Nucleus interaction:
MUNU 1
C⟶ Continuous energy loss =1,3 energy loss with delta ray and Landau;
C⟶ =2 no delta ray but Landau; =4 no delta no Landau but e-loss:
LOSS 1
C⟶ Photo-electric effect:
PHOT 1
C⟶ Compton scattering:
COMP 1
C⟶ Pair production, the interacting Gamma is stopped:
PAIR 1
C⟶ Bremsstrahlung, the interacting particle is not stopped:
BREM 1
C⟶ Rayleigh effect, the interacting Gamma is not stopped:
RAYL 0
C⟶ Delta-ray production:
DRAY 1
C⟶ Positron annihilation, the e+ is stopped:
ANNI 1
C⟶ Hadronic interactions:
HADR 1
C⟶ Light Absorption:
LABS 0
C⟶ Collision sampling, energy loss in gases (PHYS-334):
STRA 0
C⟶ Synchrotron radiation in magnetic field:
SYNC 0
C⟶ Čerenkov radiation:
CKOV 1
C⟶ Ray tracing (user parameter):
TRCE 0
C⟶ The next data cards are the GEANT cuts on kinetic energy in GeV:

C⟶ Gamma	Electron	neutral Hadron	charged Hadron
C⟶ Muon	Electron brems	Muon & Had brems	Delta rays by e^{+-}
C⟶ Delta rays by muon	Pair prod. muon	TOF in seconds	
CUTS 1.0E-3	1.0E-3	1.0E-3	1.0E-3
1.0E-3	1.0E-3	1.0E-3	1.0E-3

```
        1.0E-3             1.0E-3               1.0E-6
C
C—→ CREATE NEW PARTICLES, SET BR'S AND CONDITIONS:
C—→ Define new particles:
C—→   PID  NAME    TYPE  MASS(GeV)    CHARGE  LIFE TIME(SEC)
PADK  41   'NK+ '  4     0.493677     1.      1.2371E-8
      42   'PI+ '  4     0.13956995   1.      1. 2.6030E-8
      43   'MU+ '  5     0.10565839   1.      0.10565839
      44   'E- '   2     0.00051100   -1.     1.0000E15
C—→ Set decay length for new particles
LNDK    0.  550.
        0.    0.
        0.    0.
        0.    0.
C—→ Branching ratios (6 numbers per particle from PADK;
C—→ all 0 for user matrices)
BRDK      0.  0.  0.  0.  0.  0.
        100.  0.  0.  0.  0.  0.
        100.  0.  0.  0.  0.  0.
        100.  0.  0.  0.  0.  0.
C—→ Mode(1..6) = 10**4 particle3 + 10**2 particle2 + particle1
MODK 434244  0  0  0  0  0
        504  0  0  0  0  0
      20404  0  0  0  0  0
          0  0  0  0  0  0
C—→ Matrix for particles with no BR's defined
MXDK 'PHAS'



C—→ Numbers of positive, negative and continuous conditions
PCDK 0 1 1 1
NCDK 0 0 0 0
CCDK 0 0 0 0
C—→ List of volumes packed according to PCDK, NCDK and CCDK
PVDK
     'ACNT'
     'ACNT'
     'ACNT'
```

NVDK

CVDK

```
C⟶ SELECT ACTIVE DETECTOR PARTS:
C⟶ Activate geometries:
GEOM  'GLOB' 'TARG' 'BEAM' 'DECA' 'M48D' 'MWP1' 'MWP2' 'M120'
      'CER1' 'MWP3' 'CER2' 'MWP4' 'ACNT' 'SHOW' 'MUO1' 'BCNT'
      'MUO2' 'CCNT'
C⟶ Activate writing hits:
SETS  'GLOB' 'TARG' 'BEAM' 'DECA' 'MWP1' 'MWP2' 'CER1' 'MWP3'
      'CER2' 'MWP4' 'ACNT' 'SHOW' 'MUO1' 'BCNT' 'MUO2' 'CCNT'
C⟶ Activate writing digitization:
DIGI  'MWP1' 'MWP2' 'CER1' 'MWP3' 'CER2' 'MWP4' 'ACNT' 'SHOW'
      'MUO1' 'BCNT' 'MUO2' 'CCNT'
C
C⟶ WRITE E865-EVENT
C⟶ Flag for writing event
EVNT T
C⟶ Mask to pack MC word
PACK 'GLIF' 'MWPC' 'CERK' 'CLMP' 'MUON' 'VRTX' 'MOME'
```

Bibliography

[1] A. M. Diamant-Berger *et al.*, "*Study of some rare decays of the K^+ meson*", Phys. Lett. **62B** (1976) 485.

[2] A. M. Lee *et al.*, "*Improved limit on the branching ratio of $K^+ \to \pi^+\mu^+e^-$*", Phys. Rev. Lett. **64** (1990) 165.

[3] G. Marx, "*Die Wechselwirkung der Elementarteilchen und die Erhaltungssaetze*", Acta Phys. Acad. Sci. Hung. **3** (1953) 55.

[4] E. J. Konopinski and H. M. Mahmoud, "*The universal Fermi interaction*", Phys. Rev. **92** (1953) 1045.

[5] L. B. Okun, "*Certain problems of weak interaction theory*", in *Proceedings of the 1960 Annual International Conference on High Energy Physics at Rochester*, p. 743, 1960.

[6] G. Danby *et al.*, "*Observation of high energy neutrino reactions and the existence of two kinds of neutrinos*", Phys. Rev. Lett. **9** (1962) 36.

[7] U. Bellgardt *et al.*, "*Search for the decay $\mu^+ \to e^+e^+e^-$*", Nucl. Phys. **B299** (1988) 1.

[8] R. D. Bolton *et al.*, "*Search for rare muon decays with the crystal box detector*", Phys. Rev. **D38** (1988) 2077.

[9] P. Abreu *et al.*, "*Upper limits on the branching ratios $\tau \to \mu\gamma$ and $\tau \to e\gamma$*", Phys. Lett. **B359** (1995) 411.

[10] A. Bean *et al.*, "*A search for $\tau \to \gamma\mu$: A test of lepton number conservation*", Phys. Rev. Lett. **70** (1993) 138.

[11] J. Bartelt *et al.*, "*Search for neutrinoless decays of the tau lepton*", Phys. Rev. Lett. **73** (1994) 1890.

[12] H. Albrecht *et al.*, "*Search for neutrinoless tau decays*", Z. Phys. **C55** (1992) 179.

[13] K. Arisaka *et al.*, "*Improved upper limit on the branching ratio $B(K_L^0 \to \mu^\pm e^\mp)$*", Phys. Rev. Lett. **70** (1993) 1049.

[14] A. Weir *et al.*, "*Upper limits on $D^\pm$ and $B^\pm$ decays to two leptons plus $\pi^\pm$ or $K^\pm$*", Phys. Rev. **D41** (1990) 1384.

[15] A. Freyberger *et al.*, "*Limits on flavour changing neutral currents in D^0 meson decays*", Phys. Rev. Lett. **76** (1996) 3065.

[16] R. Ammar *et al.*, "*Search for B^0 decays to two charged leptons*", Phys. Rev. **D49** (1994) 5701.

[17] C. Dohmen *et al.*, "*Test of lepton number conservation in $\mu \to e$ conversion on titanium*", Phys. Lett. **B317** (1993) 631.

[18] P. Langacker and U. Sankar, "*$K_L \to \mu e$ in $SU(2)_L \times U(1)$ and $SU(2)_L \times SU(2)_R \times U(1)$ models with large neutrino masses*", Phys. Rev. **D38** (1988) 2841.

[19] A. Barroso *et al.*, "*$K_L \to \overline{\mu} e$: Can it be observed?*", Phys. Lett. **134B** (1984) 123.

[20] H. E. Haber and G. L. Kane, "*The search for supersymmetry: Probing physics beyond the standard model*", Phys. Rep. **117** (1985) 76.

[21] M. Drees, "*An introduction to supersymmetry*", in *Inauguration conference of the Asia Pacific Center for theoretical physics, Seoul*, 1996, hep-ph/9611409.

[22] L. Girardello and M. T. Grisaru, "*Soft breaking of supersymmetry*", Nucl. Phys. **B194** (1982) 65.

[23] C. S. Aulakh and R. N. Mohapatra, "*The neutrino as the supersymmetric partner of the majoron*", Phys. Lett. **119B** (1982) 136.

[24] I. Hinchliffe and T. Kaeding, "*B- and L-violating couplings in the minimal supersymmetric standard model*", Phys. Rev. **D47** (1993) 279.

[25] G. Costa and F. Zwirner, "*Baryon and lepton number nonconservation*", Nuovo Cimento Riv. **9** (1986) 1.

[26] J. Ellis and D. V. Nanopoulos, "*Flavour-changing neutral interactions in broken supersymmetric theories*", Phys. Lett. **110B** (1982) 44.

[27] B. A. Campbell, "*Supersymmetry and neutral-flavour nonconservation*", Phys. Rev. **D28** (1983) 209.

[28] F. Borzumati and A. Masiero, "*Large muon- and electron-number violations in supergraphity theories*", Phys. Rev. Lett. **57** (1986) 961.

[29] B. Mukhopadhyaya and A. Raychaudhuri, "*$K_L \to \mu e$: A possible probe of slepton mass splitting?*", Phys. Rev. **D42** (1990) 3215.

[30] E. Farhi and L. Susskind, "*Technicolor*", Phys. Rep. **74** (1981) 278.

[31] K. D. Lane, "*An introduction to technicolor*", in *The building blocks of creation, Boulder*, 1993.

[32] S. Dimopoulos and J. Ellis, "*Challenges for extended technicolor theories*", Nucl. Phys. **B182** (1981) 505.

[33] R. N. Cahn and H. Hariri, "*Bounds on the masses of neutral generation-changing bosons*", Nucl. Phys. **B176** (1980) 135.

[34] T. Appelquist *et al.*, "*Higher mass scales and mass hierarchies*", Phys. Lett. **B220** (1989) 223.

[35] C. Adloff *et al.*, "*Observation of events at very high Q^2 in ep collisions at HERA*", Z. Phys. **C74** (1997) 191.

[36] J. Breitweg *et al.*, "*Comparison of ZEUS data with standard model predictions for $e^+p \to e^+X$ scattering at high x and Q^2*", Z. Phys. **C74** (1997) 207.

[37] J. C. Pati and A. Salam, "*Lepton number as fourth 'color'*", Phys. Rev. **D10** (1974) 275.

[38] C. Quigg, "*Gauge theories of the strong, weak and electromagnetic interactions*", Addison-Wesley, 1983.

[39] L. Lyons, "*An introduction to the possible substructure of quarks and leptons*", Prog. Part. Nucl. Phys. **10** (1982) 227.

[40] G. Senjanović and A. Šokorac, "*Light lepto-quarks in $SO(10)$*", Z. Phys. **C20** (1983) 255.

[41] K. D. Lane and M. V. Ramana, "*Walking technicolor signatures at hadron colliders*", Phys. Rev. **D44** (1991) 2678.

[42] B. Schrempp and F. Schrempp, "*Light leptoquarks*", Phys. Lett. **153B** (1985) 101.

[43] J. Wudka, "*Composite leptoquarks*", Phys. Lett. **167B** (1986) 337.

[44] S. Davidson *et al.*, "*Model independent constraints on leptoquarks from rare processes*", Z. Phys. **C61** (1994) 613.

[45] K. S. Babu *et al.*, "*Comments on the high-Q^2 HERA anomaly*", 1997, hep-ph/9703299.

[46] K. Brown, 1996, Brookhaven National Laboratory, private communication.

[47] J. R. Sanford and C. L. Wang, BNL Internal Reports 11299 & 11479, (1967).

[48] C. F. Campagnari, "*A search for the decay $K^+ \to \pi^+\mu^+e^-$*", PhD thesis, Yale University, (1988).

[49] F. Sauli, "*Principles of operation of multiwire proportional and drift chambers*", CERN Yellow Report, CERN 77-09, 1977.

[50] L. G. Christophorou *et al.*, "*Fast gas mixtures for gas-filled particle detectors*", Nucl. Instr. and Meth. **163** (1979) 141.

[51] J. Fischer *et al.*, "*Proportional chambers for very high counting rates based on gas mixtures of CF_4 with hydrocarbons*", Nucl. Instr. and Meth. **A238** (1985) 249.

[52] R. Henderson *et al.*, "*Wire chamber aging with CF_4/isobutane and argon/ethane mixtures*", IEEE Trans. Nucl. Sci. **NS-35** (1988) 477.

[53] J. Wise *et al.*, "*Chemical model for wire chamber ageing in CF_4/iC_4H_{10} gases*", J. Appl. Phys. **74** (1993) 5327.

[54] T. Yamashita *et al.*, "*Measurement of the electron drift velocity and positive ion mobility for the gases containing CF_4*", Nucl. Instr. and Meth. **A283** (1989) 709.

[55] Wire type 761 manufactured by LUMALAMPAN AB, Kalmar, Sweden.

[56] Stesalit AG, Zullwil, Switzerland.

[57] L. Meier, 1993, Paul Scherrer Institute, private communication.

[58] Kapton (Polyimid), Du Pont International S.A., 1218 Genf, Switzerland.

[59] S. Majewski and F. Sauli, CERN NP Internal Report 75-14 (1975).

[60] Mylar (Polyester), Du Pont International S.A., 1218 Genf, Switzerland.

[61] Araldit epoxy glue manufactured by CIBA-Geigy AG, Basel, Switzerland.

[62] DAG 502 manufactured by Acheson Colloiden, Scheemda, Netherlands.

[63] Elecolit 340, 3M (Schweiz) AG, 8803 Rüschlikon, Switzerland.

[64] J. V. Jelley, "*Čerekov radiation and its applications*", Pergamon Press, 1958.

[65] G. S. Atoyan *et al.*, "*Lead-scintillator electromagnetic calorimeter with wave length shifting fibre readout*", Nucl. Instr. and Meth. **A320** (1992) 144.

[66] W. Menzel, "*Eine Studie zur Nachweisempfindlichkeit des Experimentes E865 für den Zerfall* $K^+ \rightarrow \pi^+\mu^+\mu^-$", PhD thesis, University of Basel, 1996.

[67] D. D. Koetke, "*MEGA detector and trigger system*", in *AIP Conference Proceedings 243*, 1991.

[68] S. Hansen *et al.*, "*Fermilab Smart Crate Controller*", IEEE Trans. Nucl. Sci. **NS-34** (1987) 1002.

[69] V. L. Highland, "*Some practical remarks on multiple scattering*", Nucl. Instr. and Meth. **129** (1975) 497.

[70] S. Pislak, "*KAY, E865 Monte-Carlo*", Internal note (1995).

[71] R. Brun *et al.*, "*GEANT, Detector description and simulation tool*", Oct. 1994, CERN Geneva.

[72] J. Sandweiss, I.O. Skillicorn and M.S. Webster, "*BETRAF, A program for ray tracing through a magnetic lens system.*", 1962, 1967, Updated by H.N. Brown (1968, 1969, 1970, 1978, 1980).

[73] K. O. Mikaelian and J. Smith, "*Radiative correction to the decay* $\pi^0 \rightarrow \gamma e^+ e^-$.", Phys. Rev. **D5** (1972) 1763.

[74] S. M. Bermann and D. A. Geffen, "*The electromagnetic structure and alternative decay models of the* π^0", Nuovo Cimento **18** (1960) 1192.

[75] R. M. Barnett *et al.*, "*Review of particle physics*", Phys. Rev. **D54** (1996) 1.

[76] R. Brun *et al.*, "*ZEBRA, Overview of the ZEBRA system*", Feb. 1994, CERN Geneva.

[77] J. B. Birks, "*The theory and practice of scintillation counting*", Pergamon Press, 1964.

[78] C. N. Chou, "*The nature of saturation effect of flourescent scintillators*", Phys. Rev. **87** (1952) 905.

[79] R. L. Craun, "*Analysis of response data for several organic scintillators*", Nucl. Instr. and Meth. **80** (1972) 239.

Acknowledgment

I have really enjoyed the past four years. Therefore I'm happy to take this opportunity to express my deepest gratitude to all the colleagues and friends with whom I worked - to all the people who made graduate school an exciting experience.

Peter Truöl is an advisor in the fullest sense of the word. He allowed me to explore many different aspects of an experiment in high energy physics and always brought me back on the right track when I started to drift off.

Mike Zeller is the guiding spirit behind E865. His enthusiasm keeps the whole thing going. He is able to create a very stimulating atmosphere and is a vivid example that even after spending an important fraction of one's life in particle physics one can still be as enthusiastic about the subject as in the beginning.

In Heinz Kaspar, I met an excellent physicist and also a very good friend. I will always remember our lengthy discussions either at work or in the evenings with Heinz's wife Elizabeth and a glass of wine.

The other members of the Swiss crew are Johny Egger, Wolf Dieter Herold, Heinz Weyer, and Wolfgang Menzel. Thanks to all of them for supporting me.

Maybe I learned most about doing particle physics from Hong Ma. He is one of the people who is always open for questions and problems and often provides a nice solution. His helpfulness made it possible to complete this work.

Hong's counterpart in Zürich is Peter Robmann. I could always rely on his expertise. His knowledge of proportional wire chambers is remarkable and helped me quite a few times.

To Christoph Felder who came aboard as a Postdoc for Pitt and later ended up with the 'brainers' at BNL, I owe the deepest gratitude for many common hours inside and outside the 'palace'. But that's something we have to handle in private and in person, best at 'green-sauce'.

Very often Hanh Do and Juan Lozano joined us. Also to them: Many, many thanks. Without you guys, it would have been much less fun. I will never forget the basketball and soccer competitions and the glass of Nutella...

The collaboration is completed by Don Lazarus, Larry Leipuner and Pavel Rehak from BNL, Vladimir Issakov, Grisha Atoyan and Andrei Poblaguev from INR in Moscow, Bernd Bassalleck, Scott Eilerts, Horst Fischer and Jim Lowe from the University of New

Mexico, Doug Bergman and Walid Majid from Yale, and not to forget the Pitt crew: Robin Appel, Naipor Cheung, Mike Gach, Dave Kraus, Sasha Sher, Julia Thompson and many, many undergrads. Every one of you have been helpful at some time or other. Especially, I will remember Robin as a good friend.

A special thanks goes also to Kurt Bösiger and Stefan Steiner from the workshop at the Physik Institut of the University of Zürich, for - well - keeping me bored. You built two very, very reliable multiwire proportional chambers. There was almost nothing left to care about, the chambers just worked.

I do not want to forget all the other people in Zürich. The group changed, Christian Dollfus surfed away through the Internet, Dave Urner 'spins' now at Champaign, Hanspeter Beck got lost somewhere in a DAQ system at CERN and Vinz Bickel and Olaf Engfer went 'industrial'. The 'Hamburgers' Martin zur Nedden, David Müller and our rookie Stefan Hengstmann brought on their rare visits always a fresh breeze into the group. Thomi Walter and Andreas Maag were at Zürich the whole time and Andreas Suter, the intruder from the floor below, came aboard one year ago. You made these lonely days behind a computer, stuck between Ntuples and Supersymmetry much more tolerable. You were around when it was needed most - during the writing of this thesis.

Und zum Schluss, aber am wichtigste, no en ganz en grosse Dank mine Eltere, Erika und Toni. Ohni eui Unterstützig wäri sicher nüd da won i jetzt bi.

Curriculum vitae

Personalien:

Name	Pislak
Vorname	Stefan
Geboren	17. Juni 1966 in Schaffhausen
Bürgerort	Neuhausen am Rheinfall SH

Bildungsgang:

1973 - 1981	Primarschule und Sekundarschule in Neuhausen
1981 - 1986	Kantonsschule in Schaffhausen
1986	Matura, Typus C
1987 - 1992	Studium der Physik an der ETH Zürich
1992	Diplom in Experimentalphysik Diplomarbeit: 'Bau und Test eines Driftkammerprototypen für LHC' Unter Leitung von Dr. G.Viertel
1992 - 1996	Wissenschaftliche Mitarbeit beim Experiment E865 am Brookhaven National Laboratory, NY
1997	Dissertation bei Prof. Dr. P. Truöl

Dozentenverzeichnis:

An der ETHZ besuchte ich Vorlesungen bei den Herren R. E. Bühler, R. Eichler, P. Feyerabend, J. Fröhlich, H. J. Gerber, H. Gränicher, W. Grüebler, G. Guekos, P. Günter, M. Gutknecht, M. Hegland, K. Hepp, A. Huber, W. Hunziker, R. Kind, F. Kneubühl, H. Knörrer, H. Läuchli, P. Läuchli, W. Lukosz, R. Müller, H. Nussbaumer, H. R. Ott, C. Schmid, K. R. Spillmann, J. Stromicki, M. Struwe, H. W. Tobler, J. Ulbricht

Nach dem Diplom besuchte ich an der Universität Zürich Vorlesungen und Seminare bei den Dozenten C. Amsler, D. Brinkmann, R. Engfer, W. Jaus, H. Keller, W. Kündig, P. F. Meier, J. Osterwalder, H. P. Pruys, G. Rasche, U. Straumann, P. Truöl